Eduardo Bonini Guedes

X-ray Spectroscopy and Electronic Structure of the $SrTi_{1-x}Ru_xO_3$ series and $Sr_2YRu_{1-x}Ir_xO_6$ (x = 0, 0.25)

Curitiba

2017

Eduardo Bonini Guedes

X-ray Spectroscopy and Electronic Structure of the $SrTi_{1-x}Ru_xO_3$ series and $Sr_2YRu_{1-x}Ir_xO_6$ (x = 0, 0.25)

Thesis presented in partial fullfilment of the requirement for the degree of PhD in Physics, at the Physics Department of Universidade Federal do Paraná.

Universidade Federal do Paraná

Setor de Ciências Exatas

Programa de Pós-Graduação em Física

Supervisor: Prof. Dr. Rodrigo J. O. Mossanek

Curitiba

2017

G924x Guedes, Eduardo Bonini
X-ray Spectroscopy and Electronic Structure of the SrTi1-xRuxO3 series and Sr2YRu1-xIrxO6 (x = 0, 0.25) / Eduardo Bonini Guedes. – Curitiba, 2017.
134 f. : il. color. ; 30 cm.

Tese - Universidade Federal do Paraná, Setor de Ciências Exatas, Programa de Pós-Graduação em Física, 2017.

Orientador: Rodrigo J. O. Mossanek.
Bibliografia: p. 114-121.

1. Física. 2. Estrutura eletrônica (Física). 3. Espectroscopia de raios-X. I. Universidade Federal do Paraná. II. Mossanek, Rodrigo J. O. III. Título.

CDD: 621.382

MINISTÉRIO DA EDUCAÇÃO
UNIVERSIDADE FEDERAL DO PARANÁ
PRÓ-REITORIA DE PESQUISA E PÓS-GRADUAÇÃO
Setor CIÊNCIAS EXATAS
Programa de Pós-Graduação FÍSICA

ATA Nº17

ATA DE SESSÃO PÚBLICA DE DEFESA DE DOUTORADO PARA A OBTENÇÃO DO GRAU DE DOUTOR EM FÍSICA

No dia vinte e dois de Fevereiro de dois mil e dezessete às 14:00 horas, na sala Pe, Departamento de Física - Bloco II - Centro Politécnico, foram instalados os trabalhos de arguição do doutorando **EDUARDO BONINI GUEDES** para a Defesa Pública de sua tese intitulada **X-Ray Spectroscopy and Electronic Structure of the SrTi1-xRuxO3 series and Sr2YRu1-xIrxO6 (x=0, 0.25)** . A Banca Examinadora, designada pelo Colegiado do Programa de Pós-Graduação em FÍSICA da Universidade Federal do Paraná, foi constituída pelos seguintes Membros: RODRIGO JOSÉ OCHEKOSKI MOSSANEK (UFPR), TULIO COSTA RIZUTI DA ROCHA (CNPEM), DANTE HOMERO MOSCA JÚNIOR (UFPR), EDUARDO GRANADO MONTEIRO DA SILVA (UNICAMP), KLEBER DAUM MACHADO (UFPR). Dando início à sessão, a presidência passou a palavra ao discente, para que o mesmo expusesse seu trabalho aos presentes. Em seguida, a presidência passou a palavra a cada um dos Examinadores, para suas respectivas arguições. O aluno respondeu a cada um dos arguidores. A presidência retomou a palavra para suas considerações finais e, depois, solicitou que os presentes e o doutorando deixassem a sala. A Banca Examinadora, então, reuniu-se sigilosamente e, após a discussão de suas avaliações, decidiu-se pela APROVAÇÃO do aluno. O doutorando foi convidado a ingressar novamente na sala, bem como os demais assistentes, após o que a presidência fez a leitura do Parecer da Banca Examinadora. Nada mais havendo a tratar a presidência deu por encerrada a sessão, da qual eu, RODRIGO JOSÉ OCHEKOSKI MOSSANEK, lavrei a presente ata, que vai assinada por mim e pelos membros da Comissão Examinadora.

Curitiba, 22 de Fevereiro de 2017.

RODRIGO JOSÉ OCHEKOSKI MOSSANEK
Presidente da Banca Examinadora (UFPR)

TULIO COSTA RIZUTI DA ROCHA
Avaliador Externo (CNPEM)

DANTE HOMERO MOSCA JÚNIOR
Avaliador Interno (UFPR)

EDUARDO GRANADO MONTEIRO DA SILVA
Avaliador Externo (UNICAMP)

KLEBER DAUM MACHADO
Avaliador Interno (UFPR)

MINISTÉRIO DA EDUCAÇÃO
UNIVERSIDADE FEDERAL DO PARANÁ
PRÓ-REITORIA DE PESQUISA E PÓS-GRADUAÇÃO
Setor CIÊNCIAS EXATAS
Programa de Pós-Graduação FÍSICA

TERMO DE APROVAÇÃO

Os membros da Banca Examinadora designada pelo Colegiado do Programa de Pós-Graduação em FÍSICA da Universidade Federal do Paraná foram convocados para realizar a arguição da tese de Doutorado de **EDUARDO BONINI GUEDES** intitulada: **X-Ray Spectroscopy and Electronic Structure of the SrTi1-xRuxO3 series and Sr2YRu1-xIrxO6 (x=0, 0.25)** , após terem inquirido o aluno e realizado a avaliação do trabalho, são de parecer pela sua APROVAÇÃO.

Curitiba, 22 de Fevereiro de 2017.

RODRIGO JOSÉ OCHEKOSKI MOSSANEK
Presidente da Banca Examinadora (UFPR)

TULIO COSTA RIZUTI DA ROCHA
Avaliador Externo (CNPEM)

DANTE HOMERO MOSCA JÚNIOR
Avaliador Interno (UFPR)

EDUARDO GRANADO MONTEIRO DA SILVA
Avaliador Externo (UNICAMP)

KLEBER DAUM MACHADO
Avaliador Interno (UFPR)

Dedicated to the memory of my mother.

Acknowledgements

It is often said that pursuing a PhD degree is a lonely process, which is a sentence I agree only to some extent. The thinking process required for work is done almost entirely solely, but this is not all. In fact, the hardest issues are personal, and it is in such situations that the support from family and friends is most needed. This part is devoted to acknowledge all the support I had during this part of my life.

Mother, although you have not been here physically during these last years, I am forever thankful for everything you did to me. You are my inspiration. I could not have done it without the unconditional love and help of my father and brother. Likewise, the daily routine became much easier with the love and care of my girlfriend. Thank you mom, dad, Gus and Fê. I hope you know how essential you are to me. I love you.

I am grateful to Prof. Rodrigo Mossanek for these 6 years of supervision. Thank you for all the lessons, trust, understanding and *beer*. I would also like to thank Prof. Miguel Abbate for having accepted me as part of the research group when I was an undergraduate student, and for all the wisdom shared.

I would like to acknowledge the members of the three committees during the PhD course, Drs.: José Varalda, Sergio d'A. Sanchez, Guilherme J. P. Abreu, Ismael L. Graff, Márcio H. F. Bettega, Dante H. Mosca, Eduardo Granado, Kleber D. Machado and Tulio C. R. Rocha. Your corrections and suggestions were much appreciated.

To all my professors during the undergraduate, Masters and PhD courses, thank you. In particular, I must thank Prof. José Arruda de Oliveira Freire, who was my teacher in several subjects. With his brilliant explanations, filled mathematical rigor and physical intuition, he made Physics even more exciting.

To all my friends who ensured me moments of fun, but also moments of Physics discussions and group work: Alessandra, Ali, Alexandre, Cleber, Diego, Guilherme, Henrique, Lucas and Santana: thank you. Also, special thanks to Ana Luiza who helped me get myself together in this difficult period.

I must also acknowledge CAPES for the scholarship, and all the collaborators who kindly provided me with their samples or supported me at the beamlines and, most importantly, shared their time and knowledge.

“Not ordinarily do men achieve this balance of opposites. The idealists are not usually realistic, and the realists are not usually idealistic. The militant are not generally known to be passive, nor the passive to be militant. Seldom are the humble self-assertive, or the self assertive humble. ...truth is found neither in the thesis nor the antithesis, but in an emergent synthesis that reconciles the two."

(Dr. Martin Luther King Jr.)

Abstract

The electronic structure of any material is the origin of its physical properties. The present work aims at the study of the electronic structure of the perovskite series $SrTi_{1-x}Ru_xO_3$ and the substituted double perovskite $Sr_2YRu_{1-x}Ir_xO_6$ with X-ray (resonant) photoemission and X-ray absorption spectroscopies, and at the interpretation of the experimental results with suitable theoretical models. The $SrTi_{1-x}Ru_xO_3$ series is particularly known for its intriguing electrical properties, which, among other features, presents an insulator-to-metal transition for x $\approx$ 0.7. The electronic structure of this series was characterized and, in particular, the spectra of $SrTi_{0.5}Ru_{0.5}O_3$ were simulated with a double cluster (DC) and by properly weighing the $SrTiO_3$ and $SrRuO_3$ single cluster calculations (SC). Although both approaches resulted in a good agreement with experiment, the analysis of the compositions of the peaks of the different spectra depend on the experimental technique and on the theoretical method used. The differences are addressed in terms of the position of Ti^{4+} and Ru^{4+} ions in the Zaneen-Sawatzky-Allen diagram diagram and of the screening mechanisms present in each spectrum. One of the other materials studied, Sr_2YRuO_6 present an intriguing magnetic behavior, which is thought to arise from the face-centered cubic arrangement of the Ru^{5+} ions. One possible approach to study the magnetic interactions in SYRO is to replace the Ru ion with Ir. The electronic structure of these materials are interpreted with Density Functional Theory calculations with and without the inclusion of the spin-orbit interaction in the Ru $4d$ and Ir $5d$ orbitals, with different magnetization axis. The calculated density of states satisfactorily reproduced the experimental spectra, including the changes in the spectra caused by Ir substitution. The spin orbit interaction causes a reduction of magnetic moments in Ir^{5+} ions, while is does not change the Ru^{4+} magnetic moments. This interaction does not lead to orbital ordering, but is responsible for suppressing the density of states at the Fermi level of $Sr_2YRu_{0.75}Ir_{0.25}O_6$. These results indicate that the spin-orbit interaction could actually play an important role in the stabilization of the magnetic ordering in the Sr_2YRuO_6 system. The combined results presented above stress the relevance of a combined experimental + theoretical approach in the study of the electronic structure of transition metal compounds, which enables to not only map, but to thoroughly interpret the occupied and unoccupied states.

Keywords: $SrTi_{1-x}Ru_xO_3$, $Sr_2YRu_{1-x}Ir_xO_6$, electronic structure, X-ray spectroscopy, cluster model, density of states.

Resumo

A estrutura eletrônica (EE) de qualquer material é a origem de suas proporiedades físicas. Em particular, óxidos de metais de transição (OMTs) apresentam uma intrigante estrutura eletrônica, caracterizada pela presença de elétrons d na banda de valência. Elétrons dessa natureza apresentam correlação eletrônica intermediária entre elétrons s, p e f, e fazem com que inúmeras propriedades físicas interessantes sejam observadas em OMTs. Grande parte desses materiais cristaliza em estruturas do tipo perovskita, caracterizada pela presença de octaedros de átomos de oxigênio com um átomo de metal de transição (MT) central (MTO_6). A EE desse tipo de material é dominada pela presença de estados de MT d no nível de Fermi, enquanto estados da banda $2p$ do oxigênio aparecem em mais altas energias de ligação. No entanto, dependendo de fatores como a diferença de eletronegatividade entre essas duas espécies e de sua hibridização, a presença de estados de O $2p$ no nível de Fermi pode ser favorecida. O presente trabalho estuda a estrutura eletrônica das séries de perovskitas $SrTi_{1-x}Ru_xO_3$ e das duplas perovskitas Sr_2YRuO_6 e $Sr_2YRu_{0.75}Ir_{0.25}O_6$ com Espectroscopia de Fotoemissão de raios-X (XPS), Espectroscopia de Fotoemissão Ressonante (RPES) e Espectroscopia de Absorção de raios-X (XAS). Tais técnicas experimentais são capazes de acessar diretamente a EE dos materiais, e o fazem de maneira complementar: XPS e RPES fornecem informações sobre estados ocupados do sistema, enquanto a XAS mapeia um subconjunto da densidade de estados desocupada. A interpretação dos resultados experimentais é feita com dois métodos teóricos também complementares: o modelo de Cluster e o cálculo de estrutura de bandas. O primeiro é baseado em um Hamiltoniano modelo local para o octaedro de MTO_6, com parâmetros ajustáveis que levam em conta a correlação eletrônica no orbital de MT d, a transferência de carga e a hibridização com a banda de O $2p$, e outras interações. O modelo de Cluster é adequado para o estudo de estados finais em espectros de raios-X, pois com ele são calculadas taxas de transição de um dado estado fundamental (GS) para estados finais (CS, RS e AS), criados para simular os espectros experimentais de XPS de nível interno, XPS de banda de valência e XAS na borda de O $1s$, respectivamente. O estudo detalhado desses estados finais fornece informações valiosas sobre a estrutura eletrônica dos materiais, especialmente aqueles onde a correlação eletrônica e outras interações locais têm um papel importante. Já o cálculo de bandas é um método *ab-initio* baseado na Teoria do Funcional da Densidade, que tem a densidade eletrônica do estado fundamental como variável fundamental. O método propõe uma separação da função de

onda de N elétrons em N funções de onda de uma-partícula, e deixa a cargo do potencial de troca e correlação V_{xc} os efeitos de muitos-corpos. Por outro lado, o método leva em conta exatamente os efeitos de banda, dados pela simetria de translação da rede cristalina. A série $SrTi_{1-x}Ru_xO_3$ é conhecida por apresentar propriedades elétricas intrigantes que, entre outras características, passa por uma transição de fase isolante-metal para $x \approx 0.7$. Nessa tese, a estrutura eletrônica dessa série é caracterizada e os espectros de $SrTiO_3$, $SrTi_{0.5}Ru_{0.5}O_3$ e $SrRuO_3$ são simulados. Em particular, o espectro de $SrTi_{0.5}Ru_{0.5}O_3$ é simulado com um modelo de Cluster Duplo (DC), no qual a interação entre os octaedros de TiO_6 e RuO_6 é incluída, e com a combinação linear apropriada de resultados de modelo de Cluster simples (SC), que não trata tal interação entre os octaedros. O modelo de Cluster é conveniente porque o interesse nesse caso é entender a influência da interação Ti – Ru nos estados finais que dão origem aos espectros de raios-X. Os espectros de $SrTiO_3$ e $SrRuO_3$ foram satisfatoriamente reproduzidos com um conjunto de parâmetros em acordo com resultados já publicados. As posições em energia e intensidade relativas dos espectros da amostra de $SrTi_{0.5}Ru_{0.5}O_3$ foram corretamente simulados com ambos os modelos. Porém, a análise das composições das principais estruturas do espectro revelou diferenças entre os dois modelos, dependendo da técnica experimental analisada. Enquanto os espectros calculados de XAS na borda de O 1s forneceram estados finais similares, os cálculos dos espectros de XPS de nível interno e banda de valência apresentaram uma notável redução na blindagem de O 2p no modelo DC.

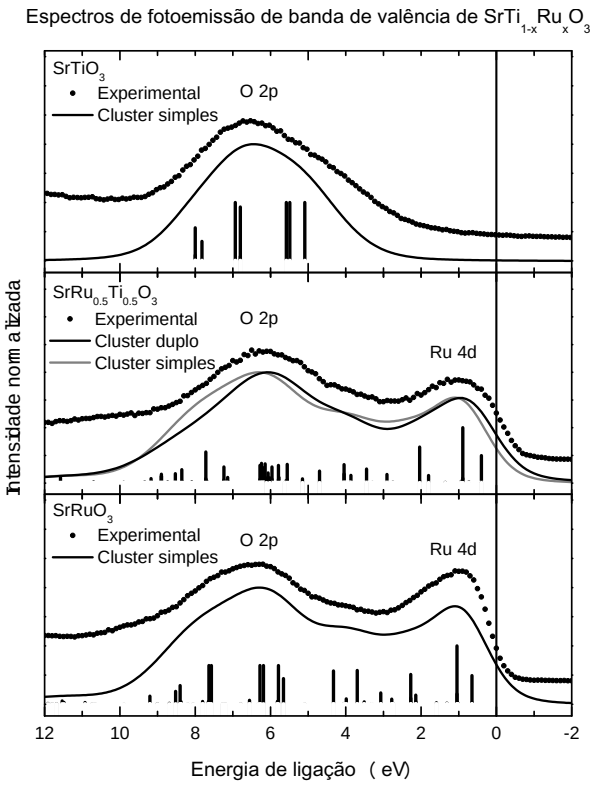

Enquanto os resultados de XAS forneceram estados finais similares, os espectros de XPS de nível interno e banda de valência apresentaram uma notável redução na blindagem de O 2p no modelo DC. As diferenças encontradas com o modelo DC são explicadas em termos das posições do íons de Ti^{4+} e Ru^{4+} no diagrama de Zaanen-Sawatzky-Allen, que favorece um estado fundamental altamente covalente e inibe outras flutuações da banda de O 2p. Ainda, os espectros de nível interno e banda de valência de $SrTi_{0.5}Ru_{0.5}O_3$ apresentam diferenças entre si nos mecanismos de blindagem calculados pelo modelo DC, que usualmente são similares em outros OMTs. Essas diferenças indicam que a criação do buraco é responsável por desacoplar as bandas de Ti 3d e Ru 4d no espectro de nível

interno, enquanto o efeito no espectro de banda de valência é o de misturar ainda mais o sistema, como evidenciado pela blindagem de O $2p$ na banda de Ti $4d$ sob a remoção de um elétron de Ru $4d$. Por utro lado, a dupla perovskita Sr_2YRuO_6, um dos outros materiais estudados, apresenta um comportamento magnético intrigante, originado do arranjo cúbico de face centrada que os íons de Ru^{5+} assumem nesse material, que dá origem ao fenômeno de magnetismo geometricamente frustrado. Uma possível abordagem pra estudar as interações magnéticas em Sr_2YRuO_6 é a substituição de Ru pelo íon menos magnético, e com um elétron extra na camada d, Ir^{5+}. As estruturas eletrônicas de Sr_2YRuO_6 e $Sr_2YRu_{0.75}Ir_{0.25}O_6$ são interpretadas com a Teoria do Funcional da Densidade, com e sem a inclusão do efeito da interação spin-órbita nos orbitais de Ru $4d$ de Ir $5d$. O uso desse método é justificado pelo interesse em estudar os momentos magnéticos, o ordenamento orbital e o efeito da interação spin-órbita no estado fundamental dessa série.

Os espectros experimentais foram corretamente descritos pelos cálculos, incluindo as mudanças causadas pela substituição parcial de Ru por Ir. Ainda, as contribuições do orbitais de Ru $4d$ para o espectro de fotoemissão de banda de valência foram indentificadas pela fotoemissão ressonante na borda de Ru L_3, e estão em bom acordo com a densidade de estados parcial de Ru $4d$. Ainda, os resultados de RPES para essa série, comparados com o resultado para $SrRuO_3$, indicam que o valor de U^{5+}_{Ru} é menor que o valor de U^{4+}_{Ru}, justificando o uso do cálculo de estrutura de bandas para estudar a EE desse material. A análise do estado fundamental calculado indica que a interação spin-órbita

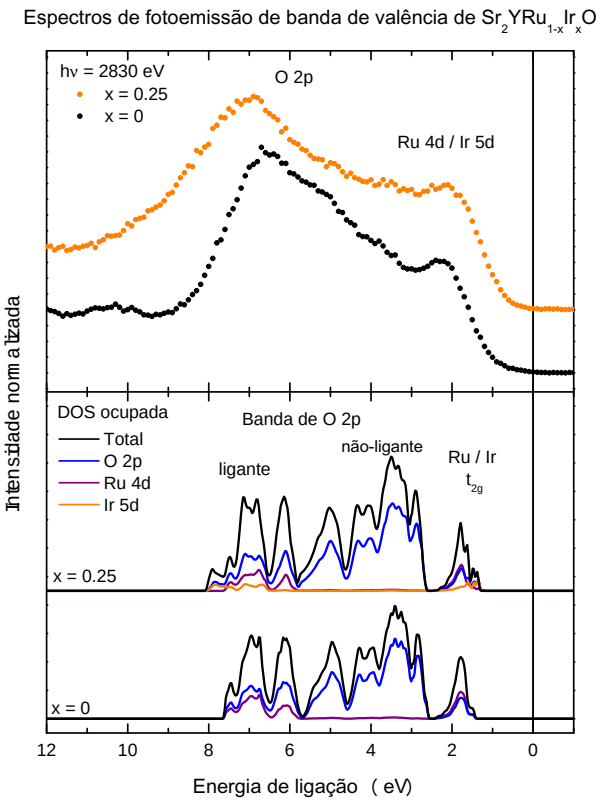

desvia o eixo de magnetização do plano cristalino ab, não altera os momentos magnéticos dos íons de Ru^{5+}, mas causa redução de 50% nos momentos magnéticos de Ir^{5+}. Ainda, essa interação é responsável por suprimir a densidade de estados no nível de Fermi, levando ao correto comportamento semicondutor da amostra, e não causa ordenamento orbital. Os resultados apresentados nesta tese destacam a relevância de uma abordagem experimental e teórica no estudo da estrutura eletrônica de óxidos de metais de transição. Do lado experimental, as fontes de luz síncrotron são aliadas importantes na produção de radiação adequada para a implementação de várias técnicas distintas, muitas vezes na mesma linha de luz. Vários métodos teóricos são encontrados na literatura, particularmente sepa-

rados em Hamiltonianos modelo (como o modelo de Cluster) e métodos *ab-initio* (como o cálculo de estrutura de bandas), cada qual com suas vantagense limitações. Apesar de todos eles poderem ser usados, a escolha conveniente do método é crucial para a correta interpretação dos epectros e da EE dos materiais. Essa escolha deve ser baseada não somente nos materiais em si, mas também nos espectros a serem interpretados e em outras informações de interesse.

Palavras-chave: $SrTi_{1-x}Ru_xO_3$, $Sr_2YRu_{1-x}Ir_xO_6$, estrutura eletrônica, espectroscopia de raios-X, modelo de cluster, densidade de estados.

List of Figures

List of Tables

Contents

1 Introduction

Contents

1.1 Electronic Structure

The electronic structure (ES) is the energy distribution of electronic states and populations of a certain atom, molecule or solid. The ES of any material determines a number of physical and chemical properties, such as its melting and boiling points, electrical and thermal conductivities and magnetic ordering. The study of the ES of macroscopic materials began around 1900, with the application of the kinetic theory of gases to study the electric conductivity of metals proposed by Paul Drude [1; 2], known as the Drude Model. Almost 30 years later (based on Drude's hypothesis) A. Sommerfeld [3] applied the Fermi-Dirac statistics to the Drude Model, developing a consistent mathematical description of metals. By the time the Drude-Sommerfeld theory was developed, F. Bloch had already studied the behavior of wave functions of non-interacting electrons in periodic lattices [4], which results in the formation of electronic bands. Ultimately, all these results culminated in a theory for the distinction between metals and insulators, widely known as the *electronic band theory*. At absolute zero, metals present a partially filled valence band, with a continuum of allowed energies for the electronic states; whereas insulators present a completely filled valence band well separated by an energy gap from the empty conduction band. At finite temperature, small gap insulators can be turned into semiconductors by thermal excitations from the valence to the conduction band, giving rise to electron-hole pairs [5–7]. This scenario is depicted in Figure 1.1.

In parallel, soon after the development of Schrödinger's equation in 1926, the electronic structure of multi-electronic atoms and ions was already an issue to researchers because of the complexity introduced by electron-electron interactions. In 1927, D. R. Hartree introduced a procedure for dealing with the many-particle wave function, which transforms the problem into a single-particle system in an effective field. This theory was

later set into a *variational principle* framework by J. C. Slater and adapted to respect Pauli's Exclusion Principle with the use of wave functions built from Slater determinants by Vladmir Fock, originating the celebrated Hartree-Fock method [8–12]. A few years later, Pierre Hohenberg, Walter Kohn and Lu Jeu Shan [13; 14] laid the basis of the celebrated Density Functional Theory (DFT), which is a widespread method based on the electronic density used to calculate the electronic structure and other properties of materials. The invention of computers in the 1950's certainly contributed to the popularization of these and other methods for electronic structure calculations, which were often interpreted in terms of the electronic band theory.

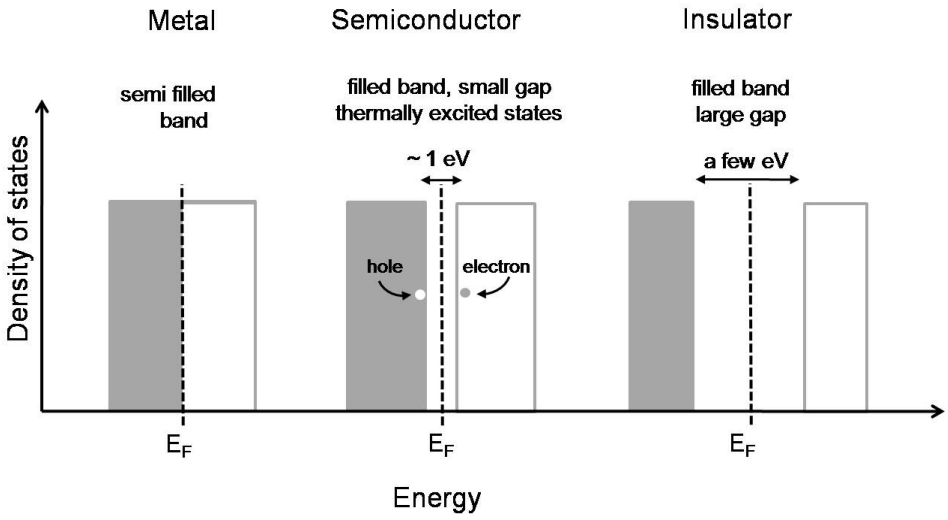

Figure 1.1 Representation of the electronic energy bands. At absolute zero, metals present a partially filled valence band and insulators present a completely filled valence band. At finite temperature, small gap insulators can be turned into semiconductors by thermal excitations.

Although the band picture was successful in many cases, the fact that a large number of transition metal oxides (TMOs) with a partially filled *d*-electron band were insulators was striking [15], the most famous example of this phenomenon being the nickel monoxide NiO. Concerning this deviation from the band picture prediction, N. F. Mott and R. Peierls noted that strong Coulomb repulsion could be the origin of the insulating behavior on partially filled *d* systems [16], giving rise to the field of *strongly correlated systems*. A few years later, Mott took an important step in understanding how electron-electron correlations could influence the intriguing state, which is called a *Mott insulator* [17–19]. In a Mott-insulator, depicted in Fig 1.2, two electrons occupying the same band would be subjected to a large Coulomb repulsion (U), which Mott argued would split the band in two: a low energy band (known as the *Lower Hubbard Band*), formed by singly occupied states, and a high energy band (known as *Upper Hubbard Band*), formed by doubly occupied states. Hence, a half filled system, with one electron per band, would be

insulating. More accurately, the system would be an insulator if $U/W > 1$, where W is the band width.

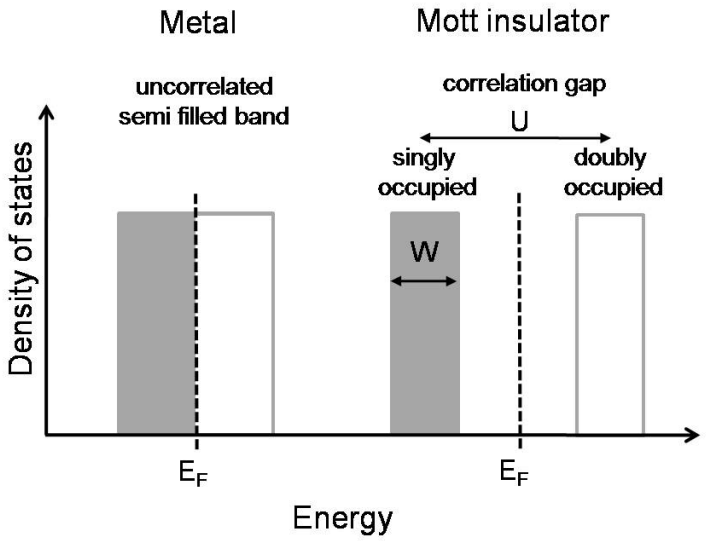

Figure 1.2 Schematic view of the electronic structure of a Mott-insulator. Singly occupied states are separated from doubly occupied states by U, which can open a band gap.

Experimentally, the electronic structure of materials can be directly accessed with spectroscopic techniques such as the X-ray Photoemission Spectroscopy (XPS), different types of X-ray Absorption Spectroscopies (XAS), X-ray Emission Spectroscopy (XES), and others [20]. In particular, the XPS and XAS techniques will be described in Section 2. The spectroscopic methods were greatly benefited from the surge of interest in synchrotron radiation storage rings in the 1970's. These sources can achieve higher energies and intensities than conventional X-ray tubes, and also provide the possibility to continuously change photon energy, which is crucial for some techniques. As a milestone, it is worth noting that in 1974, the INS-SOR (Institute for Nuclear Studies-Synchrotron Orbital Radiation) in Tokyo, commissioned a 300 MeV storage ring, considered the first machine designed from the beginning specifically for the production of synchrotron radiation [21]. A direct consequence of this development can be seen in a simple Google Scholar search of the expression "photoemission spectroscopy" which reveals a 10 times increase in the number of results between 1970 and 1980 compared to the previous decade. Then, the increasing availability of experimental data allowed a combined experimental–theoretical approach, which has proven to be extremely powerful in the study of strongly correlated systems.

1.2 Transition Metal Oxides

The important role played by electronic correlations in the electronic structure of transition metal oxides stem from a peculiarity of the d orbitals, which form the valence band of the majority of the TMOs. The bands originated from the d orbitals lie in the frontier between delocalized (like the ones originated from s and p orbitals) and localized (originated from f orbitals).

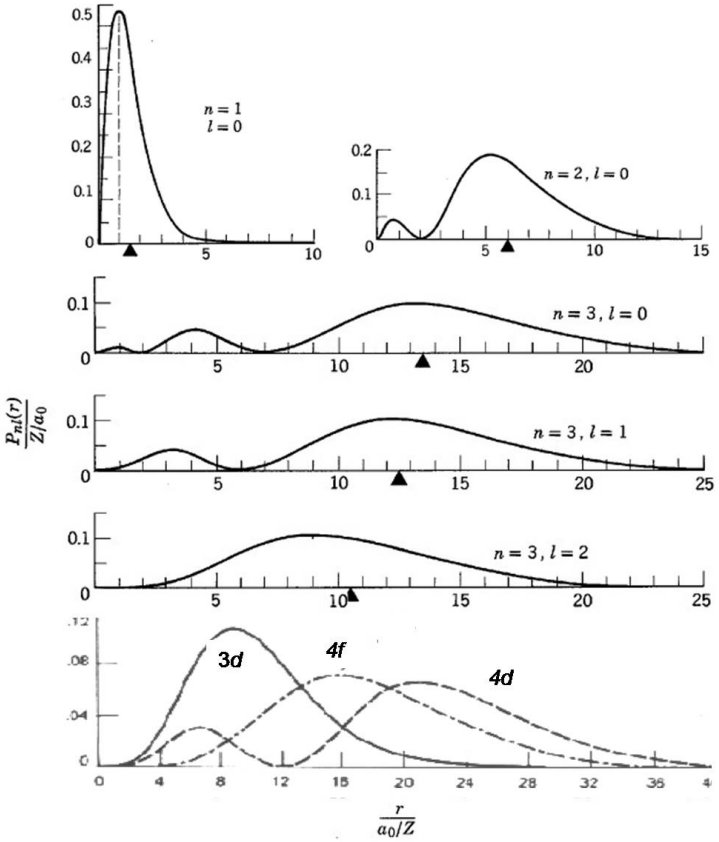

Figure 1.3 Normalized radial probability distributions of hydrogen-like wave functions with principal quantum numbers $n = 1, 2$, $\ell = 0$; $n = 3$, $\ell = 0,1,2$; and $n = 4$, $\ell = 2,3$, as function of the normalized distance from the nucleus, in which expectation values $\langle r \rangle$ are marked by triangles. Adapted from [22].

Figure 1.3, adapted from [22], presents the normalized radial probability distributions of hydrogen-like wave functions with principal quantum numbers $n = 1, 2$, $\ell = 0$; $n = 3$, $\ell = 0,1,2$; and $n = 4$, $\ell = 2,3$, *i.e.* $1s$, $2s$, $3s$, $3p$, $3d$ $4d$ and $4f$ orbitals, as function of the normalized distance from the nucleus. The expectation values $\langle r \rangle$ are marked by triangles. The d wave function has the smallest mean radius, when confronted to s or p electrons, relative to the typical lattice parameter of a crystal (as seen by the triangles in the $n = 3$, $\ell = 0,1,2$ graphics). Hence, d-electron systems have in general smaller overlap,

smaller bandwidths and greater electronic correlation than s- or p- electron systems. On the other hand, d orbitals are still less correlated than f orbitals, which present even smaller mean radius, as illustrated in the bottom graph of Fig. 1.3, and a larger mean occupancy number. Furthermore, the principal quantum number n can also have an effect on the degree of correlation, since the wave function radius depends on n, as illustrated for s electrons by the $n = 1, 2, 3$, $\ell = 0$ graphics and in the bottom of the Figure for $3d$, $4d$ and $4f$ orbitals.

The borderline nature of the d bands is decisive to the appearance of the myriad of physical properties shown by TMOs, for instance ferrimagnetism and tunneling magnetoresistance in Sr_2FeMoO_6 [23], itinerant ferromagnetism in $SrRuO_3$ [24], high-T_C superconductivity in $La_{2-x}Ca_xCuO_4$ [25] and colossal magnetoresistance in $La_{1-x}Ca_xMnO_3$ [26]. These properties are accompanied by several electrical and magnetic phase transitions that can be triggered by temperature (VO_2) [27], chemical composition ($Y_{1-x}Ca_xVO_3$) [28] or pressure (V_2O_3) [29]. Also, transition metal oxides have been used as catalysts [30], solid state fuel cells [31] and in photovoltaic devices [32].

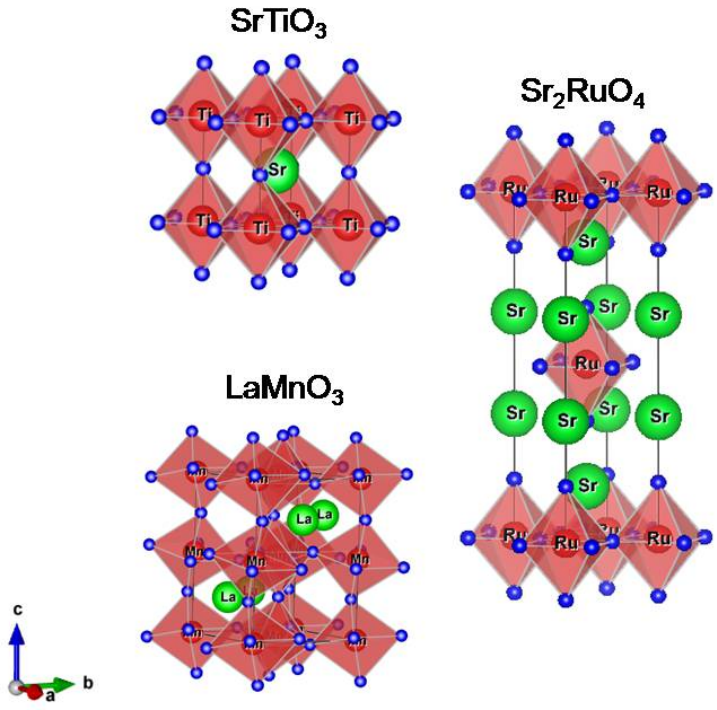

Figure 1.4 Crystal structures representations of the cubic perovskite $SrTiO_3$, the distorted $LaMnO_3$ and the layered Sr_2RuO_4. Drawings made with the VESTA software [33].

A great number of these materials crystallizes in perovskite or perovskite-like structure, characterized by the BO_6 octahedra, with B being the transition metal. The cubic perovskite structure, with chemical formula ABO_3 where A is usually a cation from the 1 or 2 families, belongs to the Pm-3m space group (#221) and presents regular BO_6 octa-

hedra. The structure can be visualized in Fig 1.4. Some perovskites may deviate from the cubic structure, presenting non-regular octahedra and distorted B–O–B connectivity like $LaMnO_3$, or crystallize in more complex structures such as the layered ruthenate Sr_2RuO_4, which are also depicted in Fig. 1.4.

Figure 1.5 shows a scheme of the electronic structure of TMOs, in which TM states are depicted in red, O $2p$ states in blue, and occupied (unoccupied) bands as solid (open) rectangles. In perovskite and perovskite-like materials, the ES close to the Fermi level is strongly influenced by the outermost d electrons of the transition metal, placed inside the TMO_6 octahedron. The O $2p$ states would appear at higher binding energies, although, in some materials, a small difference between the center of the TM d and O $2p$ bands and a strong TM d–O $2p$ hybridization may favor the presence of O $2p$ states at E_F. Such cases require the explicit introduction of O $2p$ states [34].

In general, the necessary ingredients for a correct description of the electronic structure of TMOs vary, and depends on the material itself. When interested in properties such as the band gap or magnetic moments, ground state methods which incorporate the translational symmetry of the system, such as the DFT are the convenient ones. On the other hand, the many-body interactions are in general important to interpret spectroscopic data, described by local Hamiltonian models. Similarly, it is advantageous to combine complementary experimental techniques, *i.e*, map both occupied and unoccupied parts of the ES of the compound such as the XPS and XAS; or probe different species in the sample, for instance with Resonant XPS. The choice of the experimental techniques also impacts on the theoretical methods used to analyze the data, since many-body effects have distinct relative importance, when compared to band effects, in each type of experiment.

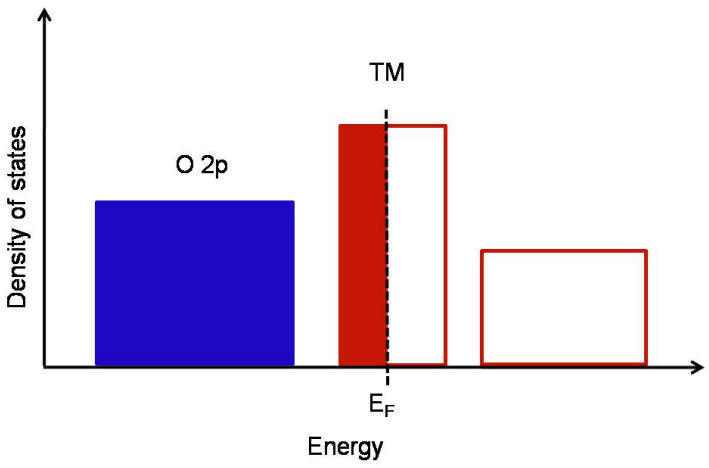

Figure 1.5 Representation of the electronic structure of TMOs. The ES close to the Fermi level is strongly influenced by TM d states, while O $2p$ states would appear higher binding energies

.

1.3 Main Goals

The present work aims at the study of the electronic structure of the perovskite series $SrTi_{1-x}Ru_xO_3$ and the substituted double perovskite $Sr_2YRu_{1-x}Ir_xO_6$ with several spectroscopic techniques. The interpretation of the results is done with suitable theoretical models. The experimental techniques are the X-ray photoemission spectroscopy (XPS), the Resonant X-ray Photoemission Spectroscopy (RPES) and the X-ray absorption spectroscopy (XAS). All the measurements were performed at the Laboratório Nacional de Luz Síncrotron - Campinas - Brazil. The experimental data were analyzed with a (Double) Cluster Model, developed during this work, and with the Density Functional Theory, implemented in the WIEN2k package. Both series studied in this work, $SrTi_{1-x}Ru_xO_3$ and $Sr_2YRu_{1-x}Ir_xO_6$, can be obtained from the same parent compound, $SrRuO_3$, which has been extensively studied, including a work by our group [35].

The $SrTi_{1-x}Ru_xO_3$ series presents very diverse electrical transport properties depending on x. On one end ($x \approx 0$), the series presents insulating character, which evolves to a correlated metal state ($x \approx 1$) going through different behaviors depending on the Ru concentration. An elusive insulator-to-metal transition is seen at $x \approx 0.70$ [36], whose mechanism is still under debate. Also, B-site order was shown to play a role in Sr_2TiRuO_6 thin films, since disordered samples (in which Ti and Ru are randomly distributed in the B sites) present lower electrical resistivity and higher number of states at the Fermi level than ordered samples [37], indicating that the TiO_6 – RuO_6 interaction may play a relevant role in the $SrTi_{1-x}Ru_xO_3$ series. The main goals regarding this series, discussed in details in Chapter 4, are the description of its electronic structure with X-ray spectroscopies and, in particular, the interpretation of the experimental results of the $SrTi_{0.5}Ru_{0.5}O_3$ sample with the Cluster and Double Cluster models. These models were chosen (i) because model Hamiltonians, such as the Cluster model, are suitable tools to analyze final state effects in X-ray spectra of correlated materials; (ii) in order to give continuity to the Cluster model study of $SrRuO_3$. The final goal of this part of the thesis is a comparison between the results obtained with Cluster and Double cluster models, aiming at understanding the role of the TiO_6 – RuO_6 interaction in the features present in the X-ray spectra.

In turn, $Sr_2YRu_{1-x}Ir_xO_6$ series presents an intricate antiferromagnetic ground state for $x = 0$. Although magnetic interactions are thought to arise only from Ru^{5+} ions, SYRO presents two phase transitions, one at $T_{N2} \approx 24$ K and the other at $T_{N1} \approx 32$ K [38; 39]. The existence of two phase transitions and other anomalous magnetic properties presented by this material [40] are believed to stem from the face-centered-cubic (fcc) network formed by the Ru^{5+} ions, which leads to *geometric frustrated magnetism* [41].

This system can be further studied with the substitution of Ru by Ir, which destabilizes the ordering temperature and introduces one extra electron/Ir in the unit cell. There is one important electronic structure study of Sr_2YRuO_6 and other ruthenium oxides [Mazin and Singh (1997)], which although very thorough and acclaimed, was performed with less computational resources (software and hardware) than are available today, including the possibility of treating the spin-orbit interaction in the valence orbitals. The literature specially scarce regarding experimental results and works on Ir-substituted samples. Hence, the main goals regarding the $Sr_2YRu_{1-x}Ir_xO_6$ series, discussed in details in Chapter 5, are the description of the electronic structure of this system with X-ray spectroscopic methods and band structure calculations, aiming at the study of the effects of Ir substitution and the role of the spin-orbit interaction on the electronic structure and ground state properties of both pristine and substituted samples. The band structure calculations within the DFT framework are suitable in this case because (i) it is a ground state method; (ii) the Ir substitution and spin-orbit interactions are easily included; (iii) there is experimental evidence that the electronic correlation of Ru^{3+} ions in the $Sr_2YRu_{1-x}Ir_xO_6$ series is smaller than in Ru^{4+} ions in $SrRuO_3$, which justifies the comparison of X-ray spectra with the calculated density of states. Analysis of the calculated magnetic moments and orbital occupancies may be useful to understand the intriguing magnetic properties of Sr_2YRuO_6.

This thesis is divided the following way: Chapter 2 briefly reviews the interaction of X-rays with matter, and then describes the spectroscopic techniques used to study the electronic structure of the $SrTi_{1-x}Ru_xO_3$ and $Sr_2YRu_{1-x}Ir_xO_6$ series. Chapter 3 discusses the (Double) Cluster model and the band structure calculations used to interpret the experimental results, along with the justification to their use for each series. The results of the XPS and XAS measurements for $SrTi_{1-x}Ru_xO_3$ and $Sr_2YRu_{1-x}Ir_xO_6$, and their interpretation with the corresponding theoretical methods, are discussed in Chapters 4 and 5. Finally, Chapter 6 presents the concluding remarks.

2 Experimental Techniques

In this Chapter the experimental techniques used in this thesis are introduced. After a general view on spectroscopy and the interactions of X-ray with matter, the X-ray Photoemission Spectroscopy (XPS), X-ray Absorption Spectroscopy (XAS) and Resonant Photoemission Spectroscopy (RPES) will be described. The details of the measurements are presented at the end o this Chapter.

Contents

2.1 Interaction of X-rays with Matter

As already mentioned, the ES of any material is at the origin its physical and chemical properties. Conventional experimental techniques *e.g.*, specific heat, electrical conductivity and magnetic susceptibility measurements, are able to provide information on some aspects of the electronic structure of materials, such as the effective mass, the charge carrier mobility and the magnetic moment. In some cases, however, this information is not enough to completely understand the observed physical properties. In such cases, X-ray spectroscopic techniques enter as important tools to access properties that sometimes cannot be obtained with other techniques.

X-rays are broadly defined as electromagnetic radiation with energy $E = h\nu = \hbar\omega$ ($\omega = 2\pi\nu$) between 100 eV and 100 keV, which corresponds to frequencies ν between the order of 10^{16} Hz and 10^{19} Hz, or wavelengths $\lambda = c\nu$ between 10 nm and 10 pm, as depicted in Fig. 2.1. X-rays are subdivided into two categories: *soft* X-rays, from 100 eV to 3 keV, which can penetrate air up to a few centimeters, and *hard* X-rays, from 3 keV to 100 keV, which penetrate up to a few meters. Recently, photons with energies in the intermediate 2 keV–5 keV range have been referred to as *tender* X-rays [20].

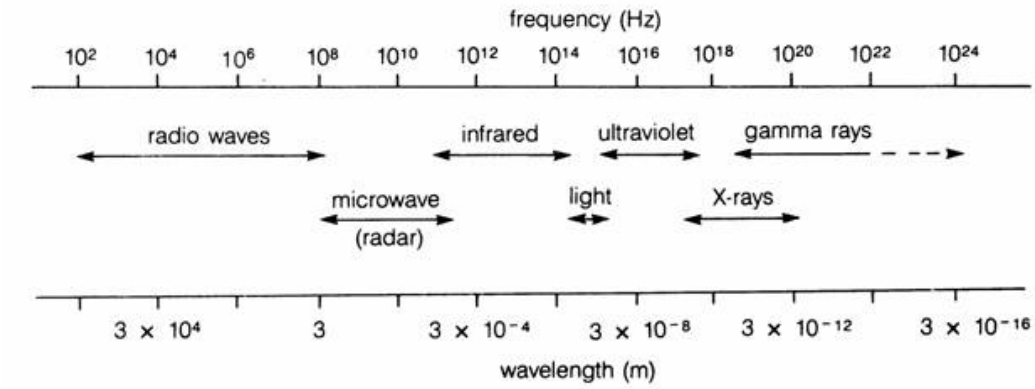

Figure 2.1 The electromagnetic spectrum from lowest energy/longest wavelength (left) to highest energy/shortest wavelength (right). X-rays are located between frequencies ν of 10^{16} Hz to 10^{19} Hz, or wavelengths $\lambda = c/\nu$ between 10 nm and 10 pm, corresponding to energies E = $h\nu$ = $\hbar\omega$ between 100 eV and 100 keV.

When an X-ray photon hits a sample, besides simply not interacting and being transmitted, it can be either absorbed or scattered. In the first case, an electron absorbs the photon and can either be excited to the conduction band, corresponding to X-ray Absorption techniques, or ejected as a photoelectron, originating the X-ray Photoemission Spectroscopy. These two *first-order* techniques will be described in the following sections. The scattering phenomenon is a second-order process which give rise to techniques such as the X-ray Emission spectroscopy [43] and X-ray Raman Scattering [20] techniques, which will not be discussed in this thesis.

Classically, an electromagnetic field can be described by $\boldsymbol{E}$ and $\boldsymbol{B}$ fields that obey the following Maxwell's equations, in vacuum and far from the field sources (in Gaussian units):

$$\begin{aligned} \nabla \cdot \boldsymbol{E} &= 0 & \nabla \cdot \boldsymbol{B} &= 0 \\ \nabla \times \boldsymbol{E} &= -\frac{1}{c}\frac{\partial}{\partial t}\boldsymbol{B} & \nabla \times \boldsymbol{B} &= \frac{1}{c}\frac{\partial}{\partial t}\boldsymbol{E} \end{aligned} \tag{2.1}$$

One set of solutions is

$$\boldsymbol{E}(\boldsymbol{r}, t) = \boldsymbol{E_0}\, sin(\boldsymbol{k}\cdot\boldsymbol{r} - \omega t) \tag{2.2}$$

$$\boldsymbol{B}(\boldsymbol{r}, t) = \boldsymbol{B_0}\, sin(\boldsymbol{k}\cdot\boldsymbol{r} - \omega t) \tag{2.3}$$

With $\boldsymbol{E}_0$, $\boldsymbol{B}_0$ being constant, $\boldsymbol{k} = (\omega/c)\hat{\boldsymbol{z}}$, with $\boldsymbol{k}\times\boldsymbol{E_0} = (\omega/c)\boldsymbol{B_0}$ and $\boldsymbol{k}\times\boldsymbol{B_0} = -(\omega/c)\boldsymbol{E_0}$, which represents a linearly polarized wave traveling in the z-direction.

Usually, for electromagnetic waves, the potentials ϕ and $\boldsymbol{A}$, used to generate the $\boldsymbol{E}$ and $\boldsymbol{B}$ fields through $\boldsymbol{E} = \nabla\phi - (1/c)\partial\boldsymbol{A}/\partial t$ and $\boldsymbol{B} = \nabla\times\boldsymbol{A}$, are chosen in the Coulomb

gauge $\nabla \cdot \boldsymbol{A}(\boldsymbol{r}, t) = 0$. Then,

$$\boldsymbol{A} = \boldsymbol{A_0}\, cos(\boldsymbol{k} \cdot \boldsymbol{r} - \omega t) \tag{2.4}$$

$$\phi(\boldsymbol{r}, t) = 0 \tag{2.5}$$

are the potentials which generate the $\boldsymbol{E}(\boldsymbol{r}, t)$ and $\boldsymbol{B}(\boldsymbol{r}, t)$ fields.

In the Quantum Mechanics formalism, a spinless electron subjected to this electromagnetic wave is governed by the following spinless Hamiltonian:

$$\hat{H}_{electron-field}(\hat{\boldsymbol{R}}, \hat{\boldsymbol{P}}, t) = \frac{1}{2m}\left[\hat{\boldsymbol{P}} + \frac{e}{c}\boldsymbol{A}(\hat{\boldsymbol{R}}, t)\right]^2 \tag{2.6}$$

In which m and e are the electronic mass and charge, respectively. In most cases, the $\boldsymbol{A}^2$ term can be neglected in comparison $\hat{\boldsymbol{P}} \cdot \boldsymbol{A}(\hat{\boldsymbol{R}}, t)$. For instance, the SXS beamline of the Brazilian Synchrotron Light Laboratory (LNLS) delivers a photon flux of density of 4×10^{14} ph/s/cm^2 with $\hbar\omega = 3000$ eV [44], which makes $\boldsymbol{A}^2$ approximately 10^{-5} smaller than $\hat{\boldsymbol{P}} \cdot \boldsymbol{A}(\hat{\boldsymbol{R}}, t)$.

Additionally, the Coulomb gauge is also called the Transverse gauge, because it yields $\boldsymbol{A}(\hat{\boldsymbol{R}}, t)$ and $\boldsymbol{k}$ vectors that makes $\hat{\boldsymbol{P}} \cdot \boldsymbol{A}(\hat{\boldsymbol{R}}, t)$ commute with $\boldsymbol{k} \cdot \hat{\boldsymbol{R}}$. Expanding the cosine of $\boldsymbol{A}(\hat{\boldsymbol{R}}, t)$ in complex exponentials, we arrive at the interaction Hamiltonian:

$$\hat{H}_{int}(\hat{\boldsymbol{R}}, \hat{\boldsymbol{P}}, t) = \frac{e}{mc}\left[\underbrace{(\boldsymbol{A_0} \cdot \hat{\boldsymbol{P}})e^{i\boldsymbol{k}\cdot\hat{\boldsymbol{R}}}e^{-i\omega t}}_{\text{absorption}} + \underbrace{(\boldsymbol{A_0} \cdot \hat{\boldsymbol{P}})e^{-i\boldsymbol{k}\cdot\hat{\boldsymbol{R}}}e^{+i\omega t}}_{\text{emission}}\right], \tag{2.7}$$

where the labeled terms represent the absorption and the emission of a photon. Since the techniques used in this thesis are based on the absorption of the incoming X-ray photon, the emission term will be ignored.

It is possible to rewrite H_{int} using the Taylor expansion $\mathrm{e}^{i\boldsymbol{k}\cdot\hat{\boldsymbol{r}}} \approxeq 1 + \boldsymbol{k} \cdot \hat{\boldsymbol{r}} + ...$ If X-ray energies are below ~ 10 keV, $\boldsymbol{k} \cdot \hat{\boldsymbol{R}}$ is smaller than 10^{-2}, and the expansion can be truncated in the zero-th order term, which is the so-called the *dipole approximation*. Finally, for first-order processes such as XPS and XAS, the transition rate of a system going from an initial state $|\psi_i\rangle$ to a final state $|\psi_f\rangle$ upon incidence of an X-ray photon of energy $\hbar\omega$, in the dipole approximation, is given by the Fermi's Golden Rule [20]:

$$\Gamma_{i\to f}(\omega) = \frac{2\pi}{\hbar}\left(\frac{e\hbar}{mc}\right)^2 \left|\langle\psi_f|\,(\boldsymbol{A_0} \cdot \hat{\boldsymbol{P}})\,|\psi_i\rangle\right|^2 \delta(E_f - E_i - \hbar\omega) \tag{2.8}$$

2.2 X-ray Photoemission Spectroscopy

The X-ray Photoemission Spectroscopy (XPS) is a technique based on the photoelectric effect, described by A. Einstein in 1905 [45]. In an XPS experiment, a sample

holder is kept in ultra-high vacuum, while X-ray photons hit the sample and eject electrons, which have their kinetic energy measured in an electron analyzer (see Figure 2.2). Part of the incoming energy hν is spent to take the electron out off its energy level (core

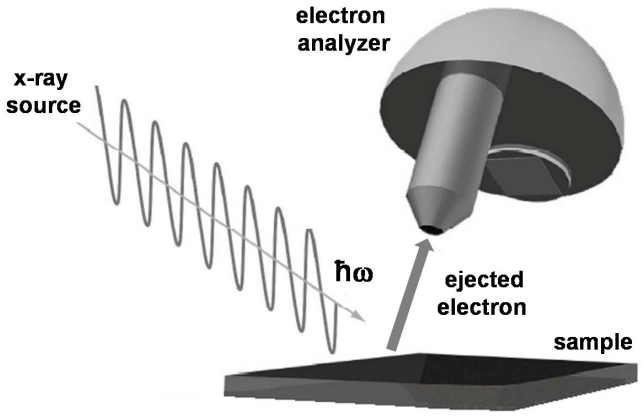

Figure 2.2 General setup of an XPS measurement, with the X-ray source, the sample and the electron analyzer.

or valence state), while the other part is spent to overcome the sample's work function ϕ_s and reach the vacuum level. The remaining of the incoming energy is left in the form of kinetic energy of the ejected photoelectron, as depicted in Fig. 2.3. Then, if E_K is measured, it is possible to find the binding energy E_B of the photoelectron, leading to the following energy conservation equation:

$$E_B = \hbar\omega - E_K - \phi_s. \tag{2.9}$$

In order to measure E_K, it is necessary to send the photoelectrons through the kinetic energy analyzer into the detector, which has a work function ϕ_a. Then, if the sample and the analyzer are put in electrical contact, their Fermi levels align and a contact potential of $\phi_s - \phi_a$ appears between them. Therefore the right-hand side of equation 2.12 reduces to $\hbar\omega - E_K - \phi_a$. Now the work function of the sample does not affect E_K anymore, but they are influenced by the work function of the analyzer. It is then possible to calibrate the kinetic energy scale with the aid of a reference sample, *e.g.* a clean gold foil, and define that the fastest electrons of the valence band spectrum (*i.e.* the Fermi edge feature) have $E_K = \hbar\omega$, and shift the entire spectrum accordingly; or to use a known core peak such as the Au $4f$ core level and correct for any shift in binding energy related to the well-known values. Now the kinetic energy scale is referenced to the Fermi level of the sample + analyzer system, and the binding energy is simply $E_B = \hbar\omega - E_K$, which sets the Fermi edge automatically at $E_B = 0$ eV [46].

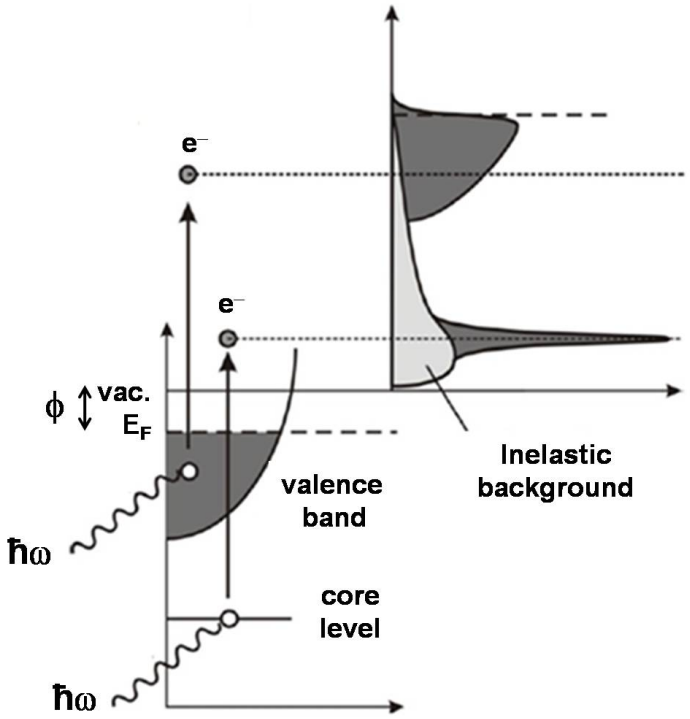

Figure 2.3 Schematic view of the XPS experiment. The incident photon with energy $\hbar\omega$ is absorbed by a core or valence electron and ejected as a photoelectron.

This picture is known as the *one-step model*. In a real sample, however, the photoelectron may suffer from inelastic effects during the transport inside the sample, originating the background seen in Fig. 2.3. The *direct* photoemission process can be described considering a division into three subsystems [20; 47]:

1. An electron $|\varphi_{\mathbf{k}}\rangle$ with energy ϵ_k, which absorbs an incoming photon of energy $\hbar\omega$;
2. An outgoing photoelectron, detected as a plane wave $|\mathbf{k}\rangle$ with energy $E_k = \frac{\hbar^2 k^2}{2m}$;
3. The valence electron system (VES), represented by $|d_0^n\rangle$ and $|d^{n-1}\rangle$, which contains the partially filled conduction band in metals and the filled and unfilled valence and conduction bands in insulators with n and $n-1$ electrons, respectively.

Subsystems 1 and 2 are treated as independent single-particles, but the core hole left behind is represented by a general interaction $\hat{V}$ that acts on 3. The VES is treated as a many-body system, and its initial and final states satisfy the following relations for $\hat{H}_0$ and $\hat{H} = \hat{H}_0 + \hat{V}$:

$$\hat{H}_0 \left|d_0^n\right\rangle = E_0^n \left|d_0^n\right\rangle \tag{2.10}$$

$$\hat{H} \left|d^{n-1}\right\rangle = E^{n-1} \left|d^{n-1}\right\rangle \tag{2.11}$$

The direct photoemission process can be written as

$$|\varphi_{\mathbf{k}}\rangle\,|d_0^n\rangle + \hbar\omega \rightarrow |\mathbf{k}\rangle\,|d^{n-1}\rangle\,, \tag{2.12}$$

where it can be assumed that the products $|\varphi_{\mathbf{k}}\rangle\,|d_0^n\rangle$ and $|\mathbf{k}\rangle\,|d^{n-1}\rangle$ are properly antisymmetrized. Also, by separating the $|\varphi_{\mathbf{k}}\rangle$ electron from the remaining system, it is implicitly assumed that the primary excitation ($|\varphi_{\mathbf{k}}\rangle \rightarrow |\mathbf{k}\rangle$) is fast compared to the relaxation time of the remaining electrons, which is known as the *Sudden Approximation*. This approximation was vastly studied [48; 49], and is known to hold for photoelectron kinetic energies higher than ~ 10 eV, which is the case in the XPS measurements presented in this thesis. Then, replacing the representations of subsystems 1, 2 and 3 into the Fermi's Golden Rule (equation 2.11), leads to the photoemission signal $I(\omega, E_K)$ for an incident photon of energy $\hbar\omega$ and for an ejected photoelectron with energy E_K [20; 47]:

$$I\left(\omega, E_k\right) \propto \left|\langle \boldsymbol{k}|\left(\boldsymbol{A_0}\cdot\hat{\boldsymbol{P}}\right)|\varphi_{\boldsymbol{k}}\rangle\,\langle d^{n-1}|d_0^n\rangle\right|^2 \delta\left(\epsilon_k + \phi + E_{n-1} - E_n - \hbar\omega\right)\delta\left(E_K - \epsilon_k\right), \tag{2.13}$$

where $f\left(E_K\right) \equiv \langle \boldsymbol{k}|\left(\boldsymbol{A_0}\cdot\hat{\boldsymbol{P}}\right)|\varphi_{\boldsymbol{k}}\rangle\,\delta\left(E_k - \epsilon_k\right)$ is proportional to the *photoionzation cross section* [50], *i.e.*, the probability of transforming $|\varphi_{\boldsymbol{k}}\rangle$ into a photoelectron $|\boldsymbol{k}\rangle$. In a regular XPS measurement, far from an *absorption edge* (defined in the next Section), $f\left(E_K\right)$ is practically constant in the energy range of the measured spectra, so it can be regarded as a constant.

The term $\langle d^{n-1}|d_0^n\rangle$ is non-vanishing because $|d_0^n\rangle$ and $|d^{n-1}\rangle$ are eigenstates of distinct Hamiltonians, as defined in equations 2.10 and 2.11. Actually, $|d_0^n\rangle$ and $|d^{n-1}\rangle$ are eigenstates of the number operator $\hat{n}_d$ with eigenvalues n and $n-1$ in the Fock space, respectively. Therefore there is a set of final states $|d_{0k}^{n-1}\rangle$ which is connected to the $|d_0^n\rangle$ state via proper annihilation operators $\hat{d}_\alpha$, where α labels the ejected electron, for instance a TM $4d$ or an O $2p$ electron. This fact, along with equation 2.2 used to change the variable from $\hbar\omega$ to E_B, leads to the final expression of $I_\alpha(E_B)$:

$$I_\alpha\left(E_B\right) \propto \sum_k \left|\langle d_{0k}^{n-1}|\,\hat{d}_\alpha\,|d_0^n\rangle\right|^2 \delta\left(E_{n-1} - E_n - E_B\right), \tag{2.14}$$

Considering the d^{n-1} states to be the same after the creation of the hole is known as the *frozen orbital approximation*, and through the Koopmans' theorem, which states that the energy required to remove an electron from this orbital is the negative of the energy of the orbital $\phi_{\boldsymbol{k}}$, the resulting XPS spectra would present one peak at the same binding energy in the XPS spectrum, being equivalent to the measurement of the density of states (DOS). In TMO's, because of electronic correlations, this approximation is poor, and the remaining electrons tend to rearrange after the creation of the hole in different

d_k^{n-1} states. Indeed, equation 2.14 is proportional to the spectral function $A(E_B)$, which is reduced to the density of states $\rho(E_B) = \sum_k \delta(\varepsilon_k - E_B)$ in the limit of non-interacting particles ($\hat{V} \to 0$) [20; 47], and is discussed in more details in Appendix B.2.

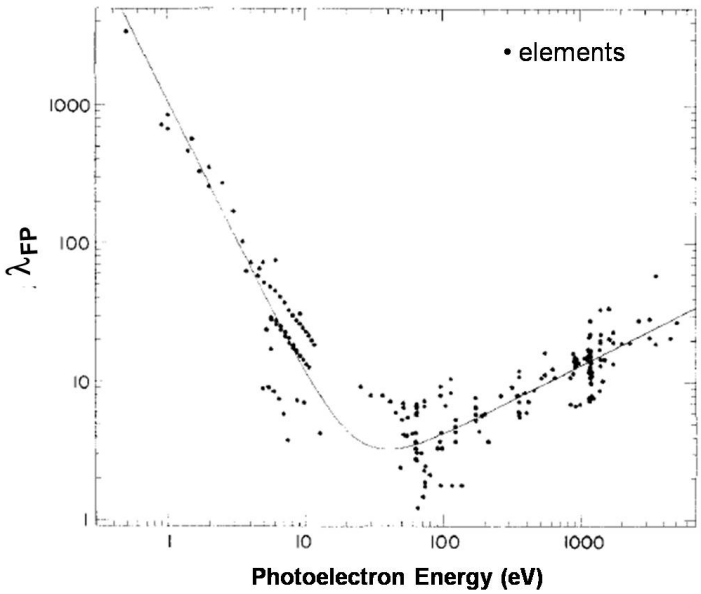

Figure 2.4 Inelastic mean free path λ_{FP} of electrons in an XPS experiment as function of the ejected photoelectron kinetic energy. Adapted from [51].

The previous description does not account for losses during the creation and transport of the photoelectron to the surface. In other words, the inelastic mean free path of the electron λ_{FP} inside the sample is assumed to be infinite. However, this is not true in real cases, where λ_{FP} is shown to depend strongly on its kinetic energy. Curiously, data taken for various materials, plotted in Fig. 2.4, follow a "universal curve", represented by the black line. For photoelectrons with kinetic energies smaller than $\sim$ 10 eV, and greater than $\sim$ 1 keV, the mean free paths are much larger than typical lattice constants, which means that there is a high chance of detecting electrons without loss of energy coming from the bulk of the sample or, in other words, the spectrum is said to be *bulk sensitive*. On the other hand, when the mean free path is only a few lattice constants (for E_K between 10 eV and 1 keV), the spectrum is said to be *surface sensitive*

2.3 X-ray Absorption Spectroscopy

The X-ray absorption spectroscopy is a widely used technique, capable of probing the element-selective density of unoccupied states of matter, projected onto the orbital symmetry allowed by selection rules. The experiment is performed exposing the sample to photons of known and variable energy. At a determined energy, E_{edge}, the absorption

rate rises significantly, thus defining an absorption edge. Incoming photon energies higher than E_{edge} are enough to excite an electron of a determined core level to the conduction band, leaving a core hole behind. If the transmission coefficient of the sample at the used photon energy is large enough, it is possible to perform the measurement by detecting the transmitted X-rays as a function of the incident energy, and hence obtain the absorption coefficient of the sample. However, in a number of cases, the detection must be indirect (see Figure 2.5).

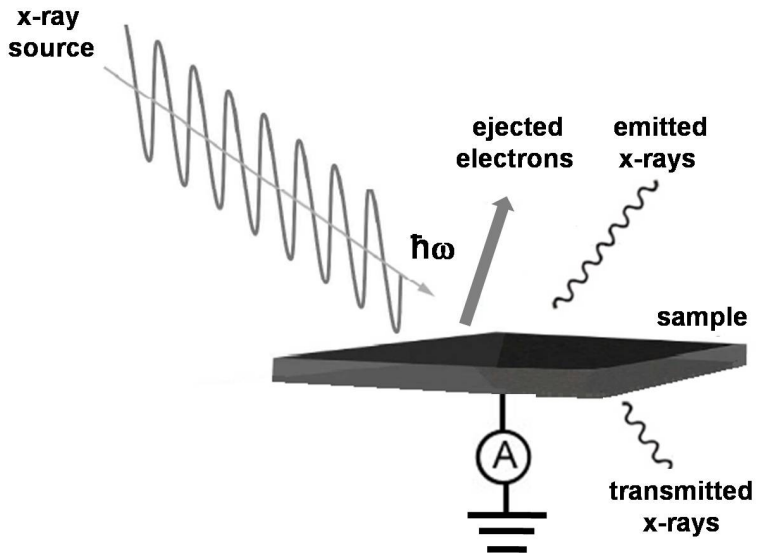

Figure 2.5 Scheme of the XAS technique. The X-ray source emits photons which are absorbed, promoting a core electron to the conduction band. The system can relax by emitting a X-ray photon or a electron.

After the absorption of the photon, the core hole lives for $\sim 10^{-15}$ s before it decays by either the emission of a photon, in a process called *fluorescence*, or the emission of an electron from a core or valence state, in a process called *Auger decay* [20]. These decay processes are depicted in Fig. 2.6 and summarized in equations 2.15 and 2.16, in which $\underline{c}$ represents a core hole.

$$|d^n\rangle + \hbar\omega \rightarrow \underline{c}\,|d^{n+1}\rangle \rightarrow |d^n\rangle + \hbar\omega \text{ (fluorescence)} \tag{2.15}$$

$$|d^n\rangle + \hbar\omega \rightarrow \underline{c}\,|d^{n+1}\rangle \rightarrow |d^{n-1}\rangle + e^- \text{ (Auger)} \tag{2.16}$$

Figure 2.7 shows the percentage of fluorescence signal of the $1s$ absorption for selected elements, as function of its binding energy, indicating some reference elements. According to the Figure, until Zn (Z = 30, Zn $1s \sim 10$ keV), the Auger decay is responsible for more than 50% of the relaxation processes [20]. In both cases, the number of emitted photons

(fluorescence) or particles (Auger) is proportional to the number of allowed unoccupied states for the primary excitation, *i.e.* absorption of the photon. When the detected signal are the X-rays, the method is called *fluorescence yield* (FY). It is also possible to ground the sample and measure the charge needed to neutralize it after the emission of all electrons, which is called the *total electron yield mode* (TEY). The probing depth of the TEY mode varies from one to a few nanometers depending on the material studied [20; 52].

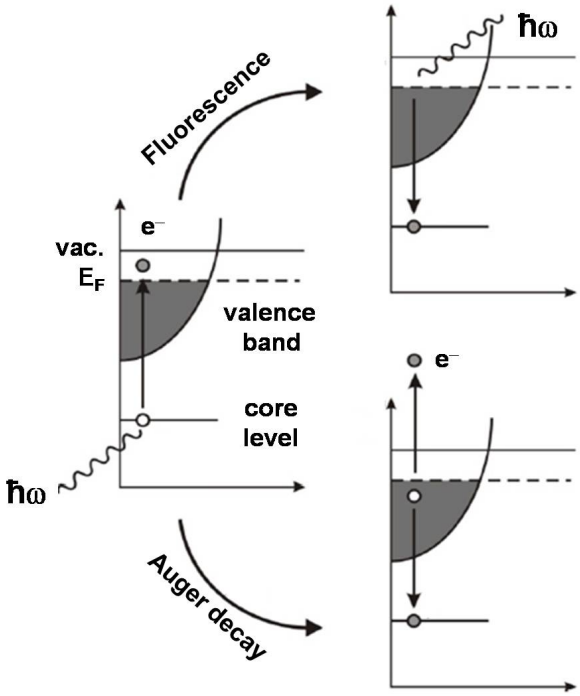

Figure 2.6 Representation of the fluorescence and Auger decay processes. After the absorption of the photon, the system decays by either the emission of a photon (fluorescence), or by an electron from a core or valence state (Auger decay).

The rate of the primary excitation, *i.e*, the rate of absorption of the incident photon by a core electron, is given by 2.17:

$$I(\omega) \propto \sum_f |\langle \underline{c} d_f^{n+1}| (\boldsymbol{A_0} \cdot \hat{\boldsymbol{P}}) |d^n\rangle|^2 \delta(E_{n+1} - E_n - \hbar\omega), \tag{2.17}$$

where the initial and final state wave functions can be separated into the radial and angular parts and calculated with the Wigner-Eckart theorem [20]. The radial part contributes with the line strength of the transition, while the angular parts give rise to the *dipole selection rules*, which states that the total angular momentum J of initial and final states must differ by $\Delta J = \pm 1$.

The case of an absorbing s level is simpler than other levels, because in this case the overlap between core and valence wave functions is smaller than the conduction band width, and overlap effects can be neglected. Hence, the initial and final wave functions can

be treated in a single-electron approach, and the XAS spectrum simply reflects ground state projected in the unoccupied states allowed by the selection rules, which in this case are mostly of p orbitals.

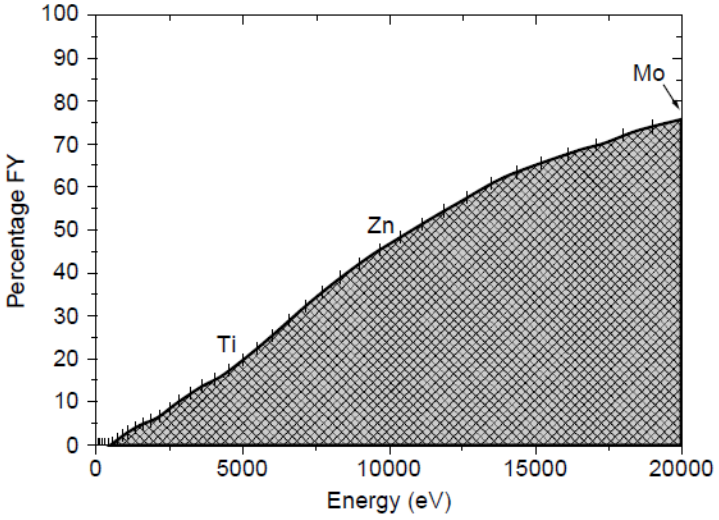

Figure 2.7 Fluorescence yield signal as function of the binding energy of the 1s level. Selected elements are highlighted. Extracted from [20].

2.4 Resonant X-ray Photoemission Spectroscopy

The Resonant X-ray Photoemission Spectroscopy (RPES) relies on a combination of the PES and XAS techniques already described. In RPES, the direct photoemission channel and the Auger decay (shown in equations 2.18 and , both leading to the same final states) interfere with each other, resulting in changes of the RPES intensity as a function of the incident energy.

$$|\varphi_{n\mathbf{k}}\rangle\,|d^n\rangle + \hbar\omega \rightarrow |\mathbf{k}\rangle\,|d^{n-1}\rangle \ \text{(direct channel)} \tag{2.18}$$

$$|d^n\rangle + \hbar\omega \rightarrow \underline{c}\,|d^{n+1}\rangle \rightarrow |d_f^{n-1}\rangle + e^- \ \text{(indirect channel)} \tag{2.19}$$

The term *resonant* is employed because the energy of the incident photon can be conveniently tuned to match an absorption edge of one of the elements in the sample. If $\hbar\omega$ is smaller than this threshold, $E_{threshold}$, only the direct channel will contribute. In other words, a conventional XPS measurement is performed, and in the RPES context this is called the *off-resonance* condition. On the *on-resonance* condition, when $\hbar\omega > E_{threshold}$, the Auger decay of this specific atom becomes energetically allowed, and it can also contribute to the signal detected in the electron analyzer. The difference between the on–off spectra yields the signal from the $d^n \rightarrow d^{n+1}$ excitation. This technique allows to separate

the contribution of the selected element to the photoemission spectrum, which makes this technique useful to identify the partial character of specific elements in the spectrum, as depicted in Fig. 2.8.

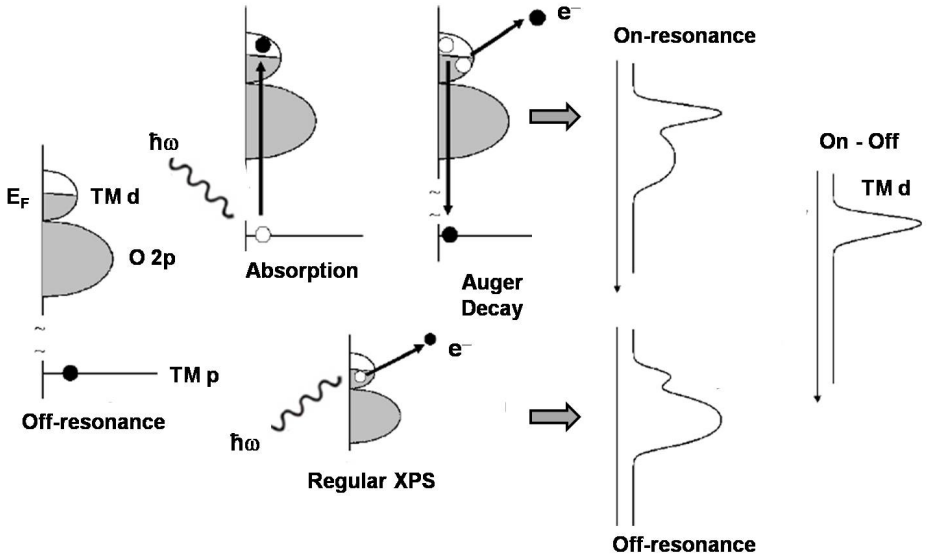

Figure 2.8 Schematic view of the RPES technique. The off-resonance spectrum is a regular XPS spectrum, while the on-resonance spectrum is measured with an incident photon energy that matches an absorption edge of one of the elements in the sample. The difference spectrum results in the partial contribution of the selected element to the spectrum.

2.5 Measurements

As mentioned in Chapter 1, X-ray spectroscopic techniques greatly benefited from the construction of synchrotron accelerators and all the interesting properties of the radiation produced by them. All the spectroscopic measurements presented herein were performed at the UVX source of the Brazilian Synchrotron Light Laboratory (LNLS), whose overview is shown in Fig. 2.9. The UVX source was inaugurated in 1997, and is composed a sequence of straight sections where the electron beam travels, intercalated with magnets and arrays of magnets (*bending magnets* and *insertion devices*, respectively) that make the electrons bend their trajectories and emit X-rays. The radiation beam is emitted tangential to the trajectory of the electron beam and treated by an optical system to become suitable to be used in experiments.

The X-ray Photoemission Spectroscopy (XPS) measurements were performed at the SXS beamline [53], under project No. SXS–17731. The SXS beamline operates in the tender X-ray range (1-5 keV), it is based on a bending magnet of 1.6 T, and uses a water

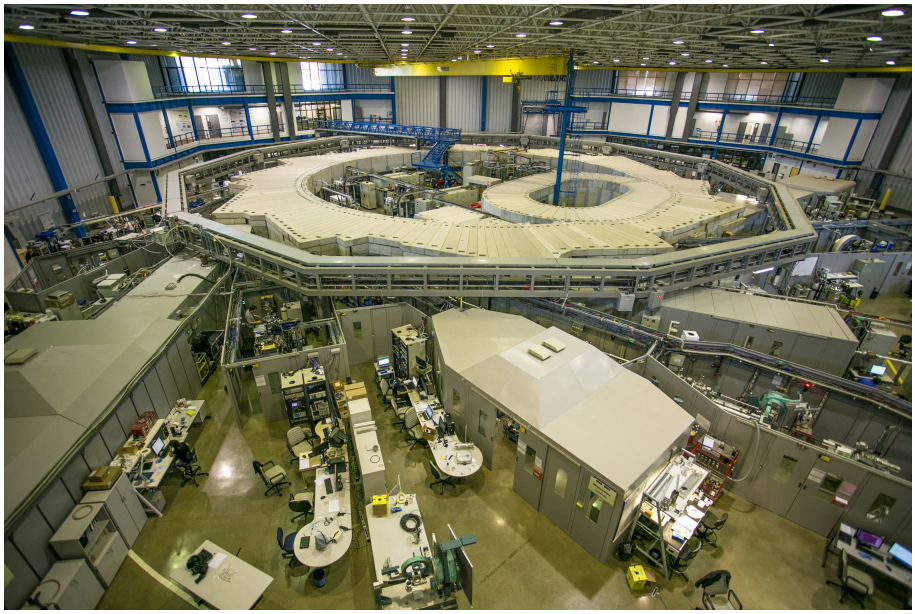

Figure 2.9 Overview of the UVX source of the Brazilian Synchroton Light Laboratory (LNLS) - Campinas - Brazil.

cooled double-crystal monochromator with different crystals depending on the energy and a Ni coated toroidal mirror for vertical and horizontal focalization. The beamline delivers a flux density at the sample of $4{\times}10^{11}$ photons/s/mm2 with photons of 3 keV, with and energy resolution of ΔE/E of 10^{-4} and a beam size of 0.6 $\times$ 1.2 mm^2 at the sample. The XPS endstation is equipped with a Phoibos 150 hemispherical electron analyzer from SPECS, a Flood Gun FG15/40 (used to neutralize charges in insulating samples) from SPECS [44].

The photon energies used for the measurements are listed on Table 2.1, along with the respective double crystal used in the monochromator. The best compromise between the signal-to-noise ratio and the experimental resolution was achieved with an analyzer pass energy of 10 eV and an exit slit of 0.5 μm. For the band insulator $SrTiO_3$, the Flood Gun was used, emitting a current of 6 nA with electrons of 150 eV onto the sample. All spectra were acquired at room temperature with the base pressure around 1.0×10^{-9} mbar.

With the photon energies used, the photoelectron escape depth is around 30 Å [54], which makes the signal less surface sensitive than usual PES measurements, with smaller photon energies. The Fermi level was calibrated using a clean Au foil, and a shift of 0.4 eV in all spectra were needed.

The X-ray Absorption Spectroscopy (XAS) was performed at the PGM beamline, under project No. PGM–17732. The PGM beamline operates in the 100 to 1500 eV range, and its source is an elliptical undulator: an insertion device composed of a periodic array of

Table 2.1: Photon energies used in the X-ray Photoemission measurements of the $SrTi_{1-x}Ru_xO_6$ and $Sr_2YRu_{1-x}Ir_xO_6$ series (in eV).

	$SrTi_{1-x}Ru_xO_6$	$Sr_2YRu_{1-x}Ir_xO_6$	Double crystal
Core level XPS	1840	1840	InSb
Valence band XPS	2830	2830	Si(111)
Ru L_3 RPES	2841.8	2840.6 and 2843.8	Si(111)

dipole magnets with alternate polarities, which force the electrons to undergo oscillations, producing more photons, while also allowing the photon polarization to be switched among linear horizontal, linear vertical or circular. The beamline is equipped with a Au coated plane grating monochromator, a water cooled Au coated toroidal mirrors for focusing. The flux at the sample if of $10^{11} - 10^{13}$ photons/s with a beam size of 0.1×0.5 mm^2 at the sample, achieving an energy resolution of $\Delta E/E \approx 10^{-3}$ -10^{-4} [55].

The O 1s level XAS measurements were performed in total electron yield mode, using a Keithley 6514 electrometer as detector, with incident photons with energies from 525 to 555 eV. The energy resolution achieved was approximately 0.4 eV, limited by the detection mode rather than the beamline. The TEY mode has a probing depth up to 30-100 Å, depending on the sample [20]. The photon energy scale was calibrated using known absorption edges of reference samples. The samples were scraped with a diamond file to remove surface contamination. All spectra were acquired at room temperature with the base pressure around 1.0×10^{-9} mbar.

3 Theoretical Methods

This Chapter presents the theoretical methods used to interpret the experimental data obtained with the techniques described in the previous Chapter. Firstly, the Cluster and Double Cluster models, which will be used to study the $SrTi_{0.5}Ru_{0.5}O_3$ series, are presented. The Cluster model consists of a model Hamiltonian that treats many-body effects exactly and ultimately aims at calculating the spectral weight. The second part of this Chapter describes the Density Functional Theory, which treats the many-body interacting problem in terms of its electronic density. Then, the WIEN2k package will be presented, which was used to calculate the ground state properties and electronic structure of the $Sr_2YRu_{1-x}Ir_xO_6$. The chapter ends with a discussion on how to use the results of the (Double) Cluster model and DFT approaches to study electronic structure of TMO's. In particular, the convenience of using each theoretical method to interpret the XPS and XAS spectra is pointed out.

Contents

3.1 Cluster Model

3.1.1 Hamiltonian

As mentioned in the Section 1.2, in perovskites, the electronic structure around the Fermi level is dictated by states originated from the TMO_6 octahedra. Thus, the cluster

model focus on the electronic structure of a regular BO_6 octahedron, where the three O $2p_i$ ($i = x, y, z$) of the six surrounding oxygen atoms and the 5 TM d_i ($i = xy, xz, yz, z^2, x^2-y^2$) states are considered. In O_h symmetry, the 23 orbitals interact in a particular way: 13 of the resulting 23 molecular orbitals present exclusively O $2p$ character, with the A_{1g}, T_{1g}, T_{1u} e T_{2u} symmetries, and can be treated in a simpler manner. The remaining 10 states split into bonding (with mostly O $2p$ character) and anti-bonding (with mostly TM d character) molecular orbitals of the T_{2g} and E_g symmetries [56]. This situation is depicted on Fig. 3.1, in which the red and blue lines represents TM d and O $2p$ characters, respectively.

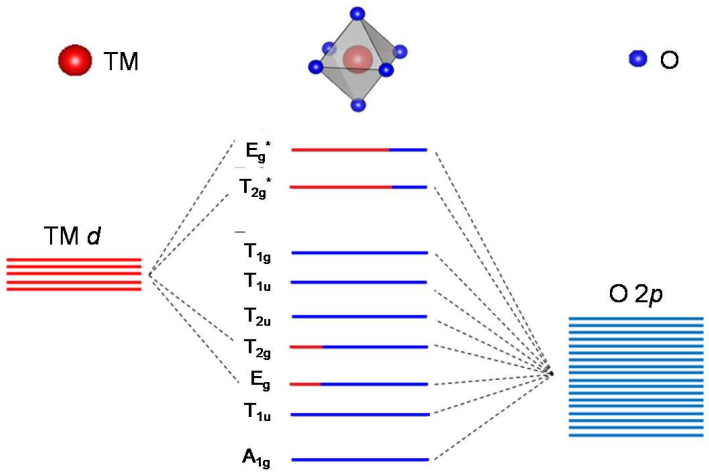

Figure 3.1 Diagram illustrating the molecular orbitals arising from the TM d–O $2p$ interaction in a TMO_6 octahedron (O_h symmetry). Only orbitals with T_{2g} and E_g symmetries present mixed TM d–O $2p$ character.

Most of the TM d character appear in the anti-bonding t_{2g} and e_g molecular orbitals, which are energetically split due to the *crystal field*. This effect stems from the geometry of the problem, and happens because 2 orbitals (z^2 and $x^2 - y^2$) point towards the oxygen atoms, while other three (xy, xz and yz) point in-between them. The difference in energy of the t_{2g} and e_g orbitals is given by $10Dq$, and has typical values of a few eV. In order to keep the energy center of the TM d band, the energy position of each t_{2g} electron is corrected in -4 Dq, while for each e_g electron is added 6 Dq, as shown in Fig. 3.2. The origin of the crystal field splitting 10 Dq is explained in details in Appendix A.

The Hamiltonian of the model includes one d site with energy ϵ_d and on-site Hubbard correlation energy U, in contact with a non-correlated O $2p$ bath with energy ϵ_p. The overlap between d and p states is given by a hybridization term T. Besides the correlation U, the model includes the other relevant local interactions, such as crystal field and intra-atomic exchange, but it does not include band dispersion effects. In general, local TMO_6 interactions play the leading role in determining the electronic structure of TMO's,

as illustrated, for instance, by the well-known example of NiO mentioned in Chapter 1.

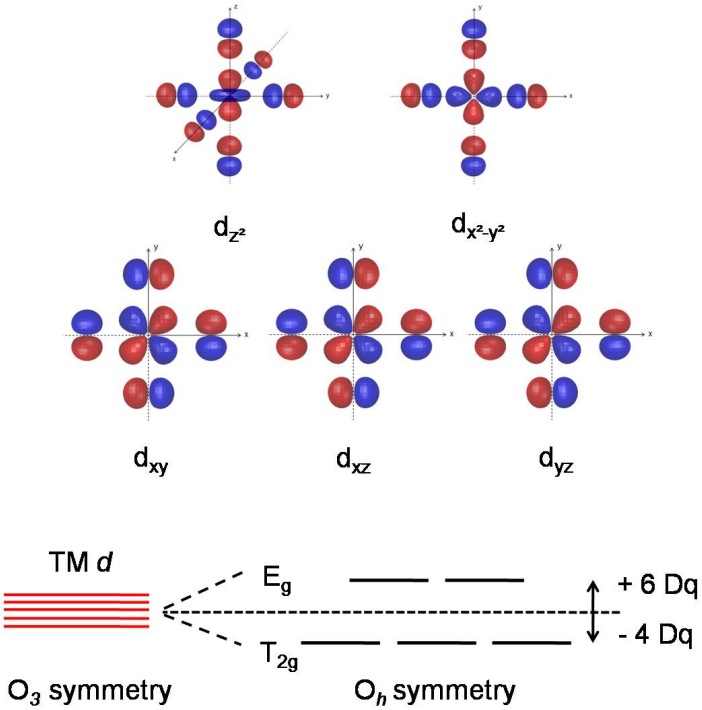

Figure 3.2 Representation of the resulting bonding molecular orbitals originated from the TM d–O $2p$ interaction in O_h symmetry. Molecular orbitals with E_g (T_{2g}) symmetry are due to TM d_{z^2,x^2-y^2} (TM $d_{xy,xz,yz}$) atomic orbitals, which form a π-character (σ-character) bond with the oxygen ions. The energy difference between the t_{2g} and e_g orbitals is 10 Dq.

Since the Cluster model aims at the correct description of electronic correlations, *i.e.*, interactions among the electrons, the convenient formalism to define its Hamiltonian is the Second Quantization, which is briefly reviewed in Appendix B. The Hamiltonian $\hat{H}_{cluster}$ reads [57]:

$$\hat{H}_{cluster} = \sum_{\nu,\sigma} \epsilon^d_{\nu,\sigma} \hat{d}^\dagger_{\nu,\sigma} \hat{d}_{\nu,\sigma} + \sum_{\nu,\sigma} \epsilon^p \hat{p}^\dagger_{\nu,\sigma} \hat{p}_{\nu,\sigma} + \sum_{\nu,\sigma} T_\nu \left(\hat{d}^\dagger_{\nu,\sigma} \hat{p}_{\nu,\sigma} + \hat{p}^\dagger_{\nu,\sigma} \hat{d}_{\nu,\sigma} \right) + \\ + \sum_{\nu,\nu',\sigma,\sigma'} (U - J\delta_{\sigma,\sigma'}) \hat{d}^\dagger_{\nu,\sigma} \hat{d}_{\nu,\sigma} \hat{d}^\dagger_{\nu',\sigma'} \hat{d}_{\nu',\sigma'}, \tag{3.1}$$

in which $\nu^{(\prime)}$ is the orbital index (t_{2g} or e_g) and $\sigma^{(\prime)}$ is the spin index; $\hat{d}^\dagger_{\nu,\sigma}$ ($\hat{d}_{\nu,\sigma}$) creates (annihilates) a d electron and $\hat{p}^\dagger$ ($\hat{p}$) creates (annihilates) a p electron. All of the creation and annihilation operators obey the fermionic commutation relations

$$\{\hat{d}^\dagger_k, \hat{d}_{k'}\} = \delta_{k,k\prime} \tag{3.2}$$

$$\{\hat{d}_k, \hat{d}_{k'}\} = \{\hat{d}^\dagger_k, \hat{d}^\dagger_{k'}\} = 0. \tag{3.3}$$

The first term of equation 3.1 computes the number of d electrons with energy $\epsilon^d_{\nu,\sigma} = \epsilon^d + (6Dq\delta_{\nu,e_g} - 4Dq\delta_{\nu,t_{2g}})$; the second term computes the number of p electrons with energy ϵ^p; the third term treats the hybridization between the O $2p$ and TM d orbitals, represented by the correspondent t_{2g} ($\nu = \sigma$) and e_g ($\nu = \pi$) parameters T_ν. These are renormalizations, due to the octahedral symmetry, of the pdσ and $pd\pi$ Slater-Koster two-center integrals [58], depicted in Figure 3.3 and defined by equations 3.4 and 3.5.

$$T_\sigma = \sqrt{3}pd_\sigma \tag{3.4}$$

$$T_\pi = -2pd_\pi \tag{3.5}$$

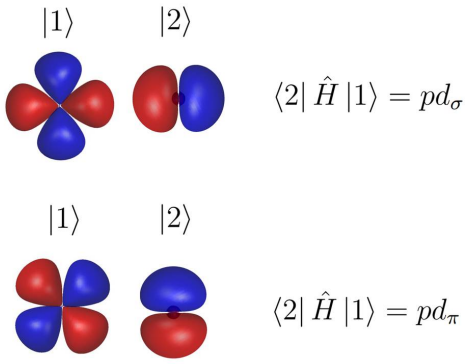

Figure 3.3 Representations of the two-center Slater-Koster integrals pdσ and $pd\pi$ and the renormalized $T_{\sigma,\pi}$ interactions in O_h symmetry.

Finally, the last term computes the number of electron pairs in the d band, adds a Coulomb repulsion energy U to each one and subtracts the intra-atomic exchange energy J to each pair of electrons with aligned spins. The terms involving $10Dq$ and J are also referred to as *multiplet* corrections.

The single-particle states are defined out of the t_{2g} triply degenerate levels with energy $\epsilon^d_{\nu,\sigma} - 4Dq$ and of the e_g doubly degenerate levels with energy $\epsilon^d_{\nu,\sigma} + 6Dq$. Starting from the vacuum level $|0\rangle$, these states are defined as:

$$t_{2g,\sigma}\begin{cases} \hat{d}^\dagger_{xy,\sigma}|0\rangle \\ \hat{d}^\dagger_{xz,\sigma}|0\rangle \\ \hat{d}^\dagger_{yz,\sigma}|0\rangle \end{cases} \qquad e_{g,\sigma}\begin{cases} \hat{d}^\dagger_{z^2,\sigma}|0\rangle \\ \hat{d}^\dagger_{x^2-y^2,\sigma}|0\rangle \end{cases} \tag{3.6}$$

The many-particle state is defined through the direct product (whose sign has been omitted) of the single particle states and labeled via the occupation number of each of the single particle states. For instance, a many-body state of a d^3 orbital can be written as:

$$|d^3\rangle = \hat{d}^\dagger_{xy,\uparrow}\hat{d}^\dagger_{xz,\uparrow}\hat{d}^\dagger_{yz,\uparrow}|0\rangle = |1110000000\rangle \tag{3.7}$$

3.1.2 Configuration Interaction Method

In the Cluster model, charge transfer effects are included through fluctuations from the O $2p$ orbitals to the TM d site. The ground state wave function is then expanded beyond the ionic configuration d^n into configurations in which one or more electrons have been transferred to one of the available TM d orbitals, represented by $\mathrm{d}^{n+1}\underline{\mathrm{L}}$, $\mathrm{d}^{n+2}\underline{\mathrm{L}}^2$, etc, where $\underline{\mathrm{L}}$ denotes a hole in the ligand band. This approach is known as *configuration interaction method* [59; 60]. The complete expansion of the ground state wave function for the above $|d^3\rangle$ example reads:

$$|\psi_{GS}\rangle = \alpha\,|d^3\rangle + \beta\,|d^4\underline{\mathrm{L}}\rangle + \gamma\,|d^5\underline{\mathrm{L}}^2\rangle + ... + \zeta\,|d^{10}\underline{\mathrm{L}}^7\rangle \tag{3.8}$$

where the $\mathrm{d}^{3+p}\underline{\mathrm{L}}^p$ states are obtained from 3.7 by distributing p electrons into the remaining orbitals.

Now that the Hamiltonian and the many-particle basis are defined, it is possible to present some typical matrix elements of $\hat{H}_{cluster}$:

$$\langle d^n|\,\hat{H}_{cluster}\,|d^n\rangle = n\epsilon_d + \frac{n(n-1)}{2}U + E_{d^n\ mult.} \equiv 0 \tag{3.9}$$

$$\langle d^{n+1}\underline{\mathrm{L}}|\,\hat{H}_{cluster}\,|d^{n+1}\underline{\mathrm{L}}\rangle = \Delta + E_{d^{n+1}\ mult.} \tag{3.10}$$

$$\langle d^{n+2}\underline{\mathrm{L}}^2|\,\hat{H}_{cluster}\,|d^{n+2}\underline{\mathrm{L}}^2\rangle = 2\Delta + U + E_{d^{n+2}\ mult.}, \tag{3.11}$$

where the multiplet corrections have been reduced to $\mathrm{E}_{d^{n,n+1,n+2}\ mult.}$ for simplicity.

These terms can be easily interpreted in terms of the charge transfer energy Δ, defined as $\Delta = \epsilon^d - \epsilon^p + nU$. Disregarding the multiplet corrections and taking the d^n configuration as the zero energy, the first electron transferred to the TM site adds Δ to the TM site energy. The second adds another Δ plus the U interaction with the first extra electron, and so on.

The cluster model includes parameters which need to be determined as to reproduce the experimental spectra as closely as possible. However, it is desirable to have estimates of those parameters *a priori*. Once the systematic of the parameters are understood in terms of properties of the ions, such as nominal valence and electronegativity, we are able to define a physical acceptable range to vary them and, to some extent, predict some properties of the electronic structure. Several studies from the late 1980's and early 1990's compose the basis of the current understanding of how the main parameters of the model, U, Δ and T_σ, change across the $3d$ transition metal series, for different stoichiometries, nominal valences and types of ligand anions.

The estimates for U, Δ and T_σ obtained from the analysis of XPS spectra may yield somewhat different parameters, but the systematic trend for their variations is accepted with respect to the TM and the ligand anion. After the analysis of several TM compounds, Zaanen *et al.* [61] highlighted that the relative values of U and Δ have a decisive role on the electronic structure of insulating TM compounds. Particularly, this work presents a diagram in the (U, Δ) parameter space, widely known as the Zaanen-Sawatzky-Allen (ZSA) diagram, in which regions are defined with different properties of the gap and low-energy excitations. Figure 3.4 reproduces three main regions of the ZSA diagram, which are explained below, although it should be noted that the original diagram much more richer than than the adaptation presented here.

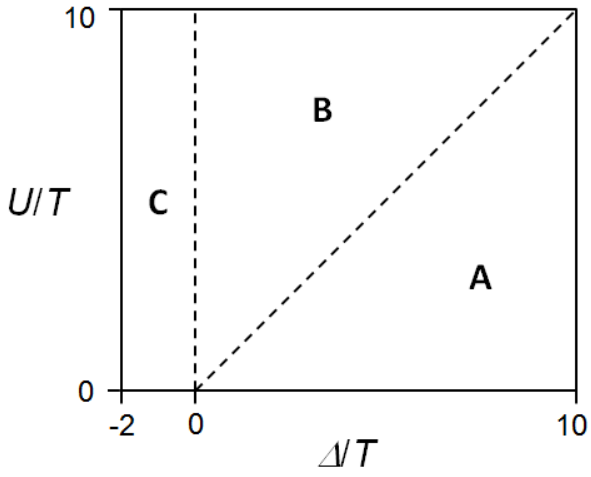

Figure 3.4 Illustration of three regions of the Zaanen-Sawatzky-Allen (ZSA) diagram. Region A (*Mott-Hubbard* regime): $\Delta > U$, gap $\propto U$, charge excitations of the $d \rightarrow d$ type; Region B (*Charge Transfer* regime): $\Delta < U$, gap $\propto \Delta$, charge excitations $p \rightarrow d$ kind; Region C (*Negative Charge Transfer* regime): $\Delta < 0$, gap $\propto \Delta$, charge excitations are of the $p \rightarrow p$ kind.

In region A, where where $\Delta > U$, the gap is proportional to U and the lowest-lying charge excitations are of the $d \rightarrow d$ type, *i.e.*, from occupied to unoccupied TM d states; this type of compound is said to be in the *Mott-Hubbard* regime. In region B, where $0 < \Delta < U$, the gap is proportional to Δ, and the lowest charge excitations are of the $p \rightarrow d$ kind, from occupied O $2p$ to unoccupied TM d states; this type of compound is said to be in the *Charge Transfer* regime. There is also the possibility that Δ assumes negative values, leading to the *Negative Charge Transfer* regime, where the charge gap is proportional to Δ and the lowest charge excitations are of the $p \rightarrow p$ kind.

Figure 3.5 depicts the differences among the electronic structures in the three different regimes. As in Figure 1.5, TM states are depicted in red, O $2p$ states in blue, and occupied (unoccupied) bands as solid (open) rectangles and the dashed line represents the Fermi energy E_F. In the Mott-Hubbard regime, since $\Delta > U$, the occupied states close

to E_F are of TM d character, occupied and unoccupied, whereas the O $2p$ band appears far from E_F. In the Charge Transfer regime, since $\Delta < U$, states with O 2p states appear close to E_F, while also mixed with TM d states at the bottom of the valence band, whereas the region above E_F remains dominated by TM d states. Finally, in the Negative Charge Transfer regime, with $\Delta < 0$, the transfer of a O $2p$ electron to the TM d band is highly favorable, which places the occupied portion of the O $2p$ band close to E_F and pushes the TM d states to more negative energies (including the bottom of the valence band), while the region above E_F presents both TM d and O $2p$ character [62].

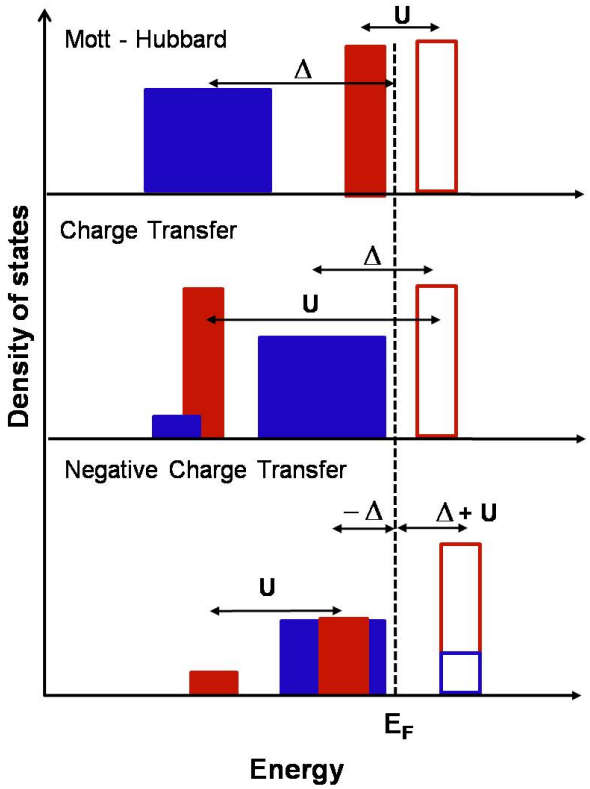

Figure 3.5 Schematic views of the electronic structures of TMOs in the Mott-Hubbard, Charge Transfer and Negative Charge transfer regimes.

There is a general consensus on the fact that late $3d$ TMO's are charge transfer insulators, such as CuO, NiO, CoO and the CuO_2 plane in high-T_C cuprates [60; 63–65]. Early $3d$ TMO's have long been thought to be of Mott-Hubbard type, but studies have shown that they are in fact in the Charge Transfer regime [34]. Moreover, the regions of the diagram and the correspondent analysis also hold for metals, except of course for the prediction of the gap.

In order to illustrate how the *a priori* knowledge of the parameters may help, consider the change U in the $3d$ TM series and for different structures and stoichiometries, extracted from Bocquet *et al.* [66] and presented in Fig. 3.6. The values of U in the $SrMO_3$ perovskite structure, open squares, show an increase from 4.5 eV in Ti (nominally d^0 in

this stoichiometry), to a plateau close to 8 eV for Mn (d^3) and Fe (d^4). If the value of U_{Ru} in the same kind of compound had to be estimated, U_{Fe} would serve as an upper limit to U_{Ru}, because Fe^{4+} and Ru^{4+} possess the same number of electrons in the d shell, and the larger spacial extension of the Ru $4d$ orbitals would result in a smaller electronic correlation in such orbital. Indeed, the values found for U_{Ru} in Guedes *et al.* [35] is 4.0 eV.

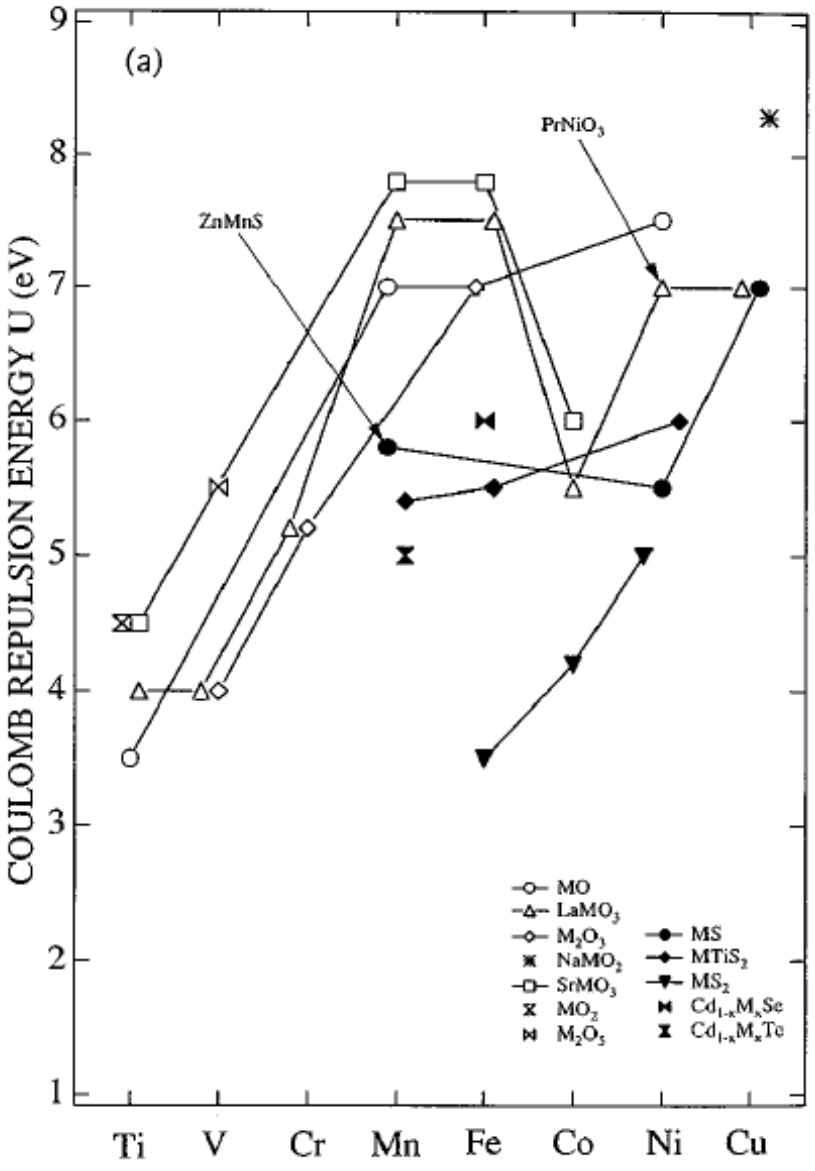

Figure 3.6 Estimates of the Hubbard U value in the $SrTMO_3$ perovskite series, for various TMs. Extracted from Bocquet *et al.* [66].

3.1.3 Nonlocal Screening

The cluster model is ultimately based on the Hubbard model, which was initially conceived to describe the Mott state in transition metal oxides. The electronic states of

metals, however, present a key ingredient, absent in insulators, which are the delocalized states at the Fermi level. Since these states have been shown to manifest in core level and valence band photoemission spectra [67], besides the local screening (from the O $2p$ band), a nonlocal screening channel (also called the *coherent* band) may be included in the description of metallic systems. [67; 68]. In such cases the model is also known as the *Extended* Cluster model, and the following terms must be added to the Hamiltonian:

$$\hat{H}_{nonlocal} = \sum_{\nu,\sigma} \epsilon^c \hat{c}^\dagger_{\nu,\sigma} \hat{c}_{\nu,\sigma} + \sum_{\nu,\sigma} T^* \left(\hat{d}^\dagger_{\nu\sigma} \hat{c}_{\nu,\sigma} + \hat{c}^\dagger_{\nu,\sigma} \hat{d}_{\nu,\sigma} \right), \tag{3.12}$$

where $\hat{c}^\dagger_{\nu\sigma}$ ($\hat{c}_{\nu\sigma}$) creates (annihilates) a coherent electron with energy ϵ^c, and T^* is the coherent band – d band transfer integral. Here, the ν is the orbital index (t_{2g} or e_g) allowed for the coherent band, and $\sigma(\prime)$ is the spin index. Please note that $\hat{H}_{coherent}$ possess the same form of the second and third terms of 3.1, and can be interpreted similarly: the first term of $\hat{H}_{coherent}$ computes the number of coherent electrons with energy ϵ^c, and the second treats the hybridization between the TM d and coherent bands, with transfer integral T^*. Now, besides the basis configurations from equation 3.12, the expansion of $|\psi_{GS}\rangle$ must also include configurations such as:

$$|\psi^{nonlocal}_{GS}\rangle = \beta\, |d^{n+1}\underline{\mathrm{C}}\rangle + \gamma\, |d^{n+2}\underline{\mathrm{C}}^2\rangle + \delta\, |d^{n+2}\underline{\mathrm{LC}}\rangle + ..., \tag{3.13}$$

where $\underline{\mathrm{C}}$ denotes a hole in the coherent band.

3.1.4 Spectral Weight

The XPS and XAS techniques measure a response of the system to some excitation. Therefore, besides calculating the N-particles ground state, it is necessary to find the final states of the system upon the excitation promoted by each technique.

In core level XPS, the final state has a localized core level hole that presents an attractive potential to the valence electrons. Hence, when constructing the core level final state Hamiltonian $\hat{H}_{CS}$, it is included an attractive term $Q = U/0.83$, which was obtained empirically, for each electron in the TM d site [69]. In this case, since the experimental technique probes the core level, the valence band basis is the same as the ground state basis. The effect of the spin-orbit interaction in core states is to split the level into two components with different values of total angular momentum $|\ell - s| \geq j \leq \ell + s$, where $s = 1/2$ is the spin quantum number for electrons. For instance, a $2p$ ($\ell = 1$) core level is split into $2p_{3/2}$ ($j = \ell + 1/2$) and $2p_{1/2}$ ($j = \ell - 1/2$); the $j = \ell - s$ component appear in at a higher binding energy than the $j = \ell + s$ component by $\xi_{n\ell}$, which is the SO splitting of the $n\ell$ level, and with renormalized intensity relative to the $j = \ell + s$ component.

Although this effect can be formally treated in the Hamiltonian, it was included in the Cluster model by simply recalculating the spectrum with a shift of $\xi_{n\ell}$, obtained from the experiment, and renormalizing the calculated spectral weight (in the case of p levels, the $j = 1/2$ component has half the integral of the $j = 3/2$).

In valence band XPS, the n final state Hamiltonians $\hat{H}_{RS}^{1,2,..,n}$ (where RS stands for removal state) are calculated with $n-1$ electrons basis sets, generated upon the individual removal of each the n electrons in the ground state d^n configuration. Each eigenvector of the $\hat{H}_{RS}^{i}$ corresponds to a possible final state achieved by the system after ejection of the photoelectron. Similarly, the $n+1$-electrons basis are generated by adding individual electrons to the $10-n$ available states of the ground state d^n configuration, and then are used to calculate the $10-n$ addition state (AS) $\hat{H}_{AS}^{1,2,...,10-n}$ Hamiltonians. Each eigenvector of $\hat{H}_{AS}^{i}$ corresponds to a possible final state achieved by the system after the addition of an electron to the conduction band. In this case, it is implicit that core hole and the valence band wave function do not overlap, which is valid for absorption of s levels. The spectral weight is then obtained by the following Fermi's Golden Rule:

$$A(\varepsilon) = \sum_{f} |\left\langle \Psi_f \right| \hat{O} \left| \Psi_i \right\rangle|^2 \delta(\varepsilon \pm (E_f - E_{GS})), \tag{3.14}$$

where the $\pm$ sign depends on whether the different $|\psi_f\rangle$ are eigenstates with $n-1$ (CS and RS) or $n+1$ (AS) particles. $\hat{O}$ is an operator set appropriately to each technique: for core level XPS, it annihilates a core electron; for valence band XPS, it may annihilate TM d and O $2p$ electrons; for the O $1s$ XAS, it creates an electron in the O $2p$ band.

The spectrum is a collection of Dirac's delta functions, with intensities given by the probability of transitioning from an initial state $|\psi_{GS}\rangle$ to a final state $|\psi_f\rangle$, given the absorption of an X-ray photon. Finally, the results are convoluted with Gaussian and Lorentzian profiles to simulate band dispersion as well as lifetime and experimental broadening effects, respectively.

In order to illustrate this fact, Figure 3.7 presents the Ni $2p_{3/2}$ core level spectrum of NiO, where the Ni^{2+} presents ionic configuration d^8. The $2p_{1/2}$ component does not appear in this energy range because ξ_{2p} is large in this compound. Without taking into account the many-body effects, Koopmans' theorem states that the spectrum should present only one peak at $E_B = E_{2p_{3/2}}$, although four structures are visible in the spectrum and are labeled as A, A′, B and C.

The structures in the spectrum are interpreted as being different ways of the system to screen the core hole. Peak A is composed by states where the screening comes from an O $2p$ electron, represented by the configuration $\underline{\mathrm{c}}3\mathrm{d}^9\underline{\mathrm{L}}$ (where $\underline{\mathrm{c}}$ denotes a core hole); peak B is due to the screening with two electrons from the O $2p$ band, represented by

the configuration $\underline{c}3d^10\underline{L}^2$; the tail labeled as C is due to final states were the core hole remain unscreened, represented by the configuration $\underline{c}3d^8$. Peak A′ is due to screening from the surface of the material [70], and can be regarded as a nonlocal screening in the sense of the coherent screening from Section 3.1.3, although it is not discussed further in this thesis.

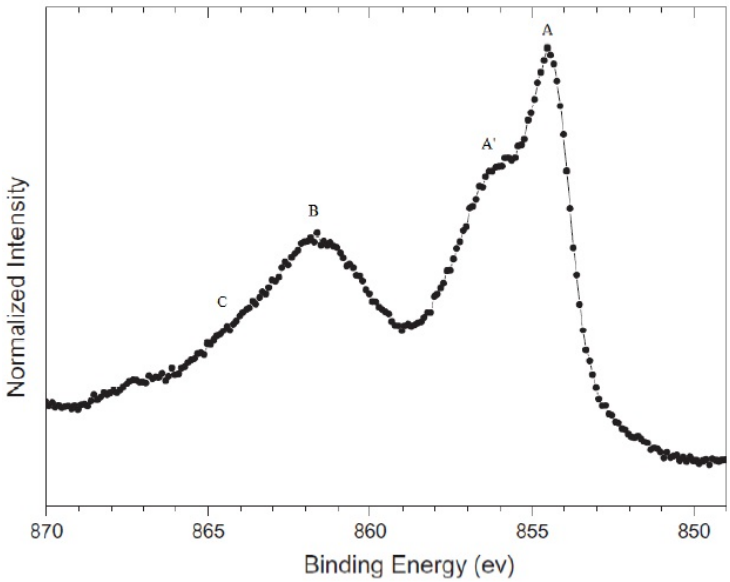

Figure 3.7 Ni $2p_{3/2}$ XPS spectrum of NiO. The peaks represent different reactions of the system to the creation of the core hole.

3.1.5 Double Cluster Model

The double cluster model considered here consists of solving two TMO_6 octahedra joined by the vertex, with distinct ionic d^m and d^n configurations, which interact through the shared oxygen atom. The Hamiltonian $\hat{H}_{DC}$ is simply the sum of the Hamiltonians of the two ions:

$$\begin{aligned}\hat{H}_{double} = &\sum_{M,\nu,\sigma} \epsilon^d_{M,\nu,\sigma} \hat{d}^\dagger_{M,\nu,\sigma} \hat{d}_{M,\nu,\sigma} + \sum_{M,\nu,\sigma} \epsilon^p \hat{p}^\dagger_{M,\nu,\sigma} \hat{p}_{M,\nu,\sigma} + \\ &+ \sum_{M,\nu,\sigma} T_{M,\nu} \left(\hat{d}^\dagger_{M,\nu,\sigma} \hat{p}_{M,\nu,\sigma} + \hat{p}^\dagger_{M,\nu,\sigma} \hat{d}_{M,\nu,\sigma} \right) + \\ &+ \sum_{M,\nu,\nu',\sigma,\sigma'} (U_M - J_M \delta_{M,\sigma,\sigma'}) \hat{d}^\dagger_{M,\nu,\sigma} \hat{d}_{M,\nu,\sigma} \hat{d}^\dagger_{M,\nu',\sigma'} \hat{d}_{M,\nu',\sigma'},\end{aligned} \tag{3.15}$$

in which the creation/annihilation operators and the parameters are the same as in equation 3.1, except for the index M, which indicates the correspondent transition metal ion.

Please note that the O $2p$ band energy ϵ^p does not depend on M, or in other words, both TM sites are in contact the same O $2p$ band. Typical matrix elements of $\hat{H}_{DC}$ are:

$$\langle d^n d^m | \hat{H}_{DC} | d^n d^m \rangle = n\epsilon_{d1} + m\epsilon_{d2} + \frac{n(n-1)}{2}U_1 + \frac{m(m-1)}{2}U_2 + E_{d^n d^m \ mult.} \equiv 0 \tag{3.16}$$

$$\langle d^{n+2}\underline{\mathrm{L}}^3 d^{m+1} | \hat{H}_{DC} | d^{n+2}\underline{\mathrm{L}}^3 d^{m+1} \rangle = 2\Delta_1 + U_1 + \Delta_2 + E_{d^{n+2}d^{m+1} \ mult.} \tag{3.17}$$

Again, it is convenient to define the charge transfer energy $\Delta_M = \epsilon_M^d - \epsilon^p + nU_M$.

The interaction between the two octahedra is included in the basis set used in the double cluster model. The basis elements of the form $\{d_1^{m+r}\underline{\mathrm{L}}^{p+r}d_2^{n+p}\}$ are obtained by direct the product of both TM's basis, with the addition of configurations where the TM ions exchanged one electron through the shared oxygen, in the process

$$d^n d^m \rightarrow d^{n+1}\underline{\mathrm{L}}d^m \rightarrow d^{n+1}d^{m-1}. \tag{3.18}$$

Then, for two ionic configurations d_1^0 and d_2^4, and supposing that coherent states populate only the d_2 site, the new basis is given by states such as $d_1^{0+r}\underline{\mathrm{L}}^{p+r}\underline{\mathrm{C}}^q d_2^{4+p+q}$, which is exactly to the basis set used to study the $SrTi_{1-x}Ru_xO_3$ series in Section 4. Hence, the Double Cluster model includes fluctuations from a ligand O $2p$ band, a coherent nonlocal band and fluctuations from the adjacent octahedron, as depicted in Fig. 3.8.

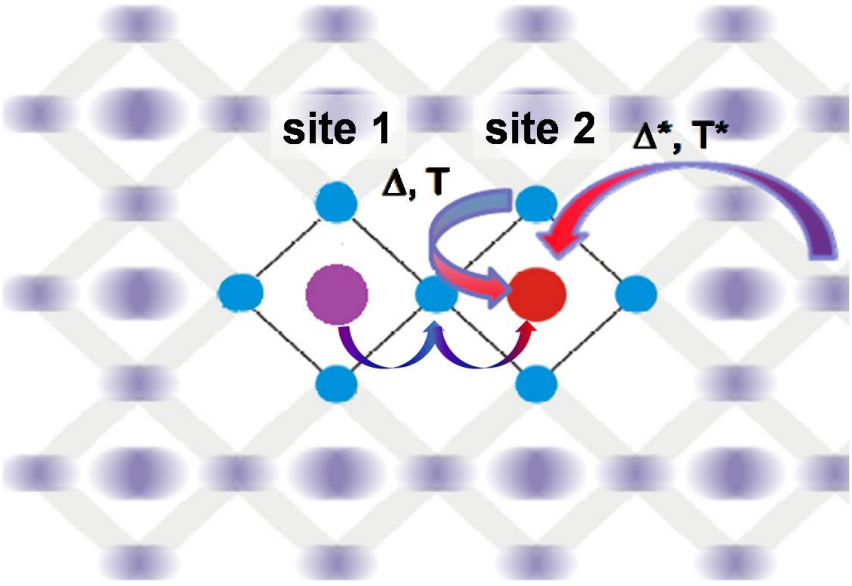

Figure 3.8 Representation of the charge fluctuations present in the Double Cluster model: from a ligand O $2p$ band; from a coherent nonlocal band; from the adjacent octahedron.

Finally, when calculating the spectral weight with equation 3.14, the $\hat{O}_f$ operators and the final states $\langle \Psi_f |$ gain a TM index, *e.g.* $\hat{d}^1_{core}$ and $\langle \Psi^1_f |$, which annihilates a core electron in site 1.

3.2 Band Structure Calculations

3.2.1 Density Functional Theory

A crystalline solid is a collection of the order of 10^{23} atoms/cm^3, arranged in a well-defined pattern by the periodic repetition of a unit called *unit cell*. Its complete description should contain the interactions between the nuclei of different atoms, the nuclei and the electrons, and the electrons with themselves, which characterizes a many-body problem. In the case of M nuclei and N electrons, the Hamiltonian for the solid, in atomic units ($\hbar = e = m_e = 1$), is given by [71]:

$$\hat{H}_T = -\frac{1}{2}\sum_{i}^{M}\frac{\nabla^2_{\boldsymbol{R_i}}}{M_i} - \frac{1}{2}\sum_{i}^{N}\nabla^2_{\boldsymbol{r_i}} - \sum_{i,j}^{M,N}\frac{Z_i}{|\boldsymbol{R}_i - \boldsymbol{r_j}|} + \frac{1}{2}\sum_{\substack{i,j\\ j\neq i}}^{N}\frac{1}{|\boldsymbol{r}_i - \boldsymbol{r}_j|} + \frac{1}{2}\sum_{\substack{i,j\\ j\neq i}}^{M}\frac{Z_i Z_j}{|\boldsymbol{R_i} - \boldsymbol{R_j}|}, \tag{3.19}$$

where $\mathbf{r_i}$ and $\mathbf{R_i}$ are the electronic the nuclear coordinates, respectively; M_i and Z_i are the i-th nucleus mass (in atomic units) and charge. The values of M_i are typically 10^3 times greater than the electron mass M_e, which makes typical separation of the nuclear energy levels $\Delta\mathrm{E}_{nuc.}$ smaller than the typical separation among electronic levels $\Delta\mathrm{E}_{elec.}$. Hence, the time scale of the nuclear motion $\tau_{nuc.} = \hbar/\Delta\mathrm{E}_{nuc.}$ is of the order of $\sim 10^{-12}$ s, while for the electronic motion $\tau_{elec.} = \hbar/\Delta\mathrm{E}_{elec.} \sim 10^{-15}$ s. This fact allows to approximate the nuclei as fixed when treating the electronic problem, which is known as the *Born-Oppenheimer* approximation. Now, given a set of $\{\boldsymbol{R_i}\}$, the kinetic energy of the nuclei is identically zero and the interaction between the nuclei gives a constant energy that can be omitted. The electronic Hamiltonian reads:

$$\hat{H}_{el} = \hat{T} + \hat{V}_{ext} + \hat{V}_{e^-e^-} \tag{3.20}$$

where,

$$\hat{T} = -\frac{1}{2}\sum_{i}^{N}\nabla^2_{\boldsymbol{r_i}} \tag{3.21}$$

$$\hat{V}_{ext} = -\sum_{i,j}^{M,N}\frac{Z_i}{|\{\boldsymbol{R}_i\} - \boldsymbol{r_j}|} \tag{3.22}$$

$$\hat{V}_{e^-e^-} = \frac{1}{2}\sum_{\substack{i,j\\ j\neq i}}^{N}\frac{1}{|\boldsymbol{r}_i - \boldsymbol{r}_j|} \tag{3.23}$$

Then, the N electrons can be thought of as moving in a constant external potential $\hat{V}_{ext}$ provided by the nucleii, while also interacting with each other.

Although this problem is much simpler than the one defined by equation 3.19, the many-body term $\hat{V}_{e^--e^-}$ is still a challenge. In 1964, in a seminal paper considered the start of the Density Functional Theory (DFT), P. Hohenberg and W. Kohn [13] formulated the DFT as an exact theory for treating many-body systems. They showed that all the ground state properties of an interacting many-body system could be uniquely defined by its electronic density $n(\boldsymbol{r})$. The challenge offered by the DFT approach is how to reformulate the many-body theory in terms of functionals.

One year later, Kohn and L. J. Sham proposed an *ansatz* [14]: there is an auxiliary system of N single-electron wave functions $\phi(\boldsymbol{r_i})$ which yield the same electronic density $\mathrm{n}(\boldsymbol{r}) = \sum_i^N |\phi(\boldsymbol{r_i})|^2$ of the original many-body system described by $\psi(\boldsymbol{r_1}, \boldsymbol{r_2}, ..., \boldsymbol{r_N})$. In the Kohn-Sham approach, the electronic energy of the system is written as

$$E_{KS} = T_0[(\boldsymbol{r})] + \int d\boldsymbol{r}\, V_{ext}(\boldsymbol{r})\, n(\boldsymbol{r}) + E_{Hartree}[n] + E_{xc}[n]. \tag{3.24}$$

In equation 3.24, T_0 is the kinetic energy of a non-interacting electron gas, V_{ext} is the functional for the external potential due to the nuclei (or any other sources, such as an electric field), $E_{Hartree}$ is the long-range electron-electron interaction term, known as the Hartree term, given by

$$\hat{E}_{Hartree} = \frac{1}{2} \int d\boldsymbol{r}\, d\boldsymbol{r'}\, \frac{n(\boldsymbol{r}) n(\boldsymbol{r'})}{|\boldsymbol{r} - \boldsymbol{r'}|}. \tag{3.25}$$

All the many-body effects are grouped into the exchange-correlation energy E_{xc}. In simple words, E_{xc} is just the difference between the kinetic and interaction energies of the true interacting system from those of the independent-particle system where electron-electron interactions are given by the long-range Hartree interaction. The conveniences of the KS approach is that, by separating the independent-particle kinetic energy and the Hartree term, E_{xc} can be expressed as a functional of the electron density

$$E_{xc}[n] = \int d\boldsymbol{r}\, n(\boldsymbol{r})\, \epsilon_{xc}([n], \boldsymbol{r}), \tag{3.26}$$

where $\epsilon_{xc}(n, \boldsymbol{r})$ is an energy per electron at point $\boldsymbol{r}$ that depends on the electronic density n at the point $\boldsymbol{r}$ and possibly its neighborhood $\boldsymbol{r} + \delta\, \boldsymbol{r}$.

The single-particle orbitals $\phi(\boldsymbol{r_i})$ obey the Kohn-Sham (KS) equation

$$\hat{H}_{KS} \left|\phi_i\right\rangle = (\hat{T}_0 + \hat{V}_{ext} + \hat{V}_{Hartree} + \hat{V}_{xc}) \left|\phi_i\right\rangle = \epsilon_i \left|\phi_i\right\rangle, \tag{3.27}$$

in which $\hat{T}_0$ is the single-particle kinetic energy, $\hat{V}_{ext}$ is the external potential, $\hat{V}_{Hartree}$ is the long range Hartree interaction and $\hat{V}_{xc}$ is the functional derivative of E_{xc},

$$\hat{V}_{xc} = \epsilon_{xc}([n], \boldsymbol{r}) + n(\boldsymbol{r}) \frac{\delta \epsilon_{xc}([n], \boldsymbol{r})}{\delta n(\boldsymbol{r})}. \tag{3.28}$$

Already in their famous paper [14] Kohn and Sham noticed that the solid can be approximated as a homogeneous electron gas (HEG). This consideration leads to the Local Density Approximation (LDA, or LSDA if spins are included), in which $\epsilon_{xc}([n], \boldsymbol{r})$ is assumed to be the same of a HEG with the density of the real system. Improvements of the L(S)DA include the Generalized Gradient Approximation (GGA), which also includes the first derivatives of the electronic density $\nabla n(\boldsymbol{r})$ into $\epsilon_{xc}([n], \boldsymbol{r})$. There are also functionals which aim at specific properties or types of materials, for example the modified Becke-Jonhson (mBJ) exchange correlation potential, which focuses on accurately calculating band gaps [72] and the LDA+U potential, used to derive properties of strongly correlated systems [73; 74].

Since the main interest lies in finding $n(\boldsymbol{r})$, which in turn is needed to build $\hat{V}_{xc}$, the KS equations must be resolved in a self-consistent fashion: an initial tentative $n^0(\boldsymbol{r})$ is given, defining an initial $\hat{V}^0_{xc}$ which is used to solve the KS equations, providing a new $n^1(\boldsymbol{r})$, then defining a new $\hat{V}^1_{xc}$. The method is iterative, and the process is repeated until a certain convergence criterion (usually the total energy of the system) is matched. The result is the electronic density $n^{GS}(\boldsymbol{r})$, which is believed to represent the ground state of the system. Then, it is possible to extract useful information of the system such as the total and ion-projected magnetic moment and density of states, the band structure, the dielectric function, and so on. However, it is important to note that the $\phi(\vec{r_i})$ wave functions and the ϵ_i eigenvalues are mathematical abstractions, having no rigorous physical meaning. There is one exception, though, which is the eigenvalue ϵ_{last} correspondent to the last occupied state. Then, ϵ_{last} is identified as $-I$, the negative of the ionization energy, *i.e.*, the energy required to unbind this electron from the system, which is known as the Koopmans' theorem [71].

3.2.2 WIEN2k

The band structure calculations were performed with the package WIEN2k [75; 76], which relies on a sophisticated version of the Augmented Plane Wave (APW) method to solve the Kohn-Sham equations. The APW method was in fact proposed by J. C. Slater in 1937 [77], before the development of the DFT, and relies on dividing the unit cell in non-overlapping atomic spheres centered at the nucleii (also known as the muffin-tin sphere) (A) and the interstitial region (B), filling the volume among the spheres, as depicted on Fig. 3.9.

Inside the atomic spheres, the wave functions $\phi_{\boldsymbol{k},\boldsymbol{K}}(\boldsymbol{r}, E)$ are expanded in radial solutions of the Schrödinger equation $u_\ell(r, E)$ at energy E, and spherical harmonics $\mathrm{Y}^\ell_m(\hat{\boldsymbol{r}})$, while

in the interstitial region they are expanded in plane waves $e^{i(\boldsymbol{k}+\boldsymbol{K})\cdot\boldsymbol{r}}$, as shown in equation 3.29:

$$\phi_{\boldsymbol{k},\boldsymbol{K}}(\boldsymbol{r},E) = \begin{cases} \sum_{\ell,m} C_{\ell,m}^{\boldsymbol{k},\boldsymbol{K}} u_\ell(r,E) Y_m^\ell(\hat{\boldsymbol{r}}) & \boldsymbol{r} \in A \\ \frac{1}{\sqrt{V}} e^{i(\boldsymbol{k}+\boldsymbol{K})\cdot\boldsymbol{r}} & \boldsymbol{r} \in B \end{cases} \tag{3.29}$$

where V is the volume of the unit cell, $\boldsymbol{K}$ is a reciprocal lattice vector a $\boldsymbol{k}$ is a point in the reciprocal lattice and $C_{\ell,m}^{\boldsymbol{k},\boldsymbol{K}}$ is an unknown coefficient. There is also the requirement that the plane wave outside the sphere matches the function inside the sphere over its entire surface. In WIEN2k, the spherical harmonics are expanded until $\ell = 10$ and number of plane waves is set by the parameter $R_{min} \times K_{max}$, in which R_{min} is the smallest muffin-tin sphere in the unit cell and K_{max} is the modulus of the highest $\boldsymbol{k}$ vector used. This parameter is set by the user, and although several values should be tested for convergence, the WIEN2k package provides a few reference values, for instance, $R_{min} \times K_{max} = 6.5$ for $R_{min} = R_{oxygen}$.

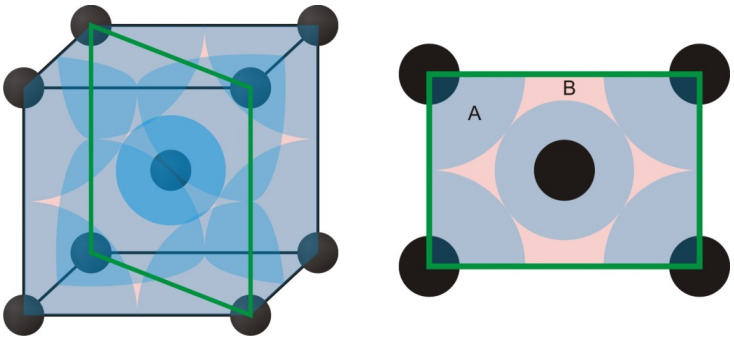

Figure 3.9 Representation of the Augmented Plane Wave (APW) method: division of the unit cell in non-overlapping atomic spheres centered at the nuclei (A) and the interstitial region (B).

The APW method has the advantage of describing electronic wave functions both near the nucleus and in the interstitial region. However, its basis functions are energy-dependent, which leads to a complicated non-linear eigenvalue problem. A way of getting around this issue is to introduce the energy derivative of $u_\ell(r,E)$ in the basis, which leads to a linear eigenvalue problem. The basis can be further enhanced with the addition of local orbitals (lo), used to describe valence d- and f-states and states in atoms that have a muffin-tin sphere much smaller than other spheres in the unit cell [71]. Indeed, the basis set implemented in the WIEN2k package is the (L)APW+lo.

The Hamiltonian of the spin-orbit interaction is given by equation 3.30 (in atomic units),

$$\hat{H}_{\mathrm{SO}} = \frac{1}{r}\frac{dU(r)}{dr}\hat{\boldsymbol{L}}\cdot\hat{\boldsymbol{S}} \tag{3.30}$$

where U(r) is a nuclear spherical potential presented to the electron, $\hat{\boldsymbol{L}}$ and $\hat{\boldsymbol{S}}$ are the orbital and spin angular momenta, respectively. This term was neglected in the previous discussion, although it may be important for the band structures and other properties of materials containing heavier elements, as well as for the description of some properties which couple lattice and spin degrees of freedom, *e.g.* the magneto-crystalline anisotropy of lighter materials. The spin-orbit term couples spin up and down wave functions, which means that the computational demand to this calculation can be considerably higher (roughly eight times) than the case without the SO term. However, it is recognized that the spin-orbit is generally a small effect, which allows to diagonalize the SO Hamiltonian in the space of the KS orbitals forming the low-energy bands and can greatly reduce the computational demand. First, the usual KS orbitals are obtained by diagonalizing (the spin dependent version of) equation 3.27, as if spin-orbit were not to be included. Second, a second variational eigenvalue equation is set up, using, as basis functions, the lowest KS orbitals (for both spins) as calculated in the previous step, what is known as the *second variational method* [78].

The input for the DFT calculations of Sr_2YRuO_6 and $Sr_2YRu_{0.75}Ir_{0.25}O_6$ is simply the crystal structure of the compounds and a few parameters of the calculation, which will be described in Section 5. The magnetic moments $m_i(\boldsymbol{r})$ are obtained by integrating the difference between majority and minority spin-projected electronic density $n^{\uparrow}(\boldsymbol{r})$ - $n^{\downarrow}(\boldsymbol{r})$ over the i-th atomic sphere. In turn, the density of states per energy and per unit cell is obtained by [71]:

$$\rho(E) = \frac{V_{uc}}{(2\pi)^3} \int_{BZ} \delta(\varepsilon_{i,\boldsymbol{k}} - E)\, d\boldsymbol{k} \tag{3.31}$$

where V_{uc} is the volume of the unit cell and $\varepsilon_{i,\boldsymbol{k}}$ is the energy of i-th orbital ϕ_i for a given $\boldsymbol{k}$ inside the Brillouin Zone (BZ).

3.3 Comparison to Experimental Data

The X-ray spectroscopic techniques of Chapter 2 can be viewed as methods to map the electronic structure of materials by studying their response to the creation of the hole after absorbing the incident photon. The correct interpretation of the experimental data starts with the choice of the proper method, which in turn requires knowledge of *what* is actually being measured. In non-interacting systems, described by single-particle wave functions, the responses are associated with occupied (XPS) or unoccupied parts (XAS) of the density of states. In other words, the detected signals will reflect the ground state energies and occupations. However, in the presence of interactions, the system can react

in many different ways, giving rise to many-body effects in the spectrum. These can be manifested as charge transfer effects, given by Δ and U, or multiplet effects, given by J and $10Dq$, in the cluster model scheme [20; 47].

In XPS measurements of TMO's, the most relevant many-body effects are of the charge transfer type, *i.e.*, charge fluctuations to neutralize the core or valence hole hole, which causes a distinction between *well-screened* and *poorly-screened* states. In turn, multiplet effects can usually be regarded as small energy corrections. This approximation, however, may not be true for (4,5)d^n systems with $4 \leq n \leq 6$. These present the most energetic multiplet corrections due to the possibility of achieving maximum intratomic spin magnetic moment and maximum filling of the low-lying t_{2g} orbital. In these systems, multiplet corrections may approach the order of Δ and U - this is precisely the case of the $4d^4$ Ru^{4+} ion in $SrTi_{0.5}Ru_{0.5}O_3$.

In XAS measurements, the photoexcited electron does not leave the system. Instead, it actually participates in most of the screening of the core hole potential, thus suppressing further screening by the charge transfer effect. As a result, the final states of the XAS technique and the spectral shape are mainly determined by multiplet effects. If the absorbing electron is from a $1s$ core electron, the technique is simplified. In this case, the $1s$ and the valence electron system (VES) wave functions can be treated as single-particles, and the $1s$ XAS spectrum simply corresponds to the unoccupied DOS, projected in p symmetry states due to the selection rules mentioned in Section 2.1.

In the following Chapter, the results for $SrTi_{1-x}Ru_xO_3$ (x = 0, 0.1, 0.2, 0.35, 0.40, 0.50, 0.60, 0.80 and 1), and for $Sr_2YRu_{1-x}Ir_xO_6$ (x = 0, 0.25), will be presented. The (Double) cluster model was chosen to interpret the spectra of the $SrTi_{1-x}Ru_xO_3$ series based on previous work [35] on $SrRuO_3$, which used the Cluster Model to study correlation and covalence effects in this material. Now, the interest lies in identifying possible changes in the electronic structure of $SrTi_{0.5}Ru_{0.5}O_3$ arising from the interaction between the TiO_6 and RuO_6 octahedra. On the other hand, the method chosen to study the $Sr_2YRu_{0.75}Ir_{0.25}O_6$ series was the DFT for mainly two reasons: (i) the primary interest lies in ground state properties such as the magnetic moments of Ru and Ir atoms, which are correctly calculated by the DFT; (ii) the Ru^{5+} ion assumes a $4d^3$ electronic configuration in this material, which leads to smaller electronic correlation and enables a better comparison of XPS data with the calculated DOS.

4 $SrTi_{1-x}Ru_xO_3$ Series

Contents

This Section presents a brief review on the $SrTi_{1-x}Ru_xO_3$ series, its physical properties and electronic structure, as well as the preparation and characterization of the samples used in this work. Then, the X-ray spectroscopic results of these samples will be presented, and finally the detailed results for $SrTi_{0.5}Ru_{0.5}O_3$, which were interpreted with (Double) Cluster model calculations. The goal of this part of the work is to identify occasional changes in the electronic structure of $SrTi_{1-x}Ru_xO_3$ with the substitution of Ti for Ru. There is particular interest on the composition of the final states on each of the spectroscopic technique used, which makes the cluster model more suitable than the DFT calculations. Further, since our previous study on $SrRuO_3$ used the cluster model, this study is a somewhat straightforward sequence of the former. This part of the work is being prepared for submission.

4.1 Introduction

4.1.1 Physical properties

The $SrTi_{1-x}Ru_xO_3$ series mixes two very different compounds. On the $x = 0.0$ side, $SrTiO_3$ is a cubic perovskite at room temperature, which exhibits a tetragonal phase between 110 K and 65 K, orthorhombic between 55 K e 35 K and possibly rhomboedric below 10 K [79]. This material is also a diamagnetic band insulator, with direct band gap close to 3.7 eV [80]. On the $x = 1.0$ side, $SrRuO_3$ crystallizes in an orhtorhombic distorted perovskite structure at room temperature. The electrical resistivity ρ of $SrRuO_3$ exhibits metallic dependence with temperature T ($d\rho/dT < 0$) [81], behaves as a Fermi Liquid at low temperatures [82], and as a bad metal at high temperatures [83; 84]. Additionally, this material presents itinerant ferromagnetism with a Curie temperature $T_C \approx 160$ K and magnetic moment of 1.66 $\mu_B/f.u.$ [24]. Until now, $SrRuO_3$ is the only known material among the 4*d* TM oxides to present metallic behavior and ferromagnetism in the same phase.

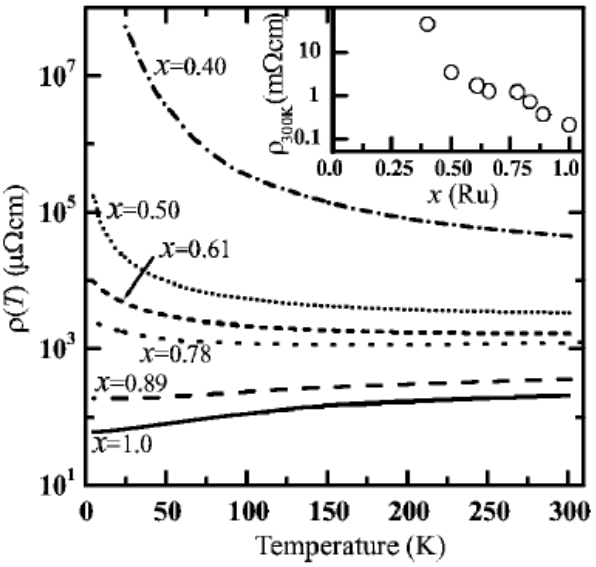

Figure 4.1 Temperature dependent electrical resistivity measurements of $SrTi_{1-x}Ru_xO_3$ series for $0.4 < x < 1.0$. The inset shows the electrical resistivity at room temperature. Extracted from [36].

The combination of $SrTiO_3$ and $SrRuO_3$ gives rise to a series marked by three different crystallographic phases and intriguing electric properties. This series accommodates a cubic perovskite structure for $0.0 < x < 0.30$, tetragonal for $0.30 < x < 0.40$ and orthorhombic for x > 0.40. Regarding its electrical resistivity, Fig. 4.1 presents ρ(T) for various values of x, extracted from [36]. In this study, the authors propose a complex

evolution of the electrical behavior across the series. For $x \approx 0.0$ the compound is insulating for all temperatures studied. Ruthenium substitution leads to a disordered correlated insulating state for x $\approx$ 0.2, a soft Coulomb gap state for $x \approx 0.4$ and an Anderson insulating state for $x \approx 0.5$. Further substitution causes an insulator-to-metal transition at $x \approx 0.75$ (which can be seen in the change of slope of ρ(T) between $x = 0.61$ and 0.78 in Fig. 4.1 and in ρ(300), the inset), turning the compound into a disordered metal and then into a correlated metal for $x \approx 1.0$ [36].

4.1.2 Electronic structure

In the ionic limit, the divalent Sr^{2+} and tetravalent Ti^{4+} ions would present empty $4d$ and $3d$ bands, respectively, whereas the also tetravalent Ru^{4+} ions would show a low-spin $4d^4$ electronic configuration.

Valence band X-ray photoemission spectroscopy measurements of $SrTiO_3$ polycrystals revealed no sign of spectral weight up to 3.2 eV, which confirms the insulating character of the compound. The valence band sets in at approximately 3 eV and extends until around 9.0 eV, as shown in Fig. 4.2 a), extracted from [85]. The conduction band of $SrTiO_3$ and other titanium compounds were studied with O $1s$ X-ray Absorption Spectroscopy [86], and is underlined in Fig. 4.2 b).

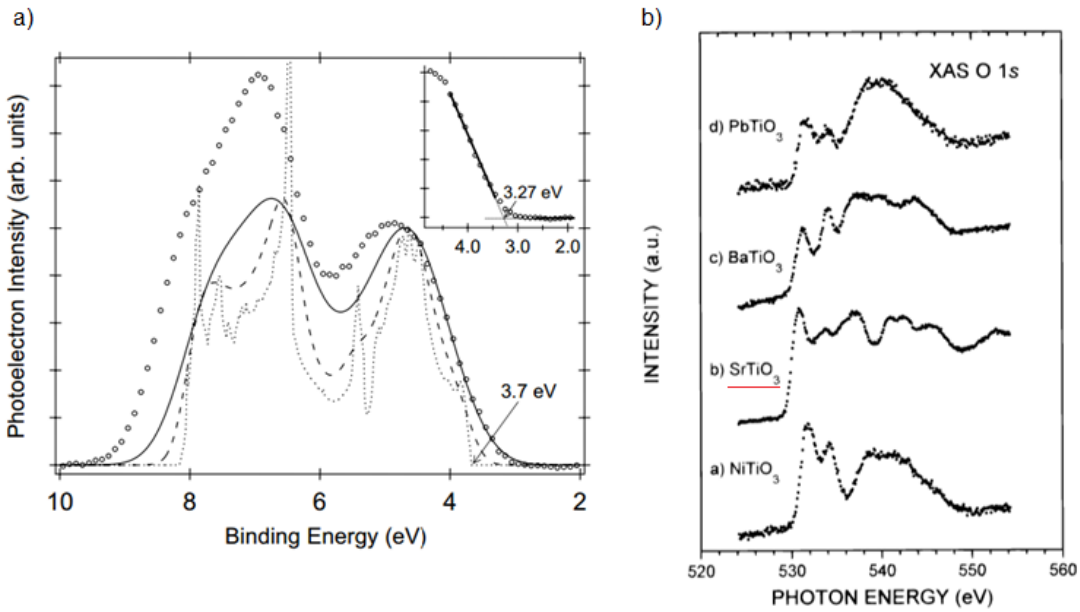

Figure 4.2 a) Valence band X-ray photoemission and b) O $1s$ X-ray absorption spectra of titanium compounds, including $SrTiO_3$, highlighted in the picture. Extracted from [85] and [86], respectively.

On the other end of the series, $SrRuO_3$ presents a more intricate electronic structure, which has been subject of several studies with different experimental techniques, for instance X-ray photoemission spectroscopy [87–89] and X-ray O 1*s* absorption spectroscopy [89–91], as well as theoretical methods such as DFT [92–95], cluster model calculations [96] and Dynamical Mean Field theory (DMFT) [97].

The results provided different conclusions regarding the relative influence of electronic correlation and O 2*p* - Ru 4*d* covalence in the electronic structure of $SrRuO_3$. Recently, our group conducted a study on $SrRuO_3$ thin films which included several spectroscopic techniques and Cluster model calculations [35]. It was shown that $SrRuO_3$ is in the Negative Charge Transfer regime, presenting a ground state dominated by configurations with holes in the O 2*p* bands ($d^5\underline{L}C$). This fact is also seen in the valence band photoemission spectrum which, according to the Cluster model results, presents significant contribution of O 2*p* screening (configurations with $d^5\underline{L}^2$) close to the Fermi level. However, this region also presents strong contribution from coherent screening (configurations with $d^5\underline{L}C$), characteristic of correlated metals. Additionally, satellite peaks in the bottom of the valence band, interpreted in the Cluster model as unscreened states ($d^4\underline{L}$), may also be attributed to electron correlation. The above characteristics of the electronic structure of $SrRuO_3$ mark the high degree of O 2*p* - Ru 4*d* covalence, as well as the importance of correlation effects in the core level and valence band photoemission spectra. Hence, both effects should be taken into account in the description of the physical properties and electronic structure of $SrRuO_3$ [35], and possibly in related compounds such as the $SrTi_{1-x}Ru_xO_3$ series.

Regarding the $SrTi_{1-x}Ru_xO_3$ series, valence band ultraviolet photoemission and O 1*s* X-ray absorption measurements were performed by M. Abbate *et al.* [98], which argued that the Ti 3*d* and Ru 4*d* bands are apart by 1.8 eV in this series, preventing fluctuations between the Ti^{4+} and Ru^{4+} sites. It was then suggested that the ES of the $SrTi_{1-x}Ru_xO_3$ series could be understood as a proper linear combination of the ES of the end members, *i.e.*, $SrTiO_3$ and $SrRuO_3$, as shown in Fig. 4.3

In the proposed scenario, the mechanism behind the insulator-to-metal transition would be of the *percolation* kind. Starting from an insulating $SrTiO_3$ matrix, the substitution of Ti by Ru (increasing x) would induce the formation of small $SrRuO_3$ clusters, which are conductive. Below a certain threshold x_C, the low connectivity among these patches prevents the metallic states from extending throughout the sample, resulting in a macroscopic insulating behavior. Above x_C, there is enough connectivity to form a path in which electrons can be transported across the sample. This situation is depicted in Fig. 4.4, where the black (white) squares denote insulating (metallic) patches, and the squares

highlighted in blue represent the path for the electronic transport.

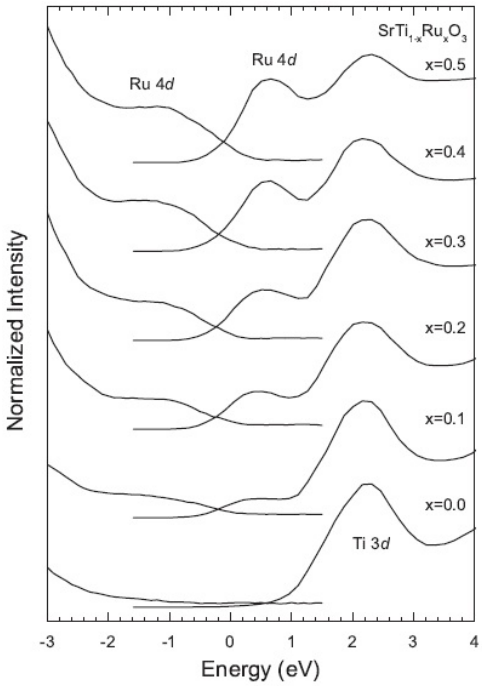

Figure 4.3 Photoemission and O 1*s* X-ray Absorption Spectra of $SrTi_{1x}Ru_xO_3$ as a function of the Ru concentration x, extracted from [98].

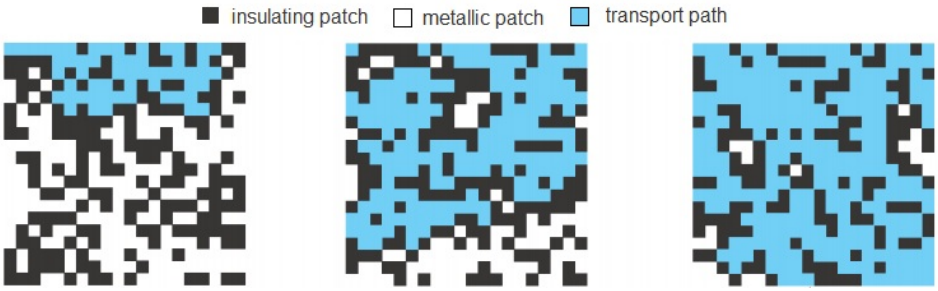

Figure 4.4 Representation of the mechanism behind the insulator-to-metal transition of the percolation kind. Starting from an insulating matrix (white squares), the substitution of metallic patches (increasing x) would induce the formation of a conduction path (blue squares). Below a certain threshold x_C, the low connectivity among results in a macroscopic insulating behavior. Above x_C, there is enough connectivity to form a path in which electrons can be transported across the sample.

Kim *et al.* [99] reported on X-ray core level photoemission spectra of the $SrTi_{1-x}Ru_xO_3$ series, and found no sign of different Ti and Ru ions other than the nominal Ti^{4+} and Ru^{4+}. Such study also reports on X-ray valence band photoemission and X-ray absorption measurements, which present good agreement with the spectra reported by M. Abbate *et al.* [98], although the authors have interpreted the results differently. They suggested that the insulator-metal transition in the $SrTi_{1-x}Ru_xO_3$ would be caused

by the combined effects of correlation (in the sense of a Mott-insulator) and disorder (which is detrimental to the formation of delocalized states throughout the sample). However, electrical resistivity $\rho(T)$ and X-ray photoemission measurements on thin films of Sr_2TiRuO_6 with various degrees of disorder, *i.e.* the arrangement of TiO_6 and RuO_6 octahedra, showed that more ordered samples (towards three-dimensional checkerboard arrangement) present higher electrical resistivity and lower spectral weight at the Fermi level [37] than disordered samples (with randomly distributed TiO_6 and RuO_6 octahedra). This suggests that the electronic properties of Sr_2TiRuO_6 are strongly influenced by the $4d$ state connectivity among neighboring Ru atoms. Fig. 4.5 summarizes these results.

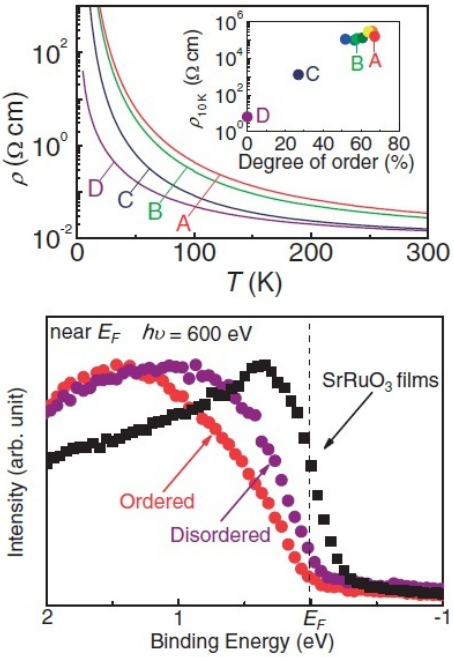

Figure 4.5 Electrical resistivity and X-ray photoemission measurements on thin films of Sr_2TiRuO_6 with various degrees of disorder. Extracted from [37].

A theoretical study by Maiti [100], based on the DFT method with the LDA approach, explored the possibility of emerging half-metallicity in Ti substituted $SrRuO_3$ due to the narrowing of the Ru d band, which in turn would be cause by reduced Ru $4d$ – Ru $4d$ interactions. On the other hand, Lin *et al.* [101], using both GGa and GGA+U (in which a local U term was added to the Ru $4d$ orbitals) approaches. Their study showed that the driving mechanism behind the insulator-metal transition in $SrTi_{1-x}Ru_xO_3$ is the electron correlation, and that Ti substitution alters Ru $4d$ orbital ordering.

4.1.3 Sample preparation and characterization

Polycrystalline samples of $SrTi_{1-x}Ru_xO_3$ (x = 0, 0.10, 0.20, 0.30, 0.33, 0.35, 0.40, 0.50, 0.60, 0.80 and 1) were synthesized by the solid state reaction method by the group of Prof. Renato Jardim, from University of São Paulo - SP. X-ray diffraction (DRX) patterns (not shown) were obtained using a Bruker D8 Discover diffractometer (Cu K_α radiation, $\lambda = 1.5418$ Å). The Rietveld analysis, performed with the GSAS/EXPGUI package [102; 103], was used to obtain the lattice parameters and identify the crystallographic phases, and no sign of spurious phases were found. Electrical resistivity measurements were performed in a Physical Properties Measurement System from Quantum Design in the temperature range between 5 and 300 K. The results for the x = 0, 0.30, 0.33, 0.35, 0.40, 0.50, 0.60, 0.80 and 1 samples are displayed in Fig. 4.6. The behavior of the ρ *vs.* T curve is clearly insulating ($d\rho/dT < 0$) for the $x = 0.3$ sample, and evolves to a metallic behavior ($d\rho/dT > 0$) for the $x = 1$ sample. More precisely, the samples with $x \leq 0.60$ present insulating behavior, while the $x = 0.8$ sample presents an insulator-to-metal transition for $T \approx 70K$ (not shown) and the $x = 1$ sample is metallic in the entire measured temperature range. The insulator-to-metal transition in the $SrTi_{1-x}Ru_xO_3$ series happens in the $0.7 \leq x \leq 0.8$ range, which agrees with results from Kim *et al.* [36] reproduced in Fig. 4.1.

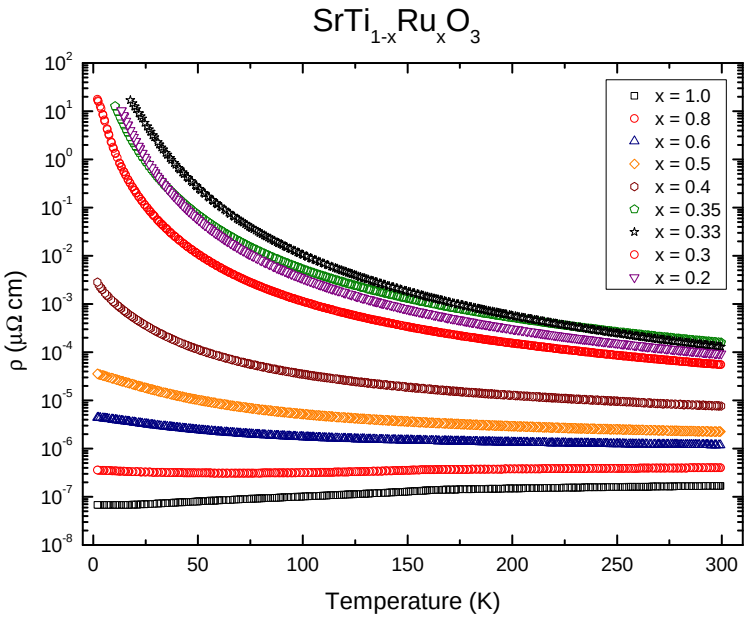

Figure 4.6 Temperature dependent electrical resistivity measurements of $SrTi_{1-x}Ru_xO_3$ samples with $0.4 < x < 1$, used in the X-ray spectroscopy measurements presented in this thesis.

4.2 Results

4.2.1 X-ray spectroscopy of $SrTi_{1-x}Ru_xO_3$ series

This section presents the X-ray core level and valence band photoemission and X-ray absorption spectra of the $SrTi_{1-x}Ru_xO_3$ samples (x = 0, 0.1, 0.2, 0.35, 0.40, 0.50, 0.60, 0.80 and 1.0). The following spectra will be described in a general way across the whole series. A more detailed view of the x = 0, 0.5 and 1 samples, and comparison with (Double) Cluster Model calculations, will be presented in the subsequent sections.

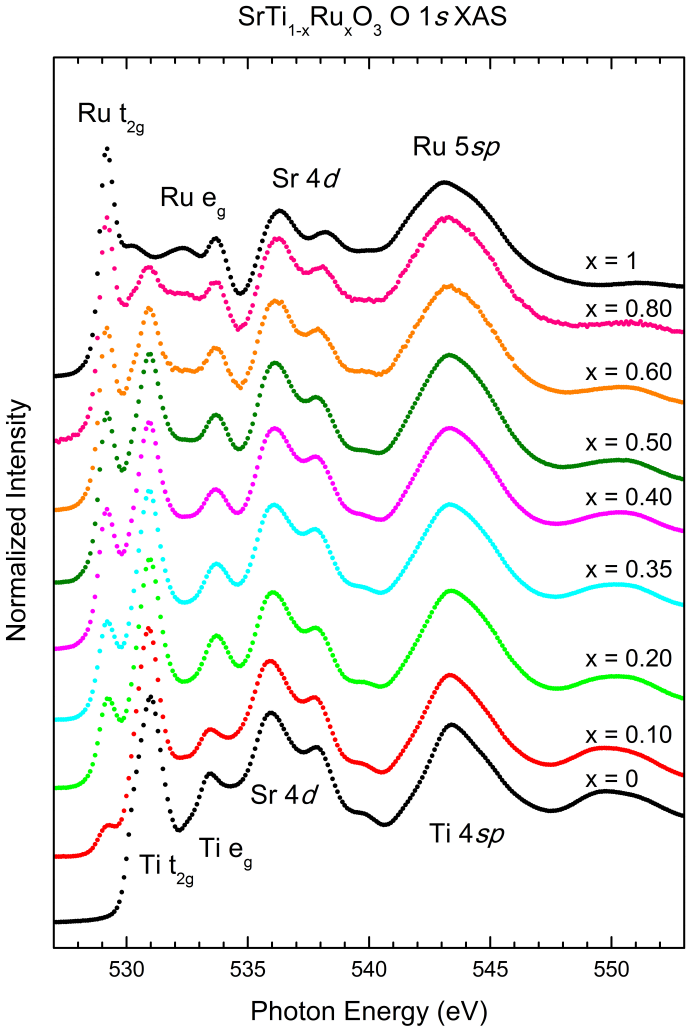

Figure 4.7 O 1s XAS spectra of the $SrTi_{1-x}Ru_xO_3$ series. The Sr 4d and Ti 4sp/Ru 5sp region is practically independent of x, while the the structures related to the Ru 4d (Ti 3d) band increase (decrease) smoothly with increasing x.

Figure 4.7 presents the O 1s XAS spectra of the $SrTi_{1-x}Ru_xO_3$ series. The spectra

are related to transitions from O 1s to empty O 2p states, which are covalently mixed with Ti and Ru bands (and also with Sr bands). Hence, transitions to these states provide information on the unoccupied TM bands.

The spectrum of $SrTiO_3$, in the bottom part of the Figure, Ti 3d-derived band is formed by two peaks assigned to 3d t_{2g} (531 eV) and 3d e_g (533.3 eV) sub-bands split by the crystal field; the Sr 4d states appear from 534 to 538 eV, while Ti 4sp states appear centered at 543 eV. Similarly, the XAS spectrum of $SrRuO_3$, in the top part of the Figure, presents the Ru 4d is also split into the t_{2g} (529 eV) and e_g (centered at 534 eV) sub-bands, while the latter is further split by the intra-atomic exchange interaction in two structures at 532.2 and 533.6 eV.

At intermediate x values, all the spectra present the structures seen in the end members' spectra. Since the Sr 4d and Ti 4sp/Ru 5sp bands fall in the same energy region, this part of the spectra remains practically unchanged across the series. On the other hand, the Ti 3d/Ru 4d region present visible changes. For $x = 0.1$, TM region exhibits the two Ti 3d t_{2g} and e_g peaks, while the Ru 4d t_{2g} states start to evolve at a lower energy and the Ru 4d e_g states are buried in the Ti e_g region. As x increases, the structures related to the Ru 4d (Ti 3d) band increase (decrease) smoothly. It is worth noting that, despite the structural phase transitions across the series, the local environment of the Ti^{4+} and Ru^{4+} ions, *i.e.* their respective TMO_6 octahedra, remain unaltered, which is why the Ti 3d and Ru 4d unoccupied states present the same shape. The above attributions agree with the literature [88; 104].

Fig. 4.8 presents the core level XPS measurements of the $SrTi_{1-x}Ru_xO_3$, measured with photons of 2840 eV. In the bottom, the spectrum for $x = 0$ presents two main features at 458 and 464 eV, related to the Ti $2p_{3/2}$ and Ti $2p_{1/2}$ features, split by the spin-orbit interactions. The structures at 472 and 478 eV are the correspondent satellites. In the top, the $x = 1$ spectrum also presents two components, which are broader and more separated than the ones from Ti 2p, originated by the spin-orbit interaction, Ru $3p_{3/2}$ at 464 eV and Ru $3p_{1/2}$ at 486 eV.

At the intermediate x values, the spectra present all the features from the series' end members. For x = 0.1, small Ru-derived features are found at 486 eV, while intense Ti derived features are observed at 458 and 486 eV. Please note that the Ru $3p_{3/2}$ and Ti $2p_{1/2}$ are superimposed around the 464 eV region. As x increases towards 1, the Ru-derived features increase smoothly, while the Ti-derived structures are gradually suppressed. In fact, the spectra of the different mixed compositions look like linear combinations of the end members' spectra. Again, since the local environment of the Ti^{4+} and Ru^{4+} ions remain unaltered, the Ti 2p and Ru 3p core states present the same shape.

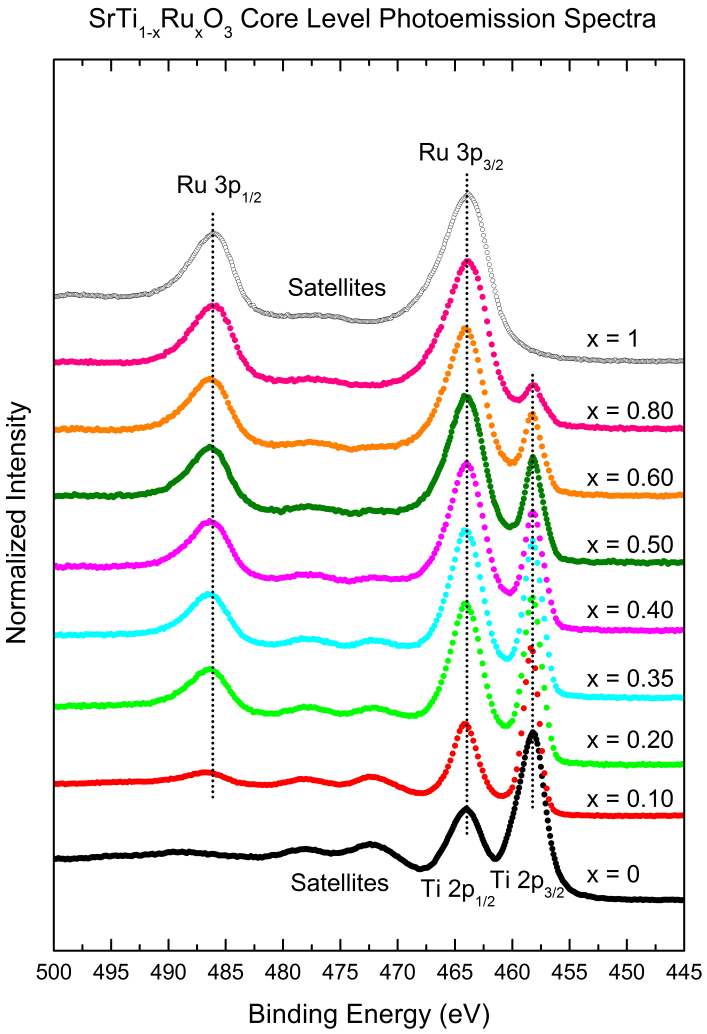

Figure 4.8 Core level XPS measurements of the $SrTi_{1-x}Ru_xO_3$. For $x = 0$, the spectrum features at 458 and 464 eV, related to the Ti $2p_{3/2}$ and Ti $2p_{1/2}$ components, and the correspondent satellites at 472 and 478 eV. As x increases towards 1, the Ru-derived features at 464 and 486 eV increase smoothly, while the Ti-derived structures are gradually suppressed.

Figure 4.9 presents the valence band XPS spectra of the $SrTi_{1-x}Ru_xO_3$ series, measured with photons of 2841 eV. The solid line at zero energy represents the Fermi level. The spectrum for x = 0, at the bottom of the Figure, shows no spectral weight until the onset of the O $2p$ band at around 2 eV, extending until 8 eV, in agreement with the band insulating behavior of $SrTiO_3$. In turn, the spectrum of $SrRuO_3$, at the top part of Fig. 4.9 presents two regions, a Ru $4d$-derived band from E_F to $\approx$ 4 eV, and the O $2p$ from 4 eV to 8 eV, also seen in the spectra presented on Figure 4.3.

All the intermediate compositions present a spectral shape very close to the one from $SrRuO_3$. For the incident photon energies $\hbar\omega \approx 2800$ eV used in the experiment, the

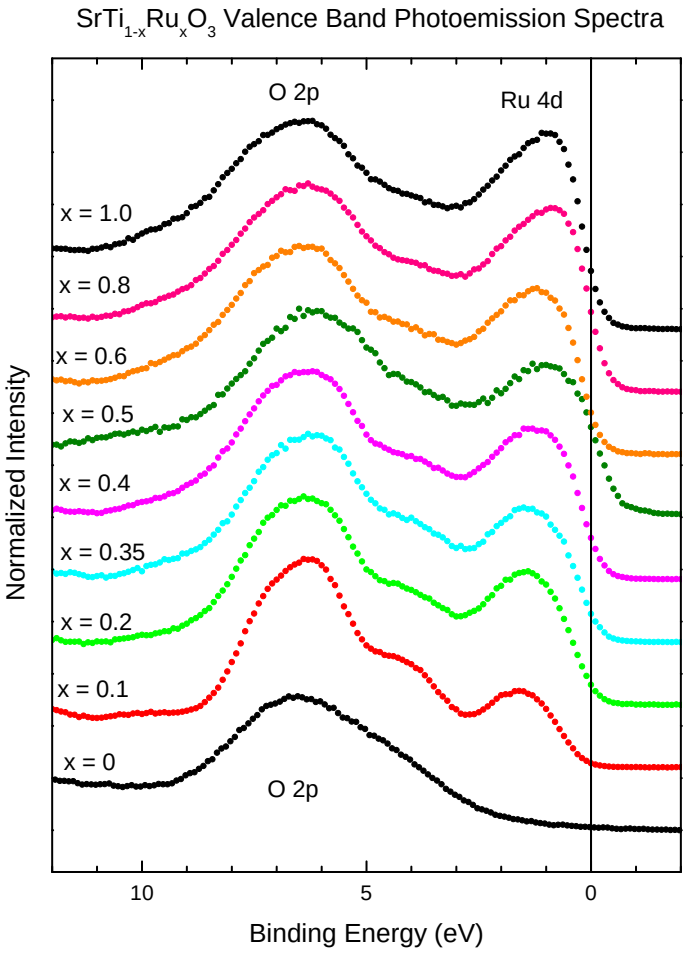

Figure 4.9 Valence band XPS spectra of the $SrTi_{1-x}Ru_xO_3$ series. The solid line at zero energy represents the Fermi level. For x = 0, no spectral weight is measured until the onset of the O 2*p* band around 2 eV, up to 8 eV. The spectrum for x = 1 presents two regions, a Ru 4*d*-derived band from E_F to ≈ 4 eV, and the O 2*p* from 4 eV to 8 eV.

photoionization cross section $\sigma_{Ti\ 3d}$ of Ti 3*d* electrons is at least an order of magnitude smaller than $\sigma_{Ru\ d}$, which explains the similarity. On the other hand, it is worth noting that the shape of the Ru 4*d* band is nearly unaffected throughout the series.

4.2.2 Details of the double cluster calculations

As seen in many examples throughout this thesis, single cluster model calculations have been extensively used to simulate and interpret spectroscopic measurements of transition metal compounds, such as in [35; 60; 65; 67] and others, but there are no reports of the extension of this method to two octahedra. Double cluster model calculations are much more computationally demanding, which can usually be performed using a com-

plete basis sets including elements from the ionic d^n up to the $d^{10}\underline{\mathrm{L}}^{10-n}$ configurations. To deal with this model, a program was developed in *MATLab*, in collaboration with a colleague, MSc. Henrique P. Martins. The program generates the basis; diagonalize the ground, core, removal and addition state matrices; and calculates the corresponding XPS and XAS spectra. Any ionic configuration, from d^0 to d^{10} can be given as input for each site. The program is currently developed to treat only the O_h symmetry, but it can be adapted to other symmetries.

Due to computational limitations, in all present calculations a maximum of 4 holes, ligand and coherent, were admitted. Disregarding identical matrices, which are identified by the program and are only diagonalized once, the present calculation required the diagonalization of one $\approx 7500 \times 7500$ matrix for the ground state; one $\approx 7500 \times 7500$ matrix for each core state (Ti $2p$ and Ru $3p$); two removal state $\approx 6000 \times 6000$ matrices, and two $\approx 5000 \times 5000$ addition state matrices for the Ti site; two $\approx 8000 \times 8000$ removal state matrices, and four $\approx 5000 \times 5000$ addition state matrices for the Ru site. For consistency, the same maximum number of ligand holes were used in the single cluster calculations. With this basis restriction, the ground state energy is correct up to the order of 10^{-2} eV.

4.2.3 Ground state

Table 4.1 presents the parameters used in the double cluster model calculations, which were chosen to give the best agreement with the X-ray spectroscopy measurements. The parameters found are in accordance with previous reported values [35; 69]. The reduced values of the hybridizations $\mathrm{T}\sigma_{Ti}$ and $T\sigma_{Ru}$ may partly be due to the reduced basis set, as seen in other calculations [69]. Additionally, small differences in the TiO_6 and RuO_6 octahedra may also affect $T\sigma_{Ti}$, $T\sigma_{Ru}$, 10 Dq_{Ti}, and 10 Dq_{Ru}.

Table 4.2 presents the calculated contributions of the main configurations to the ground state (GS) of $SrTi_{0.5}Ru_{0.5}O_3$. The configurations are displayed with $\mathrm{d}_{Ti}^{m+r}\underline{\mathrm{L}}^{p+r}\underline{\mathrm{C}}^{q}\mathrm{d}_{Ru}^{n+p+q}$ notation, as well as projected over each TM ion to facilitate comparison with the single cluster results. According to the calculations, most of the GS is dominated by $d^1\underline{\mathrm{L}}^2d^5$, $d^0\underline{\mathrm{L}}d^5$, $d^1\underline{\mathrm{L}}d^4$ and d^0d^4 configurations. The projected values onto each TM site yielded, for Ti^{4+}, 45% $d^1\underline{\mathrm{L}}$ + 27% d^0, and for Ru, 45% $d^5\underline{\mathrm{L}}$ + 26% d^4. These results are very close to those of single cluster calculations of $SrTiO_3$ and $SrRuO_3$ [35; 69]. Hence, the most relevant configurations to the GS of $SrTi_{0.5}Ru_{0.5}O_3$ can be understood as different arrangements of the $SrTiO_3$ and $SrRuO_3$ ground states.

According to the Δ_{Ti} and U_{Ti} parameters, the Ti^{4+} ion should fall close to the

Table 4.1: Parameters used in the double cluster model calculation for $SrTi_{0.5}Ru_{0.5}O_3$.

$SrTi_{0.5}Ru_{0.5}O_3$			
Ti		Ru	
Parameter	Value (eV)	Parameter	Value (eV)
U	4.2	U	5.0
Δ	4.5	Δ	1.4
T_σ	3.9	T_σ	1.7
$10Dq$	1.8	$10Dq$	4.4
J	0.20	J	0.75
$pp\sigma - pp\pi$	0.91	$pp\sigma - pp\pi$	0.91
Δ^*	-	Δ^*	0.6
T^*	-	T^*	0.25

frontier of the charge transfer and the intermediate regimes on the ZSA diagram [61]. However, the high value of the T_σ interaction favors the sharing of an O $2p$ electron, making $d^1\underline{L}$ the dominant configuration in the ground state of $SrTiO_3$. On the other hand, the Ru^{4+} ion in $SrRuO_3$ is known to be in a negative charge transfer regime (NCT) [61], because the lowest energy configuration in the ground state is $d^5\underline{L}$ and $\Delta_{Ru}^{eff} \equiv \Delta_{Ru} - \epsilon_{multiplets} < 0$, where $\epsilon_{multiplets}$ is the energy of the multiplet terms $10Dq_{Ru}$ and J_{Ru} [35].

In fact, the GS of $SrTi_{0.5}Ru_{0.5}O_3$ is dominated by the $d^1\underline{L}^2d^5$ (21.8%) state, which presents an electron transferred from the O $2p$ bands to both metal bands. This configuration is closely followed by the $d^0\underline{L}d^5$ (15.3%) and $d^1\underline{L}d^4$ (14.2%) configurations, while the ionic d^0d^4 configuration contributes with roughly 10%. Projection of these states onto each TM site agrees with the single cluster model calculations for $SrTiO_3$ and $SrRuO_3$. It is not a surprise that the GS of $SrTi_{0.5}Ru_{0.5}O_3$ also presents a highly mixed p–d character, yielding a mean occupancy in the metal d bands of around 5.8 electrons, 0.9 coming from the Ti site and 4.9 from the Ru site.

Table 4.2: Main contributions to the ground state wave function of $SrTi_{0.5}Ru_{0.5}O_3$, their projection onto each site, and the mean d orbital occupancy.

$SrTi_{0.5}Ru_{0.5}O_3$					
Ti:Ru		Ti site		Ru site	
Conf.	%	Conf.	%	Conf.	%
$d^1\underline{L}^2d^5$	21.75	$d^1\underline{L}$	45%	$d^5\underline{L}$	45%
$d^0\underline{L}d^5$	15.3	d^0	27%	d^4	26%
$d^1\underline{L}d^4$	14.22	$d^2\underline{L}^2$	23%	$d^5\underline{C}$	13%
d^0d^4	9.7	$d^3\underline{L}^3$	1.3%	$d^5\underline{LC}$	2.5%
$\langle n\rangle \approx 5.8$ elec.		$\langle n\rangle \approx 0.9$ elec.		$\langle n\rangle \approx 4.9$ elec.	

4.2.4 O 1*s* level absorption spectra

Figure 4.10 presents the O 1s absorption spectra of $SrTiO_3$ (top), $SrRuO_3$ (bottom), and $SrTi_{0.5}Ru_{0.5}O_3$ (middle). The spectra are related to transitions from O 1s to empty O 2p states. Since O 2p states are covalently mixed with Ti and Ru bands (and also with Sr bands), transitions to these states provide information on the unoccupied TM bands. The Ti 3d and Ru 4d-derived regions of the experimental spectra are compared to the O 2p character of the calculated addition $(N+1)$ spectrum. The top panel presents the spectrum of $SrTiO_3$. The Ti 3d region is composed of two peaks, at 531.0 and 533.5 eV, whereas the Sr 4d and Ti 4sp regions are located at around 537 and 543 eV, respectively. These results are in agreement with previously reported O 1s XAS spectra for $SrTiO_3$ [86]. The calculated addition spectrum, using the single cluster model, is represented by the solid black line, and is able to reproduce the positions of two Ti-derived structures in the spectrum.

The spectrum of $SrRuO_3$ is presented in the bottom panel. The Ru 4d region presents three peaks at 529.2, 532.2 and 533.6 eV, whereas the Sr 4d and Ru 5sp regions also appear at 537.0 and 543.0 eV, respectively. Again, the calculated spectrum, using the single cluster model and represented by the solid black line, is in good agreement with the experimental data and with previously reported results [35].

The O 1s XAS spectrum for $SrTi_{0.5}Ru_{0.5}O_3$ is presented in the middle panel. The spectrum resembles a linear combination of both $SrTiO_3$ and $SrRuO_3$ O 1s XAS spectra and presents the first Ru and Ti features at 529.2 eV and 531 eV, respectively, followed by a plateau at 532.3 eV and a peak at 533.6 eV. The Sr 4d and Ti 4sp/Ru 5sp states appear at the same energies, between 537.0 and 543.0 eV. The middle panel also presents the results for the double (black solid line) and the sum of the two single cluster model

calculations for $SrTiO_3$ and $SrRuO_3$ (gray dotted line). Both spectral shapes are similar and reproduce with good accuracy the intensities and energy positions of the features in the spectrum.

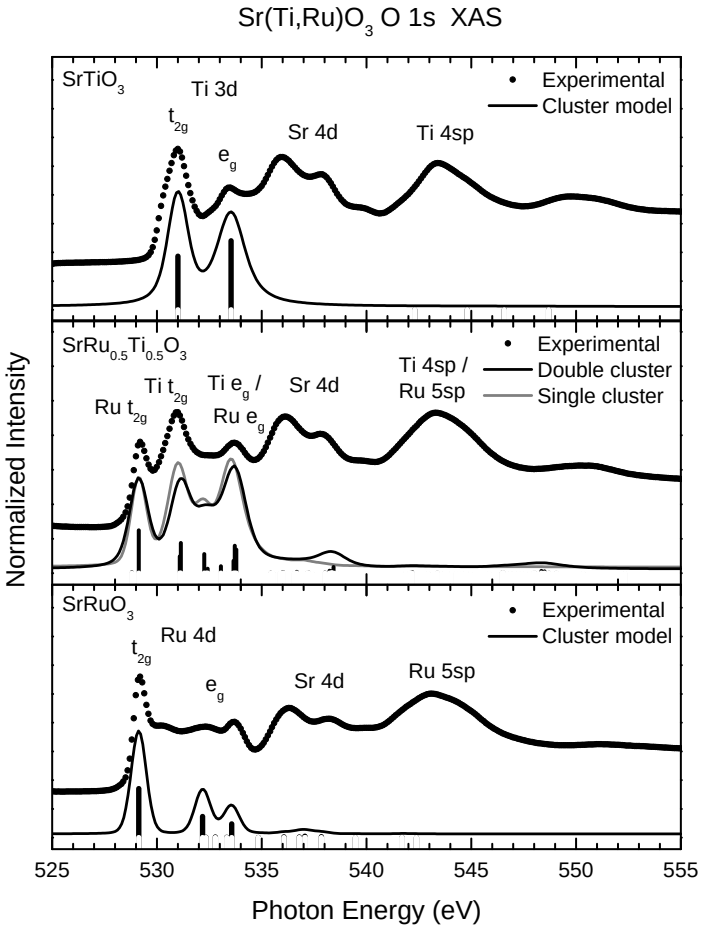

Figure 4.10 O 1*s* X-ray absorption spectra of $SrTiO_3$ (top), $SrTi_{0.5}Ru_{0.5}O_3$ (middle), and $SrRuO_3$ (bottom). The labels refer to the metal bands which are covalently mixed with the unoccupied O 2*p* states. The experimental results are compared to weighted single cluster and double cluster calculations.

In spite of the similarities, we can also analyze the composition of the different final states in the spectra in both cases. The top panel of Fig. 4.11 presents the decomposition of the calculated O 2*p* addition spectra for $SrTi_{0.5}Ru_{0.5}O_3$ with the double cluster model. The total spectral weight is split into Ti and Ru partial contributions, and the labels indicate the dominant configuration and the corresponding multiplet of each final state.

In the Ti part of the spectrum, shown in red, the two main peaks at 531.0 and 533.5 eV are due to the addition of an electron in the Ti 3*d* t_{2g} and Ti 3*d* e_g orbitals, respectively. The energy separation of the two peaks is around 2.5 eV, consistent with

the $10Dq_{Ti}$ value of 1.5 eV. In turn, the Ru component of the spectrum, shown in purple, presents three main peaks. The first peak at 529.2 eV is due to the addition of a minority Ru $4d$ t_{2g} electron. while the other two peaks are due to the addition of a majority (532.2 eV) and minority (533.6 eV) e_g electron, which is consistent with the splitting of $2J_{Ru} = 1.5$ eV. The separation of the t_{2g} peak and the center of the e_g peaks is also consistent with the value of $10Dq_{Ru} \approx 4.3$ eV. For comparison, the bottom panel of Fig. 4.11 presents the single cluster model calculation for $SrTiO_3$ and $SrRuO_3$. According to the labels, the Ti $3d$ features located at 531 and 533.5 eV correspond to transitions to $3d^1$ t_{2g} and $3d^1$ e_g states, respectively. The Ru $4d$ peaks at 529.2 eV correspond to transitions to minority $4d^5$ t_{2g} states. The other two peaks at 532.2 and 533.6 eV are due to majority and minority $4d^5$ e_g states, respectively.

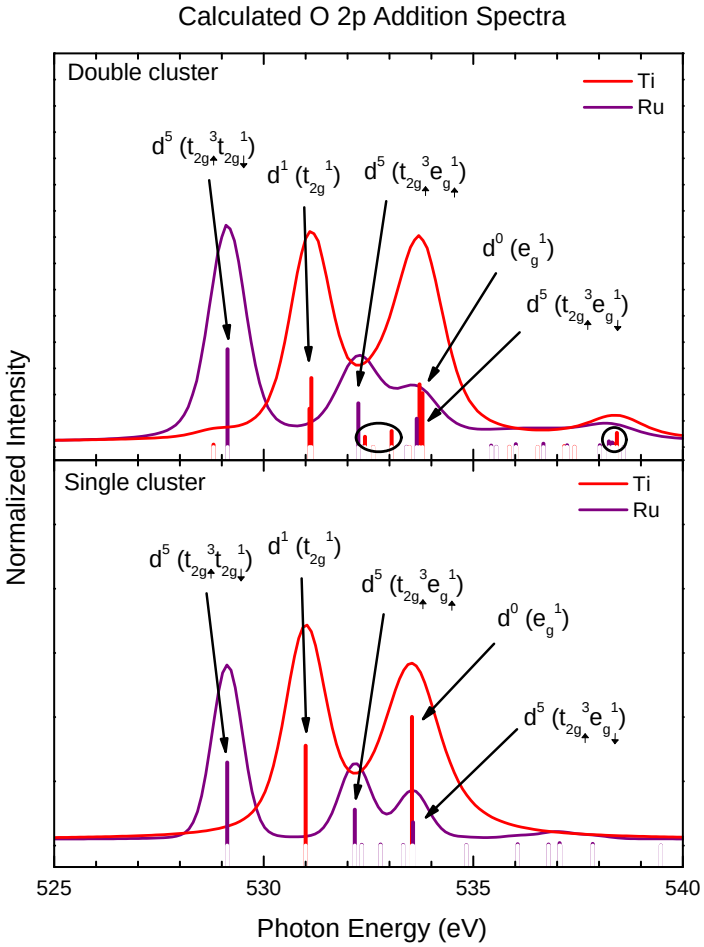

Figure 4.11 Calculated O $2p$ addition spectra with the double (top) and single (bottom) cluster. In the double cluster calculation, the spectra is projected into the Ru and Ti sites. The labels refer to the dominant configuration (multiplet) in the relevant discrete final states. The circles in the top panel point to new structures in the spectra when the Ti - Ru interaction is included.

It is clear that, in the case of O 1s XAS of $SrTi_{0.5}Ru_{0.5}O_3$, the spectrum resembles very closely, not only in shape, but also in the composition of the significant final states, to the sum of the spectra of the $SrTiO_3$ and $SrRuO_3$ samples. Nevertheless, it is worth noting that there are some small differences in the final states with Ti contribution at around 533 eV and in the intensity of satellites at about 539 eV, as highlighted in Fig. 4.11, even though they are not relevant for the XAS technique.

4.2.5 Ti 3p and Ru 4p core level spectra

Figure 4.12 presents the Ti 2p and Ru 3p core level photoemission spectra of $SrTiO_3$, $SrTiO_3$ and $SrTi_{0.5}Ru_{0.5}O_3$. The experimental spectra are compared with the corresponding calculated core level spectra. In the top panel, the experimental Ti 2p spectrum of $SrTiO_3$ presents the Ti $2p_{3/2}$ and Ti $2p_{1/2}$ peaks at 458.2 and 463.9 eV, split by the spin-orbit interaction. Each main peak is accompanied by a satellite at around 472.2 and 477.9 eV, in agreement with the spectrum reported by Bocquet *et al.* [69]. The core level spectrum calculated with the single cluster model is in good agreement with the experimental data, reproducing the energy position and relative intensities of all structures in the spectrum.

In the bottom panel, the Ru 3p spectrum of $SrRuO_3$ presents two broad structures at 463.9 eV and 486 eV, ascribed to the Ru $3p_{3/2}$ and Ru $3p_{1/2}$ components, respectively, along with a small bump centered at 477.0 eV. The calculated spectrum with the single cluster model is in good agreement with the experimental data, and is also able to reproduce the Ru 4p spectrum previously reported [35]. According to the calculation, the broad peaks are actually formed by various multiplets, as expected from a d^4 system. However, the bump around 477.0 eV was not reproduced by the model, although it could also be due to extrinsic effects [35].

The middle panel presents the Ti 2p and Ru 3p core level spectrum for $SrTi_{0.5}Ru_{0.5}O_3$, which shows features at the same energies as in the pristine compounds. The black line represents the calculated core level spectral weight with the double cluster model, while the gray line represents the linear combination of single cluster calculation for $SrTiO_3$ and $SrRuO_3$. Both calculated curves take into account the different photoionization cross sections of the Ti 2p and Ru 3p core levels [50], and present a good agreement with the experimental result.

It is clear that both calculations satisfactorily reproduce the experimental spectrum, although the many-body states contributing to each structure of the spectrum may still differ from one calculation to another. The top panel of Fig. 4.13 presents the decom-

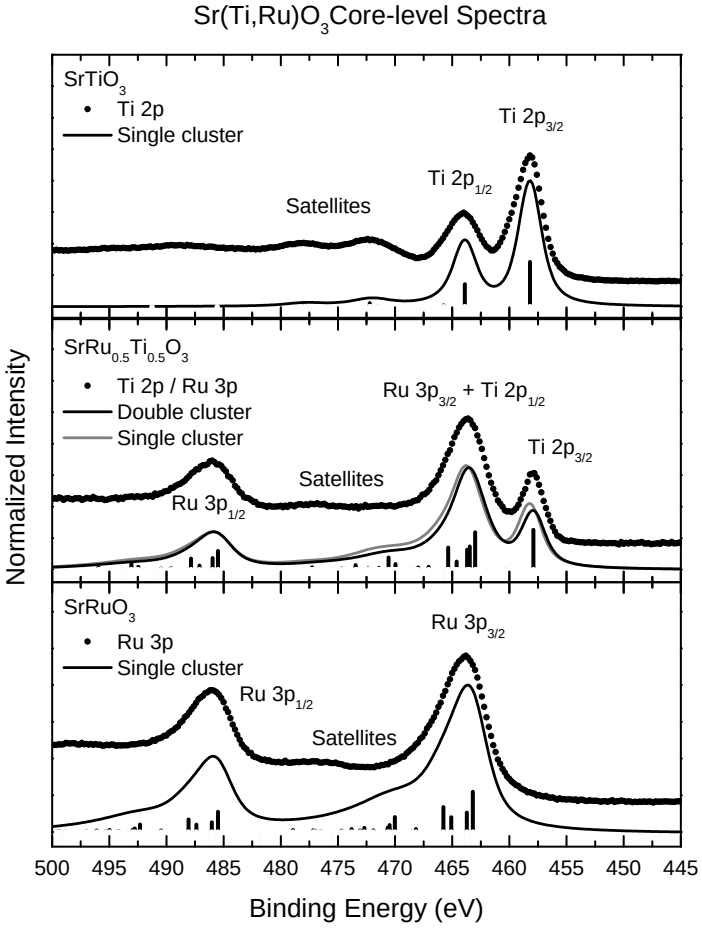

Figure 4.12 Ti 2p and Ru 3p core level photoemission spectra of $SrTiO_3$ (top), $SrTi_{0.5}Ru_{0.5}O_3$ (middle), and $SrRuO_3$ (bottom). The spectra are split, due to spin-orbit effects, into the 3/2 and 1/2 leading structures, which also present satellites. The experimental results are compared to weighted single cluster and double cluster calculations.

position of the calculated core level spectrum with the double cluster into the Ti $2p_{3/2,1/2}$ and Ru $3p_{3/2,1/2}$ contributions. The labels in the figure indicate final states with different dominant configurations, projected in the corresponding ion site, which are displayed in Table 4.3 for clarity. The analysis is given in terms of the different screening mechanisms, from the ground state to each discrete final state, upon the creation of a TM core hole. Depending on the availability of the screening, final states can be labeled well-screened, unscreened, poorly-screened, etc., and one can also keep track on the nature of the screening (from ligand, coherent, etc. bands). The following analysis is performed for the Ti $2p_{3/2}$ and Ru $3p_{1/2}$ parts of the spectra, but they also hold for the other respective component.

The leading structure in Ti $2p_{3/2}$ region of the spectrum (peak A) is mainly composed by the $\underline{c}d^1\underline{L}$ and $\underline{c}d^2\underline{L}^2$ configurations, whereas the satellite (peak B) is dominated

by $\underline{c}d^2\underline{L}^2$ and $\underline{c}d^1\underline{L}$ configurations. In turn, in the Ru $3p_{1/2}$ spectrum, the three main peaks and the satellite, labeled C, D, E and F, are formed by $\underline{c}d^6\underline{LC}$ configurations.

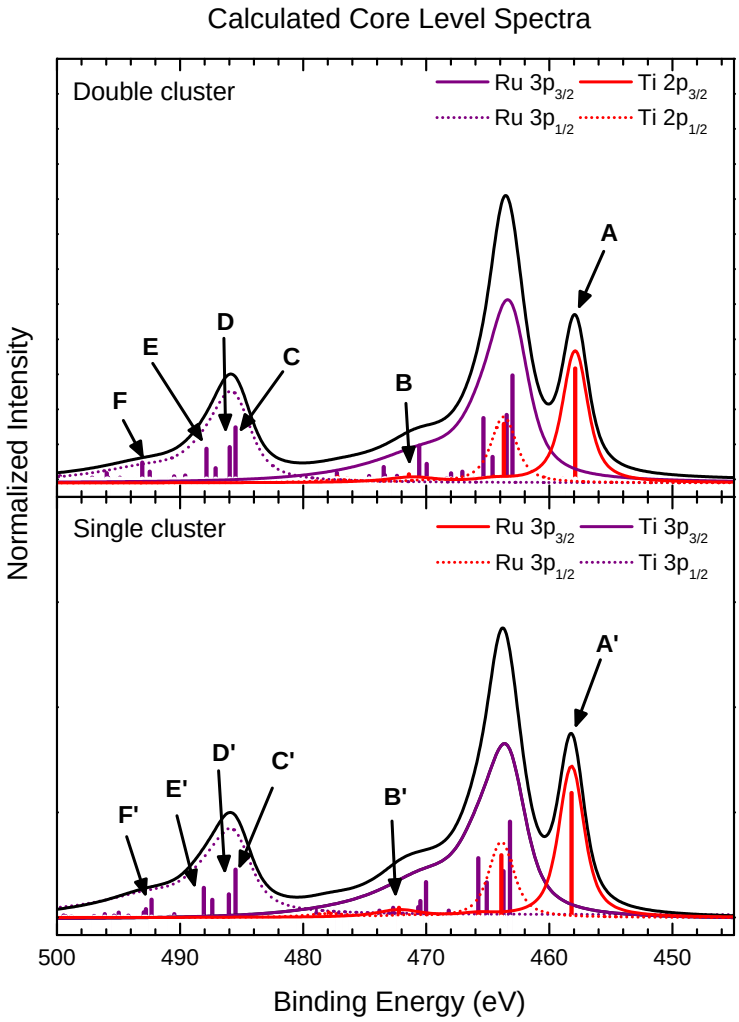

Figure 4.13 Calculated core level spectra with the double (top) and single (bottom) cluster. In the double cluster calculation, the spectra is projected into the Ru and Ti sites. The labels refer to relevant discrete final states and their composition is described in Table 4.3.

For comparison, the bottom panel of Fig. 4.13 presents the single cluster model calculation for the Ti $2p$ (red) and Ru $3p$ (purple) core level spectral weight. For clarity, the relevant contributions to the labeled peaks are also displayed in Table 4.3.

The leading structure in the spectrum (peak A′) is composed by the $\underline{c}d^1\underline{L}$ and $\underline{c}d^2\underline{L}^2$ configurations, whereas the satellite (peak B′) is composed mainly of $\underline{c}d^0$ and $\underline{c}d^2\underline{L}^2$ configurations. On the other hand, the three peaks in the main region of the Ru $3p_{1/2}$ spectrum, labeled C′, D′ and E′ are identified with $\underline{c}d^6\underline{LC}$, $\underline{c}d^6\underline{L}^2$ and $\underline{c}d^6\underline{L}^2$ character, respectively, whereas the structure labeled F′ is mainly due to the $\underline{c}d^5\underline{L}$ configuration [35].

The analysis of the the leading configurations for each of the peaks in the spectra reveals that the introduction of the Ti - Ru interaction in the calculation affects the interpretation of the electronic structure of the double perovskite $SrTi_{0.5}Ru_{0.5}O_3$. In the Ti $3p$ part of the spectrum, the character of the leading peak shifts from well-screened in the single cluster to unscreened in the double cluster, whereas the satellite structure changes from unscreened to poorly-screened. In turn, in the Ru $3p$ spectrum, the structures with ligand (oxygen) screening in the single cluster change to ligand/coherent screening in the double cluster, which fully dominates the spectrum.

The reason for the differences may stem from the fact that both Ti^{4+} e Ru^{4+} ions favor the sharing of an O $2p$ electron in their ground states. In the double perovskite, the GS is governed by charge transfer configurations to such an extent that further ligand screening is not favorable even after the creation of the core hole. As a consequence to the Ti $2p$ spectrum, configurations with $\underline{c}d^2\underline{L}^2$ character dominate the satellite, while they do not appear at all in the Ru $3p$ spectrum, which becomes dominated by states with coherent screening character through the $\underline{c}d^6\underline{LC}$ configuration.

Table 4.3: Dominant final state configurations for selected peaks in the core level spectrum, projected onto their respective site, where $\underline{c}$ represents a core hole.

Double Cluster		Single Cluster	
Peak (site)	Dominant final states	Peak (site)	Dominant final states
A (Ti)	$\underline{c}d^1\underline{L}$, $\underline{c}d^2\underline{L}^2$	A′ (Ti)	$\underline{c}d^2\underline{L}^2$, $\underline{c}d^1\underline{L}$
B (Ti)	$\underline{c}d^2\underline{L}^2$, $\underline{c}d^1\underline{L}$	B′ (Ti)	$\underline{c}d^2\underline{L}^2$, $\underline{c}d^0$
C (Ru)	$\underline{c}d^6\underline{LC}$	C′ (Ru)	$\underline{c}d^6\underline{LC}$
D (Ru)	$\underline{c}d^6\underline{LC}$	D′ (Ru)	$\underline{c}d^6\underline{L}^2$
E (Ru)	$\underline{c}d^6\underline{LC}$	E′ (Ru)	$\underline{c}d^6\underline{LC}$
F (Ru)	$\underline{c}d^6\underline{LC}$	F′ (Ru)	$\underline{c}d^5\underline{L}$

4.2.6 Valence band photoemission spectra

Figure 4.14 presents the X-ray valence band photoemission spectra of $SrTiO_3$, $SrTiO_3$ and $SrTi_{0.5}Ru_{0.5}O_3$. The experimental spectra are compared with the respective calculated removal $(N-1)$ spectra. For the d^0 band insulator $SrTiO_3$, in the top panel, there is no spectral weight until the onset of the O $2p$ band at ≈ 2.0 eV, which extends up to 9.0 eV. The experimental data is compared to the valence band spectrum calculated with

the single cluster model. The theoretical result is in good accordance with the measured data and with previous reports on other Ti^{4+} compounds, such as TiO_2 [104].

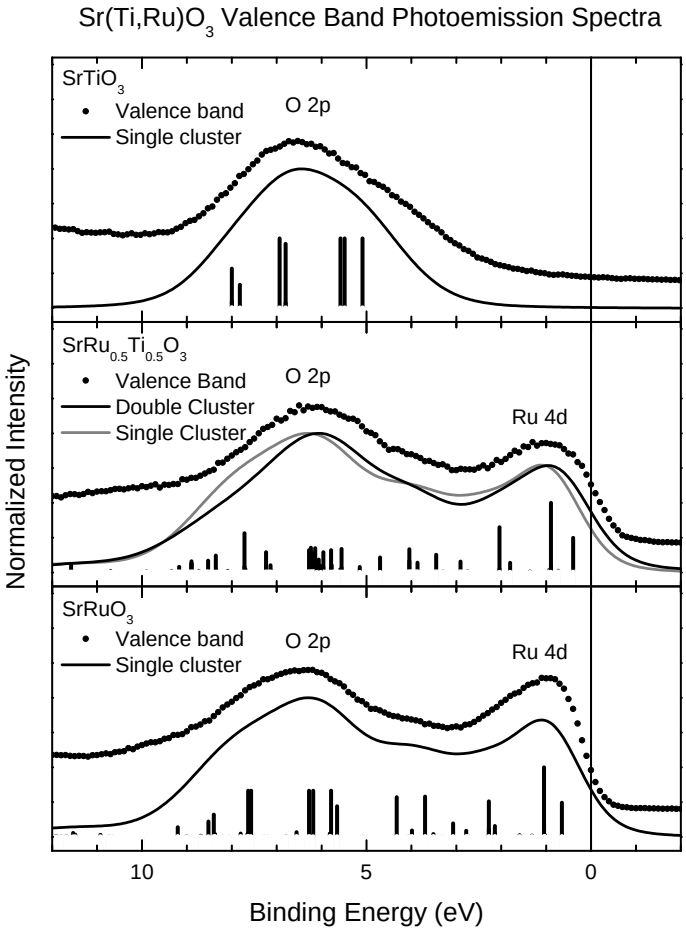

Figure 4.14 Valence band photoemission spectra of $SrTiO_3$ (top), $SrTi_{0.5}Ru_{0.5}O_3$ (middle), and $SrRuO_3$ (bottom). The two main structures in the spectra are related to O $2p$ and Ru $4d$ occupied states. The experimental results are compared to weighted single cluster and double cluster calculations.

For the itinerant ferromagnet $SrRuO_3$, in the bottom panel, the spectrum presents the Ru $4d$ band region, from 3.0 eV to E_F, and the O $2p$ band region, from 10 to 3.0 eV. The low binding energy region presents the so-called coherent and incoherent peaks around 0.5 eV and 2.0 eV, respectively. The calculated removal (N - 1) transitions agree well with the experimental spectrum and also with previous work on $SrRuO_3$ films [35].

The $SrTi_{0.5}Ru_{0.5}O_3$ valence band spectrum is presented in the middle panel. The overall shape of the spectrum resembles the one from $SrRuO_3$, particularly because with this photon energy, the Ru $4d$ photoionization cross-section $\sigma_{Ru\ 4d}$ is at least one order of magnitude greater than $\sigma_{Ti\ 3d}$ [50]. There are no reports of high energy valence

band spectrum for this material, but the present spectrum presents features at the same binding energies as other measurements with photons of 22.1 [99], 40 [98] and 600 eV [37]. The spectrum is compared to double cluster model (black solid line) and the weighted $SrTiO_3$ and $SrTi_{0.5}Ru_{0.5}O_3$ single cluster model calculations (gray line). Both theoretical results successfully reproduce the energy positions and relative intensities of the features in the spectrum.

In order to further analyze the Ru $4d$ weight in the valence band of $SrTi_{0.5}Ru_{0.5}O_3$, Figure 4.15 presents the Ru L_3 resonant photoemission spectra (RPES) of $SrTi_{0.5}Ru_{0.5}O_3$. The inset shows the Ru L_3 XAS and the arrows indicate the photon energies chosen to measure the ON and OFF valence band photoemission spectra, shown in the main panel (solid circles).

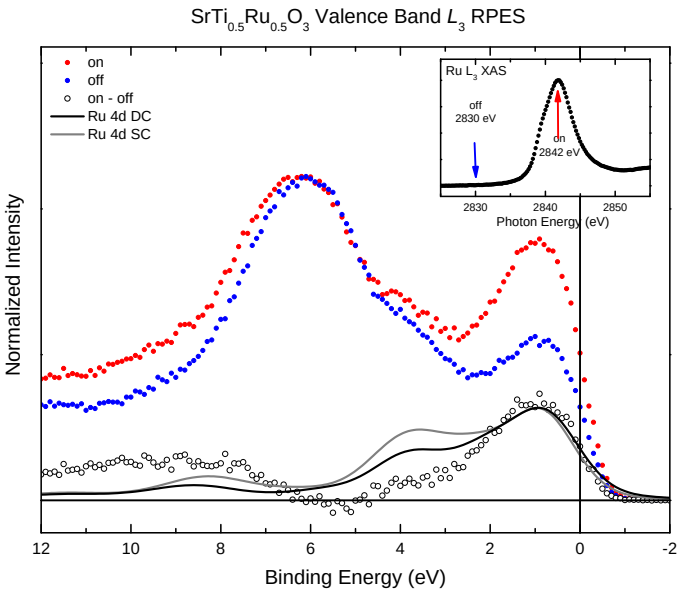

Figure 4.15 Ru L_3 resonant photoemission spectra of $SrTi_{0.5}Ru_{0.5}O_3$. The inset shows the Ru L_3 XAS and the arrows indicate the photon energies used to obtain the valance band spectra in the on ($h\nu$ = 2830 eV) and off ($h\nu$ = 2841.8 eV) conditions. The on - off spectrum is compared to the Ru $4d$ removal spectra calculated with the double and single cluster approaches.

At the off-resonance condition, the spectrum is due to the direct photoemission process, namely, $2p^6 4d^n + h\nu \rightarrow 2p^6 4d^{n-1} + e^-$. However, at the resonance condition, the spectrum is enhanced due to interference with the indirect excitation channel $2p^6 4d^n + h\nu \rightarrow 2p^5 4d^{n+1} \rightarrow 2p^6 4d^{n-1} + e^-$. Thus, the on – off (open circles) spectrum is directly related to the Ru $4d$ character in the valence band due to the virtual $2p^5 4d^{n+1}$ excitation [105].

The difference (on – off) spectrum reveals that Ru $4d$ states appear close to the

Fermi energy, from 0 to 5 eV, and at the bottom of the valence band, from around 7 to 12 eV. The partial Ru 4*d* contribution is compared to the Ru 4*d* removal spectrum, calculated with the double (black) and single (gray) cluster models, which were normalized to the same intensity at the Fermi level. Both results are in agreement with the measured RPES spectrum.

The top panel of Figure 4.16 presents the decomposition of the calculated removal spectra from the double cluster model, as seen in Fig. 4.14, into the partial Ru 4*d*, O 2*p* and Ti 3*d* contribution. The dominant configuration of the labeled peaks, projected only onto the Ru site, are displayed in Table 4.4. Again, the analysis is given in terms of the different screening mechanisms, from the ground state to each discrete final state, upon the removal of a TM valence electron.

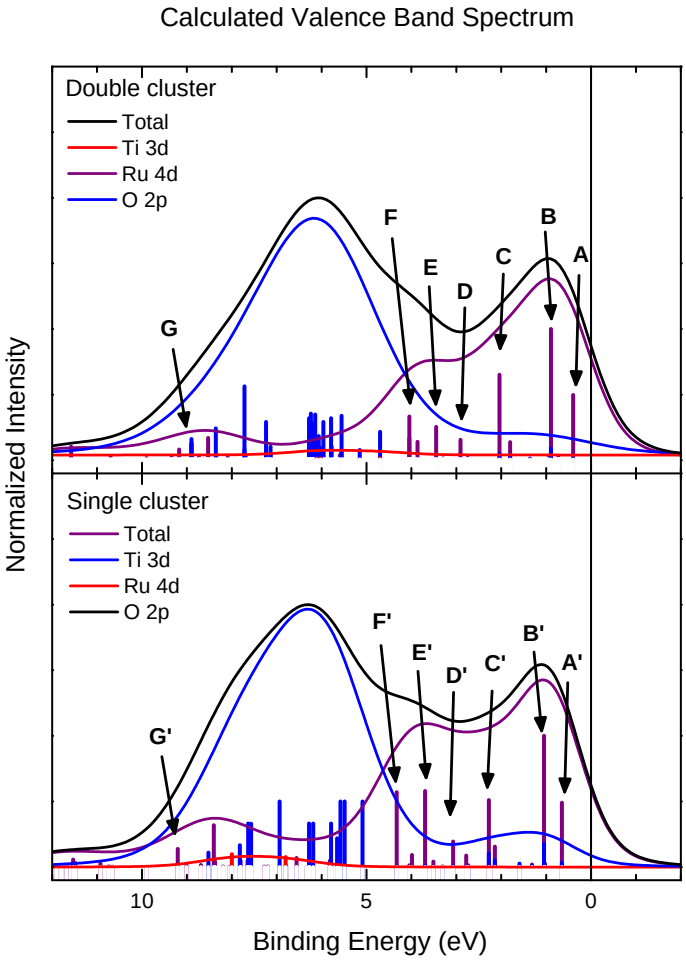

Figure 4.16 Calculated valence band spectra with the double (top) and single (bottom) cluster. In the double cluster calculation, the spectra is projected into the Ru and Ti sites. The labels refer to relevant discrete final states and their composition is described in Table 4.4.

Peaks A, B, D and E are mainly composed of the $d^0\underline{\mathrm{L}}d^4$ and $d^1\underline{\mathrm{L}}^2d^4$ final states,

Table 4.4: Dominant final state configurations, projected in the Ru site, for selected peaks in the valence band spectrum

Double Cluster		Single Cluster	
Peak	Dominant final states	Peak	Dominant final states
A	$d^4\underline{L}$	A′	$d^5\underline{LC}$
B	$d^4\underline{L}$	B′	$d^5\underline{L}^2$
C	$d^5\underline{LC}$	C′	$d^5\underline{LC}$
D	$d^4\underline{L}$	D′	$d^5\underline{L}^2$
E	$d^4\underline{L}$	E′	$d^5\underline{LC}$
F	$d^5\underline{L}^2$	F′	$d^5\underline{L}^2$
G	$d^5\underline{LC}$	G′	$d^4\underline{L}$

which corresponds to a $d^4\underline{L}$ state in the Ru site. After the ejection of the photoelectron, leaving the system with $N-1$ electrons, these configurations can be achieved via three processes: (i) ligand screening on the Ru site; (ii) ligand screening on the Ti site; but also (iii) the absence of screening, due to the different relevant configurations present in the ground state. Peaks C and G are mainly composed of the $d^0\underline{LC}d^5$ final state. Given the calculated GS, this state can be achieved via (i) ligand screening or, (ii) coherent screening. Finally, peak F is mainly composed of the $d^0\underline{L}^2d^5$ final state, which arise from (i) ligand screening, as well as (ii) absence of screening.

For comparison, the bottom panel presents the calculated removal spectra from the weighted single cluster model. The dominant configuration of the peaks presented in the Figure are also displayed in Table 4.4, and have been previously addressed elsewhere [35]. It is evident that the character of the peaks changes from one material to the other. The peaks around E_F are composed by a mixture of $d^4\underline{L}$ states in $SrTi_{0.5}Ru_{0.5}O_3$, rather than $d^5\underline{LC}$ in $SrRuO_3$. The most remarkable difference in the characters of the peaks is the shift to higher binding energies of ligand screened states, such as $d^5\underline{L}^2$. Again, the reason may arise from the (negative) charge transfer regime of both $SrTiO_3$ and $SrTi_{0.5}Ru_{0.5}O_3$, which favors states with holes in the O $2p$ band in the GS, making the system less prone to further ligand screening upon ejection of the photoelectron.

4.2.7 Screening mechanisms and the Ti - Ru octahedra interaction

After analyzing the present results one can argue why the inclusion of the Ti – Ru interaction would be necessary for the description of the electronic structure of $SrTi_{0.5}Ru_{0.5}O_3$ and, moreover, of the $SrTi_{1-x}Ru_xO_3$. Primarily, although positions and intensities do not change, the correct interpretation of the origin of the structures is important for understanding the physical properties of the systems. There are three main aspects concerning the Ti – Ru interaction worth noting.

First, the manifestation of the Ti - Ru interaction clearly depends on the experimental technique. As shown above, the O $2p$ addition spectra calculated with both approaches - single and double cluster - can reproduce the O $1s$ XAS spectra of this system. More importantly, the interpretation of each peak in the spectra is almost identical, so the inclusion of this interaction seems irrelevant for this technique. On the other hand, the core level and valence band photoemission spectra were reproduced with both calculations, but the assignment of the structures in the spectra is quite different. Now, the Ti - Ru interaction appears to be relevant and the main difference comes from the availability of screening mechanisms in each calculation.

Second, whenever the inclusion of this interaction yielded differences in the screening mechanisms, their expected energy positions were not realized. In (negative) charge transfer materials, it is expected that leading structures would present screened character, whereas satellite features would present unscreened/poorly-screened character [61]. In other words, the screening of the photoelectron would be favorable, and the low energy features in the electronic structure of charge transfer materials would have mixed character. This is important for understanding the character and microscopic origin of low energy transitions in TM compounds [57; 61]. Then, the differences in the core level and valence band photoemission spectra of $SrTi_{0.5}Ru_{0.5}O_3$ seen in the double cluster calculation (clearly seen in Tables 4.3 and 4.4), where the Ru - Ti interaction was included explicitly, lead to a different interpretation of its electronic structure.

And third, other important aspect is the fact that transition metal compounds always showed similar trends for the core level and valence band spectra. Namely, both techniques would share the same type of screening mechanisms [35; 96; 106–108]. This is not what happens in $SrTi_{0.5}Ru_{0.5}O_3$ when the Ru - Ti interaction is included in the double cluster model. In fact, according to the calculations, upon ejection of a Ru $4d$ photoelectron in the valence band, unscreened states and states in which the screening happens the Ti sites may contribute to the low energy region of the spectrum. On the

other hand, in the core level spectrum, the low energy region is composed of usual ligand and coherent final states.

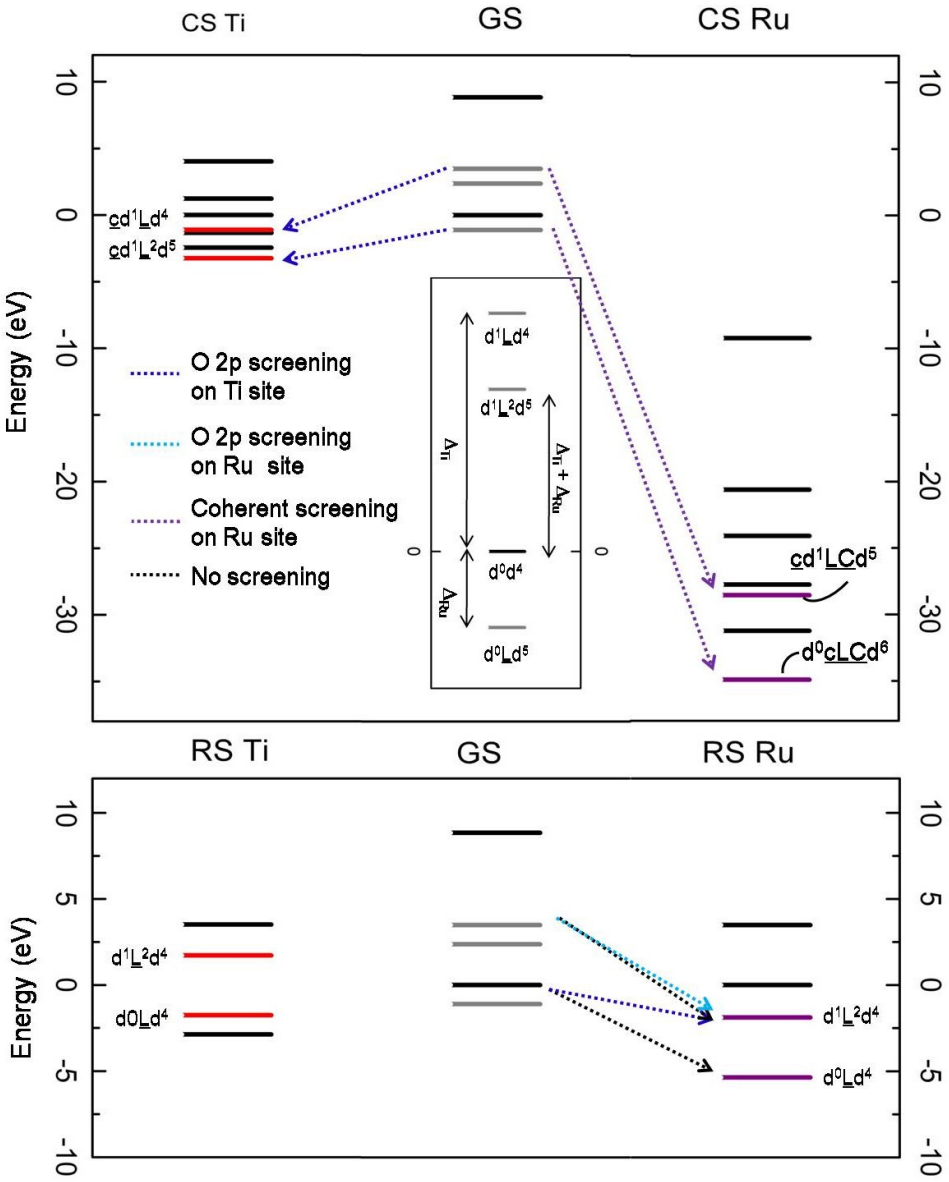

Figure 4.17 Energy levels of the most relevant configurations of the ground, removal and core states basis, used in the double cluster calculations. The arrows in the diagrams represent the screening mechanisms leading to the dominant final configurations of peak A from the valence band spectrum and peaks A and C from the core level spectrum of $SrTi_{0.5}Ru_{0.5}O_3$, which are displayed in Tables 4.3 and 4.4.

In order to clarify the third point, Figure 4.17 shows the energy levels of the most relevant configurations of the ground, removal and core states basis, used in the double cluster calculations. Please, note the reduced scale in the RS part of the Figure. The inset presents the energies of the GS configurations in terms of $\Delta_{Ti,Ru}$, and the

arrows in the diagrams represent the screening mechanisms leading to the dominant final configurations of peak A from the valence band spectrum and peaks A and C from the core level spectrum of $SrTi_{0.5}Ru_{0.5}O_3$, which are displayed in Tables 4.3 and 4.4. After the ejection of the photoelectron, the final states can be achieved by ligand screening either on the Ti site (blue) or on the Ru site (cyan); by coherent screening on the Ru site (purple); and by the absence of screening (black). It is clear that the A peak in the VB spectrum is composed by a richer set of transitions than peak C in the Ru $4p$ core level. This difference may stem from the energy levels of the basis states, which are well separated in the core level, but close together in the valence band, as seen in Figure 4.17. The closeness of the energy levels of the RS basis leads to a more intricate spectrum, as illustrated by the already mentioned contribution of states in which the screening happens the Ti sites upon ejection of a Ru $4d$ electron.

In other words, **the presence of Ti screened final states upon removal of Ru electron is a sign of the coupling of the different octahedra in the valence band**. This conclusion is in contrast with the results from M. Abbate *et al.* [98], which analyzed the valence band photoemission spectra in terms of a Hubbard model (a similar Hamiltonian model which does not include O $2p$ states), and concluded that the Ti $3d$ and Ru $4d$ bands are mostly decoupled. Conversely, the absence of the mentioned states in the core level spectrum indicates that the creation of the core level hole is indeed responsible for decoupling the Ti 3d and Ru 4d bands in the core level photoemission. It is important to note that only the double cluster model, with the explicit inclusion of the Ti – Ru interaction, is capable of capturing these features.

4.3 Summary and conclusions

This part of the work presented the electronic structure of the $SrTi_{1-x}Ru_xO_3$ polycrystals studied with X-ray (resonant) photoemission and absorption spectroscopies, as well as a detailed interpretation of the ES of $SrTiO_3$, $SrTi_{0.5}Ru_{0.5}O_3$ and $SrRuO_3$ with cluster models. In particular, the spectra of $SrTi_{0.5}Ru_{0.5}O_3$ were simulated with a double cluster (DC) with interacting TiO_6 and RuO_6 octahedra, and by properly weighing the $SrTiO_3$ and $SrRuO_3$ single cluster calculations (SC). The spectra for $SrTiO_3$ and $SrRuO_3$ were satisfactorily reproduced with a parameter set in agreement with previous results. The experimental results for $SrTi_{0.5}Ru_{0.5}O_3$ were found to be correctly reproduced with both the DC and SC approaches. However, the compositions of the peaks in the spectra may yield different results depending on the experimental technique and theoretical model. While the XAS results are very similar for both calculations, the core level and valence

band spectra present a noticeable reduction of ligand screening in the DC results. This fact was explained in terms of the position of Ti^{4+} and Ru^{4+} ions in the ZSA diagram, which favors a strongly covalent ground state and inhibits further ligand screening. Further, the core level and valence band spectrum of $SrTi_{0.5}Ru_{0.5}O_3$ present differences in the screening mechanisms, which used to be thought of as similar in other TM oxides. The differences indicate that, in the core level, the creation of a hole by the photoemission process decouples the Ti $3d$ and Ru $4d$ states. In turn, the valence band hole is responsible for enhancing the mixing of the system, as seen for instance in the ligand screening on the Ti site upon removal of a Ru $4d$ electron.

5 Sr_2YRuO_6 and $Sr_2YRu_{0.75}Ir_{0.25}O_6$

Contents

This Section starts with a brief review on the physical properties of Sr_2YRuO_6 and the electronic structure of Sr_2YRuO_6, followed by the motivation to study Ir-substituted samples, along with the description of the preparation and characterization of the samples used in this part of the work. The X-ray spectroscopic results of Sr_2YRuO_6 and $Sr_2YRu_{0.75}Ir_{0.25}O_6$ will be presented and compared with DFT calculations performed with the WIEN2k package. Magnetic moments, orbital occupancies and the density of states close to E_F will be analyzed. This part of the thesis is published in Ref. [109]. The DFT+GGA method is suitable to study this system for a few reasons. Properties such as magnetic moments and orbital occupancies are ground state properties, whose description is the goal of the DFT method. Further, the effect of the spin-orbit interaction can be more easily studied in WIEN2k (and in other DFT codes), in which the SO interaction is already implemented. Finally, because the Ru^{3+} ion presents a full $t_{2g\uparrow}$ level, it is expected that the electron correlation is smaller in Sr_2YRuO_6 than in $SrRuO_3$, as will be further discussed in the following results.

5.1 Introduction

5.1.1 Physical properties

Starting from $SrRuO_3$, the substitution of every other Ru ion by Y originates the double perovskite Sr_2YRuO_6 (Fig. 5.1 a)). This material crystallizes in a monoclinic structure with space group P21/n (#14), in which the RuO_6 and YO_6 octahedra form a three-dimensional checkerboard-like arrangement, as shown in Fig. 5.1 b). Both drawings were made with the software VESTA [33]. Although Sr_2YRuO_6 has been studied since approximately four decades, the origin of some of its physical properties are still under debate [38; 39; 110].

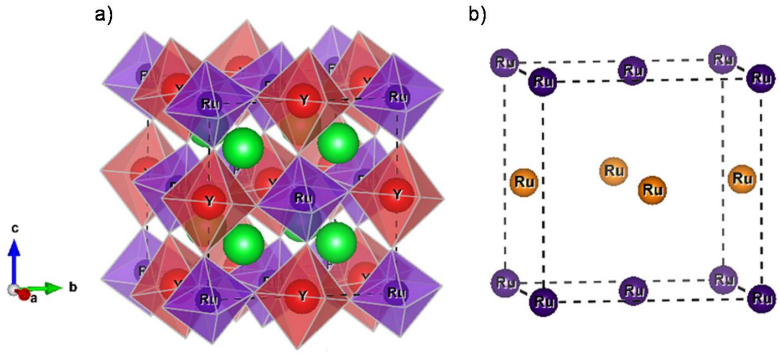

Figure 5.1 Sr_2YRuO_6 crystal structure (a), in which the RuO_6 and YO_6 octahedra form a three-dimensional checkerboard-like arrangement (b). Both drawings were made with the software VESTA [33].

Electrical resistivity measurements of SYRO single crystals showed an uncommon semiconductor behavior [40], as shown in Fig. 5.2. According to the authors, particularly in the 10 K < T < 40 K range, different scattering processes take place and negative magnetoresistance is observed, as shown in the inset. In the crystallographic ab plane, the electrical resistivity is consistent with an activation gap of 76 meV, while this gap for c is 120 meV [40], which could indicate an anisotropic electronic structure.

Although magnetic interactions are thought to arise only from Ru^{5+} ions, SYRO presents two phase transitions, one at $T_{N2} \approx 24$ K and the other at $T_{N1} \approx 32$ K [38; 39]. The existence of two phase transitions and other anomalous magnetic properties presented by this material [40] are believed to stem from the face-centered-cubic (fcc) network formed by the Ru^{5+} ions, shown in Fig. 5.1 b). This arrangement is the simplest 3D structure leading to *geometric frustrated magnetism* [41], or simply frustrated magnetism. This phenomenon arises from strong fluctuations in the magnetic interactions due to a large number of degeneracies in the ground state, resulting in strong short-range interactions,

but no long-range order. The ground state degeneracies, in turn, stem from the geometry assumed by the ions, as illustrated in Fig. 5.3 a) and b).

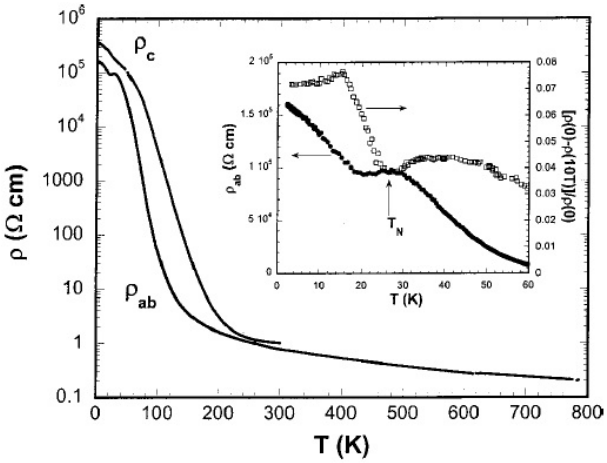

Figure 5.2 Electrical resistivity measurements of SYRO single crystals, showing an anisotropic behavior associated with negative magnetoresistance. Extraced from [40].

Considering antiferromagnetic (AFM) Ising-like $J(\boldsymbol{S_1} \cdot \boldsymbol{S_2})$ interactions, a simple example of how geometry plays a role can be seen analyzing the triangle on the top of the Figure 5.3: if vertexes A and B are to minimize their interaction energy, they must align antiparallel to each other; in this case, vertex C cannot satisfy the AFM interaction with vertexes A and B simultaneously. As a result, statistically, this arrangement coexists with others, such as the triangle below, in the ground state, leading to strong short-range correlations, but no long-range order. Figure 5.3 b) presents the same fcc unit cell (u.c.) of Ru^{5+} ions of Figure 5.1, where the different colors mean opposite spin orientations, with labels of ferromagnetic (FM, red) and AFM (green) interactions. In the left plane of the u.c., all AFM interactions are satisfied. However, the central atom of this plane satisfies only two AFM interactions with the plane passing through the center of the u.c., and interacts ferromagnetically with the other two atoms, leading to frustration. It is worth noting, however, that long-range order was shown to be stabilized by next-nearest-neighbor (NNN) interactions and/or weak anisotropy [41; 111; 112].

Magnetic measurements in single crystals revealed the occurrence of weak ferromagnetism [40], which was attributed to canting of magnetic moments due to Dzyaloshinsky-Moriya interactions (proportional to $\boldsymbol{S_1} \times \boldsymbol{S_2}$) [113; 114], which favors the canting of the otherwise antiparallel, yet collinear, spins. However, Singh and Tomy [115] argued that the reported anomalous magnetic behavior of this compound cannot be explained by these interactions only, while structural changes have also been claimed to be responsible for determining the magnetic ground state of Sr_2YRuO_6 [116]. More recently Granado *et al.* [117], revealed the existence of two-dimensional magnetic correlations in this system

and proposed a partially ordered state between T_{N2} and T_{N1}, stabilized by ferromagnetic interactions between nonconsecutive $YRuO_4$ layers (corresponding to the left and right faces of the magnetic unit cell in Fig. 5.3 b)) in the three-dimensional fcc lattice [117; 118].

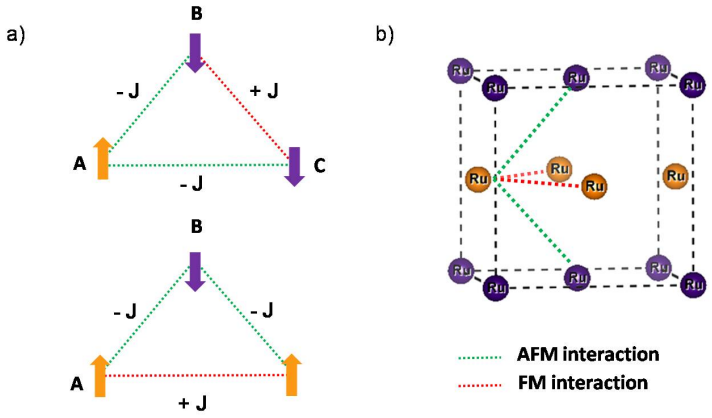

Figure 5.3 a) Representation of the geometric magnetic frustration in a triangular lattice; b) Representation of the geometric magnetic frustration of the Ru^{5+} fcc network in Sr_2YRuO_6.

5.1.2 Electronic structure

In the ionic limit, the divalent Sr^{2+} and trivalent Y^{3+} ions would present an empty $4d$ band, whereas the pentavalent Ru^{5+} ions would show a high-spin $4d^3$ electronic configuration, which is assumed to possess quenched orbital angular momentum. The only theoretical work reported on the ES was done by Mazin and Singh [42], where results from local spin density approximation (LSDA) and tight-binding calculations are analyzed. Their calculations correctly captured the antiferromagnetic semiconducting ground state, with calculated band gap of 0.08 eV. The calculated magnetic moments on the Ru (O) sites yielded 1.70 u_B/Ru ion (0.10 μ_B/O ion), in good agreement with recent neutron diffraction data [117]. Additionally, their results suggested the competition between ferromagnetic and antiferromagnetic interactions in this system.

Fig. 5.4 presents the calculated DOS of one magnetic sublattice of Sr_2YRuO_6 reported in [42], in which the dashed line represents the Ru $4d$ contribution and the dotted line the O $2p$ contribution. Positive (negative) values of N(E) indicate spin up (down) and the dashed line at E = 0 eV represents the Fermi energy. The occupied part of the electronic structure can be split into two main regions: (i) a band dominated by O $2p$ states from -1.5 and -6.0 eV and (ii) a Ru $4d$-derived band from E_F to -1.5 eV. The unoccupied part of the DOS present the Ru $4d$ t_{2g} and e_g structures. Analysis of the calculated density of states resulted in an average occupancy of five electrons in the Ru $4d$

orbitals, indicating strong Ru-O covalence, as also seen in the parent compound $SrRuO_3$. Concerning experimental data, the only study found so far presents X-ray absorption measurements at Ru K, Ru L_3, and O $1s$ level of the $Sr_2YRu_{1-x}Cu_xO_6$ system, motivated by the reports of superconductivity for this series [119; 120].

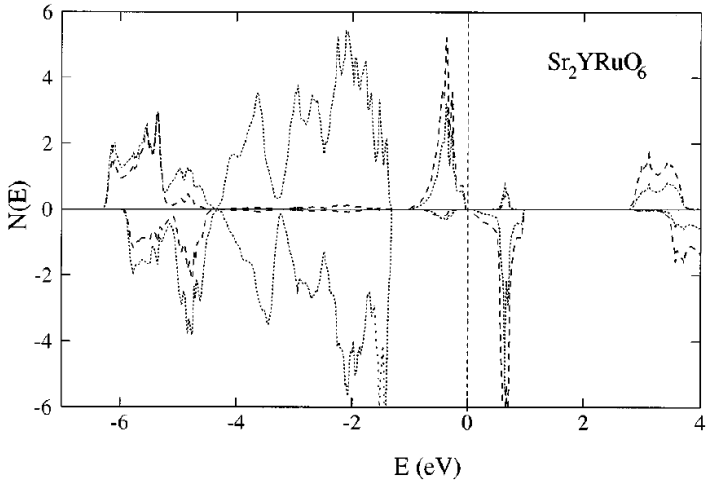

Figure 5.4 Calculated DOS of one magnetic sublattice of Sr_2YRuO_6, extracted from Mazin and Singh [42], in which the dashed line represents the Ru $4d$ contribution and the dotted line the O $2p$ contribution. Positive (negative) values of $N(E)$ indicate spin up (down) and the dashed line at E = 0 eV represents the Fermi energy. The occupied part of the electronic structure is split into a band dominated by O $2p$ states from -1.5 and -6.0 eV and a Ru $4d$-derived band from E_F to -1.5 eV. The unoccupied part of the DOS present the Ru $4d$ t_{2g} and e_g structures.

One possible approach to study the magnetic interactions in SYRO is to analyze the changes in the electronic structure upon replacement of Ru by other magnetic transition metal (TM). A good candidate is Ir, because its 5+ ion possesses almost the same ionic radius as Ru^{5+} [121] which would cause negligible change in the crystal structure of the compound. This substitution not only introduces a less magnetic atom in the Ru^{5+} fcc network, but it also donates one extra electron to the system.

Although very thorough and acclaimed, the important work of Mazin and Singh [42] was performed with less computational resources than are available today, including both hardware and software. Also, the literature regarding experimental results on the electronic structure of this material, and specially on Ir-substituted samples, is scarce. Therefore a study on the electronic structure of this system with X-ray spectroscopic methods and band structure calculations is valuable for the understanding of its physical properties.

5.1.3 Samples Preparation and Characterization

Polycrystalline samples of $Sr_2YRu_{1-x}Ir_xO_6$; $x = 0$ and 0.25 were prepared and characterized with X-ray diffraction and magnetic susceptibility measurements by the Prof. Renato Jardim's group, at University of São Paulo - SP, and are published in [109]. The samples were synthesized by the solid state reaction method, as described in detail elsewhere [117]. Phase identification and unit cell parameters were determined by refining powder X-ray diffraction patterns obtained by a Bruker D8 Discover diffractometer (Cu K_α radiation, $\lambda = 1.5418$ Å) using the Rietveld method (GSAS/EXPGUI package) [102; 103]. The measurements were performed at room temperature in the $15° < 2\theta < 120°$ range with a 0.05° step and 2.0 s counting time per step. Magnetization M(T) measurements were performed in a SQUID magnetometer from Quantum Design in the temperature range between 5 and 300 K under zero-field-cooled (ZFC) and field-cooled (FC) conditions.

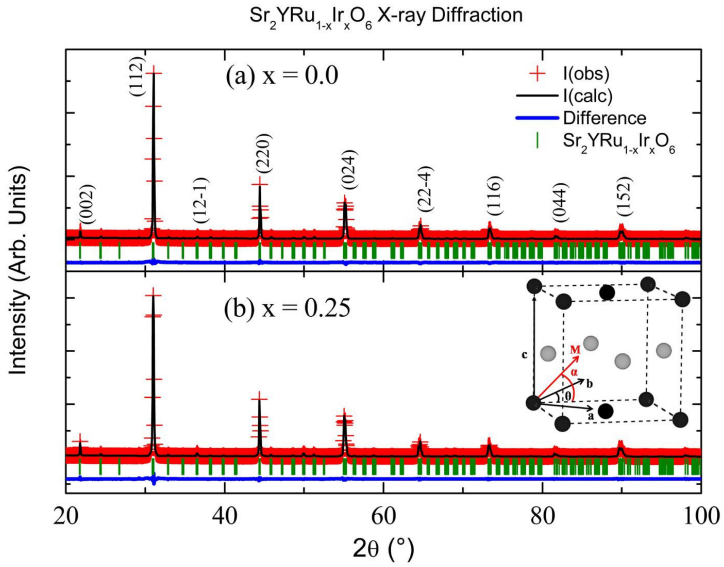

Figure 5.5 X-ray diffraction patterns of the SRY(I)O samples with $x = 0$ (a) and 0.25 (b). The observed (red sign), calculated (black solid line), and difference (blue solid line) diagrams are displayed in the figure. The Rietveld profiles were obtained from diagrams taken at room temperature. The green bars represent the Bragg reflections of the Sr_2RuYO_6 crystal phase. Miller indices of some prominent peaks are marked in (a).

The expanded XRD patterns of the two studied samples $Sr_2Ru_{1-x}Ir_xYO_6$; $x = 0$ and 0.25; are displayed in Figure 5.5. The observed reflections of the unsubstituted compound are very sharp and were indexed on the basis of a monoclinic unit cell, space group $P2_1/n$ with lattice parameters a = 5.7694 Å, b = 5.7782 Å, and c = 8.1617 Å, in excellent agreement with the ones described elsewhere [39; 116; 117; 122]. The partial Ru substitution by Ir has little effect in the XRD diagram (see Fig. 5.5 (b)). The refined lattice parameters of the x = 0.25 sample, a = 5.7657 Å, b = 5.7829 Å, and c = 8.1649 Å, were

found to be changing toward those of the Sr_2IrYO_6 crystal phase [123; 124]. Regarding the ordering of the YO_6 and $Ru(Ir)O_6$ octahedra, although it was not determined in the refinement, it must be pointed that this property depends on mainly two parameters: spontaneous ordering of B-site ions requires a large difference in ionic radius of the TM's. The radius of Y^{3+} is approximately 50% bigger than the radii of Ru^{4+} and Ir^{4+}, which in turn are virtually the same, indicating that TMO_6 order is favorable in both pristine and substituted compounds [125].

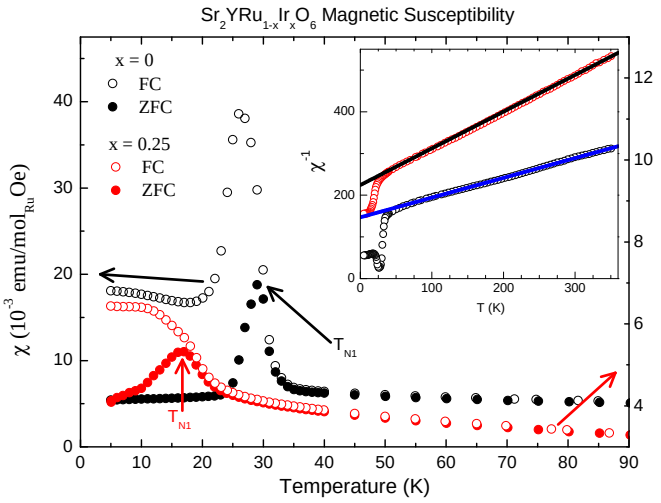

Figure 5.6 Temperature dependence of the magnetic susceptibility, $\chi(T) = M/H$, under an applied magnetic field of 1 kOe, for the two samples studied: Sr_2RuYO_6 and $Sr_2Ru_{0.75}Ir_{0.25}YO_6$. The inset displays the temperature dependence of the inverse magnetic susceptibility χ^{-1} and solid lines are linear fits of the data according to the Curie-Weiss law.

The temperature dependence of the magnetic susceptibility $\chi(T) = M(T)/H$, in the temperature range 5 - 90 K under an applied magnetic field of H = 1 kOe, for samples $Sr_2YRu_{1-x}Ir_xO_6$; x = 0 and 0.25; is displayed in Figure 5.6. The parent compound exhibits two magnetic ordering transitions, marked by arrows in the Figure: (i) at T_{N1} $\sim$ 32 K in the ZFC curve, which couples alternative $YRuO_4$ layers antiferromagnetically; and (ii) at T_{N2} $\sim$ 25 K in the FC curve, which is the ordering of a fully ordered AFM state. These features are in excellent agreement with high-resolution neutron powder diffraction experiments carried out in Sr_2YRuO_6 [117]. The development of AFM order is also observed below a peak at T_{N1} $\sim$ 16 K in the ZFC curve of the $Sr_2YRu_{0.75}Ir_{0.25}O_6$ compound, further indicating that the AFM ordering is still preserved at the level of substitution of x = 0.25. The appreciable decrease in T_{N1} suggests that the magnetic interaction is weakened with the partial substitution of Ru^{5+} by Ir^{5+}, an expected result based on recent magnetic and neutron diffraction data in Sr_2YIrO_6 [124]. It is worth noting that the influence of disorder could also play a role in the decrease of the temperature of magnetic ordering, but it will not be addressed in the following discussion.

Both samples display paramagnetic behavior at temperatures T $\gg$ T_{N1}, a feature confirmed by the linear behavior of the temperature dependent inverse magnetic susceptibility χ^{-1}(T) shown in the inset of Figure 5.6. Curie-Weiss fits to the χ^{-1}(T) vs. T data over the paramagnetic region (50 - 350 K) yielded an effective moment μ_{eff} = 3.88 μ_B/Ru for the Sr_2YRuO_6 compound, a value very close to 3.87 μ_B of isolated Hunds rule ground state of Ru^{+5} ion, and in agreement with a previous study [38]. We have also found a smaller effective magnetic moment μ_{eff} = 2.86 μ_B/Ru in the Ir-substituted sample. This value is in agreement with the μ_{eff} = 0.91 μ_B/Ir extracted from the Curie-Weiss fit in the pure Sr_2YIrO_6 (SYIO) compound [124].

The negative Weiss temperatures, Θ_{CW}, obtained from fits of χ^{-1}(T) curves under H = 5 kOe were $|\Theta_{CW}| \sim$ 292 and 214 K, for samples with x = 0 and 0.25, respectively. The high values of $|\Theta_{CW}|$ resulted in frustration parameters $|\Theta_{CW}|/T_{N1} \sim 9$ (or $\sim$ 12 when T_{N2} is considered) and $\sim$ 13, respectively, further indicating the presence of magnetic frustration that increases little with increasing Ir content in this series.

5.1.4 Calculation details

The band structure calculations were carried out within the Full Potential Linearized Augmented Plane Wave + localized orbitals method, as implemented in the WIEN2k package [75; 76] using the PBE-sol exchange-correlation potential [126]. The **k** integration was carried out using 172 points in the irreducible part of the first Brillouin Zone, and the energy convergence was set to 1 $\times$ 10^{-5} eV. The lattice parameters and atomic positions used in the calculations of Sr_2YRuO_6 were determined experimentally by neutron powder diffraction 117 and are given in Table 5.1.

Paramagnetic (P)[1], ferromagnetic (FM) and AFM orderings were admitted. The P and FM solutions for both compounds were found using the experimental monoclinic crystal structure determined by neutron diffraction measurements. In turn, the AFM solution was obtained using a supercell of $\sqrt{2} \times \sqrt{2} \times 1$ derived from the experimental monoclinic structure, which can be regarded as a pseudo-cubic structure with lattice parameters a' $\sim$ b' $\sim$ c', as described in Ref. [117]. This arrangement results in a Ru^{5+} fcc network with four equivalent ruthenium atoms, split into two sub-networks polarized antiparallel to each other. Then, the 25% substitution of Ru for Ir was simulated by replacing one Ru atom by an Ir atom of equal spin polarization. As mentioned, this substitution causes a very small change in the lattice parameters, as confirmed by DRX results. For this

[1]Rigorously, this calculation is *non-magnetic*, although the term paramagnetic is used in the DFT community to denote a calculation where spins are not included.

reason, the same crystal structure was used for the Sr_2YRuO_6 and $Sr_2YRu_{0.75}Ir_{0.25}O_6$ calculations.

Table 5.1: Crystal structure of Sr_2YRuO_6 extracted from [117].

Lattice Parameters (Å)			
a =5.766 b = 5.786 c = 8.176			
Atomic Positions			
	x	y	z
Sr	0.5073	0.53050	0.2489
Y	0	0.5	0
Ru	0.5	0	0
O_1	0.2312	0.2004	-0.0351
O_2	0.3027	0.7295	-0.0382
O_3	0.4331	-0.0127	0.2347

It has been shown recently that spin-orbit (SO) coupling can lead to novel physics, particularly in $5d$ TM's [127; 128]. In light of this fact, SO coupling was included in all TM valence d orbitals via the second variational method, as implemented in the WIEN2k package [75; 76]. It is then necessary to establish a magnetization axis **M**, *i.e.*, to choose a quantization axis for $\hat{\boldsymbol{S}}$ in equation 3.30. Since recent neutron diffraction measurements have shown that the spins align in the monoclinic b direction, the direction of M can be uniquely defined by the angle α, depicted in Fig. 5.5 (b). It is important to note that the X-ray spectra in Sections 5.2.1, 5.2.2 and 5.2.3 are compared with calculations where the SO coupling was included, while the effects of treating or not this interactions is discussed in Section 5.2.4.

5.2 Results

5.2.1 Valence band photoemission spectra

The top panel of Figure 5.7 shows the measured valence band (VB) photoemission spectra for the SYRO and SYRIO compounds. The spectra were obtained with a photon energy of 2830 eV and the solid line at zero energy denotes the Fermi energy. Both samples present insulating behavior, presenting two major regions: (i) an O $2p$ derived band, split into bonding and non-bonding states, from around 10 eV to about 3 eV, and (ii) a Ru $4d$ (and Ir $5d$) rich region, from 3 eV to 0 eV. The main differences between both spectra are

a slight shift in the O $2p$ band and a small increase in the relative intensity at the top and bottom of the valence band.

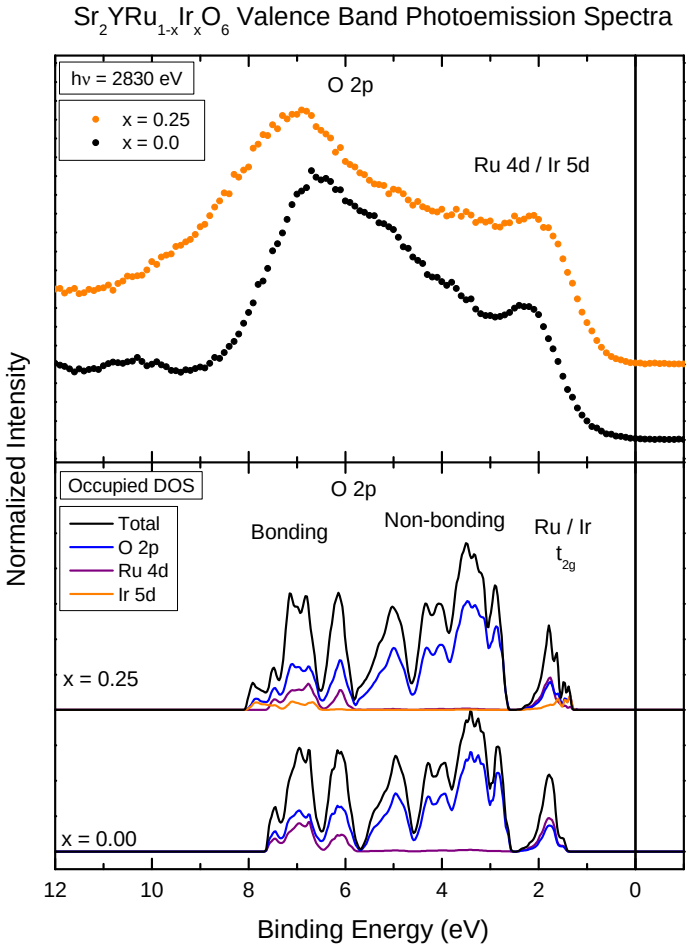

Figure 5.7 Top: valence band photoemission spectra of Sr_2YRuO_6 and $Sr_2YRu_{0.75}Ir_{0.25}O_6$. Bottom: calculated occupied densities of states (DOS) for both compositions. The total DOS is projected into the O $2p$, Ru $4d$ and Ir $5d$ contributions.

The bottom panel of Figure 5.7 presents the calculated occupied densities of states (DOS) for both compositions, calculated with the WIEN2k package, with the respective O $2p$, Ru $4d$ and Ir $5d$ projections. Since there is no reliable data on the photoionization cross section of each contribution for the photon energy used in the measurements, the calculations were not corrected for this effect. However, the values at hν = 1500 eV give $\sigma_{Ru4d}/\sigma_{O2p}$ and $\sigma_{Ir5d}/\sigma_{O2p}$ ratios of the order of 10. Allowing these ratios to be at least of the same order for hν = 2830 eV, this correction would then increase the relative intensity of the Ru $4d$ and Ir $5d$ states, thus being in good agreement with the valence band photoemission spectra.

According to the simulation, the Ru $4d$ states appear at the top and bottom of the

valence band, mixed with O $2p$ states, and are mainly responsible for the two prominent structures in the experimental spectra. Further, the Ir $5d$ states appear closer to the Fermi energy than the Ru $4d$ states, in the x = 0.25 calculation, and also at the bottom of the valence band, which is consistent with the small increase in spectral weight at these energy regions. Finally, the spectra from 3 to 6 eV are dominated by almost pure non-bonding O $2p$ states.

5.2.2 Resonant photoemission spectra

Figure 5.8 presents the Ru L_3 resonant photoemission spectra (RPES) of Sr_2YRuO_6 and $Sr_2YRu_{0.75}Ir_{0.25}O_6$. The top and bottom panels show the OFF, ON1 and ON2 spectra for the SYRO and SYRIO compounds, respectively. The lines indicate the subtraction of the ON relative to the OFF spectrum, which are compared to the Ru $4d$ projection of the calculated occupied DOS.

The inset shows the Ru L_3 X-ray absorption spectra (XAS) of the samples, where the arrows indicate the photon energies used in the RPES. The off-resonance spectrum (OFF) was obtained at 2830 eV, whereas the two on-resonance spectra were taken at 2840.8 eV (ON1) and 2843.6 eV (ON2). The energy separation of the corresponding structures in the XAS spectra, which is about 3.8 eV, is consistent to the crystal field splitting 10 Dq in these compounds (see below). Thus, the first energy is mainly related to transitions from the Ru $2p_{3/2}$ level to the unoccupied Ru $4d$ t_{2g} states, whereas the second is mostly related to transitions from the Ru $2p_{3/2}$ level to the unoccupied Ru $4d$ e_g states.

At the off-resonance condition, the spectrum is due to the direct photoemission process [105], namely, $2p^6 4d^n + h\nu \rightarrow 2p^6 4d^{n-1} + e^-$. However, at the on-resonance condition, the spectrum is enhanced due to interference with the indirect excitation channel $2p^6 4d^n + h\nu \rightarrow 2p^5 4d^{n+1} \rightarrow 2p^6 4d^{n-1} + e^-$. Thus, the ON – OFF spectrum is directly related to the Ru $4d$ character in the valence band due to the virtual $2p^5 4d^{n+1}$ excitation. The present Ru L high energy RPES presents some advantages in comparison to RPES measurements in M or N edges. The first is that the signal enhancement due to the L_3 edge absorption is large enough to provide satisfactory signal–to–noise ratio. We have also attempted to perform RPES in the Ir M_3 edge, but the signal enhancement was not sufficient to obtain a reliable ON – OFF spectrum. Also, when compared to the Cooper minimum method, Ru L RPES does not suffer from effects of photoionization cross section, since the difference between the energies of the on- and off-resonance spectra is small (about 0.4%) [50]. Finally, the spectra are less surface sensitive because with these incident photon energies the photoelectron escape depth is around 30 Å [54].

The positive enhancement to the spectra in the ON(1,2) conditions appear close to the Fermi energy, around 0 and 3 eV, and at the bottom of the valence band, about 6 to 9 eV, which is in agreement with the calculated DOS. The main differences between each system are the relative intensity of the RPES signal, which is higher for the SYRO system. Further, the RPES enhancement at the bottom of the valence band appears at lower binding energies, in the SYRIO compound.

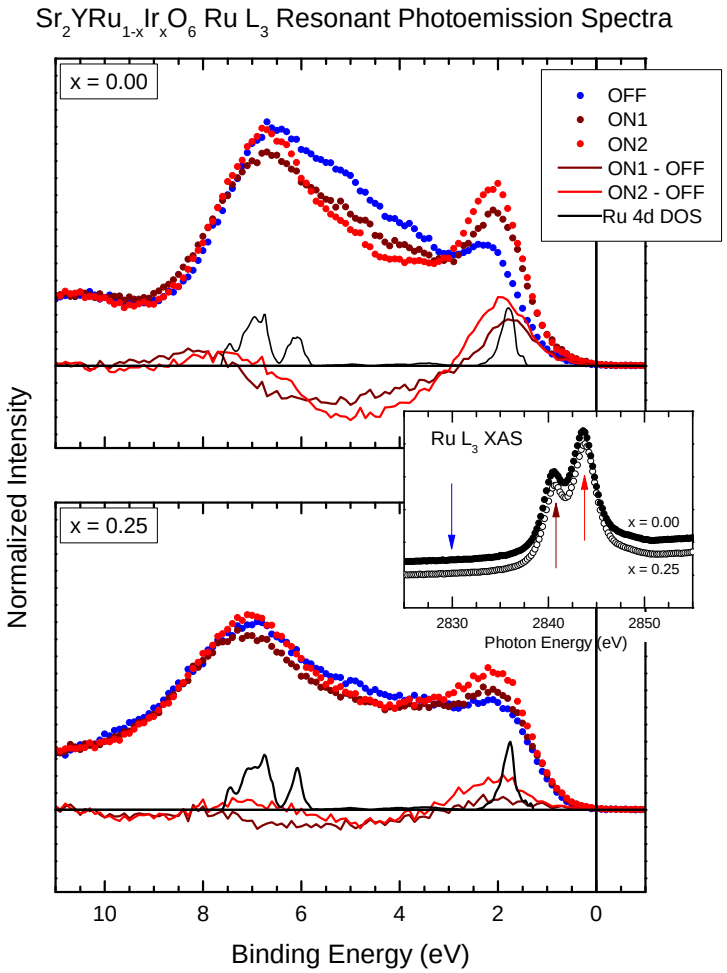

Figure 5.8 Ru L_3 resonant photoemission spectra (RPES) of Sr_2YRuO_6 and $Sr_2YRu_{0.75}Ir_{0.25}O_6$. The inset shows the Ru L_3 X-ray absorption spectra (XAS) of the samples, where the arrows indicate the photon energies used in RPES. The ON1 (2840.6 eV) and the ON2 (2843.8 eV) spectra are subtracted from the OFF (2830 eV) spectrum and compared to the calculated Ru $4d$ DOS.

The RPES spectra of both systems are somewhat different than for $SrRuO_3$ [35], in which the Ru^{4+} ions show a low-spin $4d^4$ (three $t_{2g,\downarrow}$ and one $t_{2g,\uparrow}$ electrons) electronic configuration. In the latter, a positive RPES signal appears close to the Fermi energy, but

also at around 4 eV, showing a considerable amount of Ru 4*d* weight in the O 2*p* region. Further, the SRO RPES spectrum presents significant intensity at approximately 10 eV [35].

The differences found between the Ru 4*d* spectral weight in $SrRuO_3$ and Sr_2YRuO_6 cannot be accounted for in terms of a rigid band shift picture, *i.e.* a simple shift in the Fermi level due to hole doping from Ru^{4+} to Ru^{5+}. It is possible that changes in the Coulomb interaction (Hubbard U), O 2*p* – Ru 4*d* charge transfer energy (Δ) place the Ru^{5+} ion in SYR(I)O in a region of the Zaanen-Sawatzky-Allen diagram [61] different than the Ru^{4+} ion. Judging by the position of the Ru 4*d* feature at the bottom of the valence band in RPES spectrum of Sr_2YRuO_6 and $Sr_2YRu_{0.75}Ir_{0.25}O_6$, this region should have a lower $U_{Ru^{3+}}$ than the value $U_{Ru^{4+}}$ reported for $SrRuO_3$ and $SrTi_{0.5}Ru_{0.5}O_3$ in Section 4.2.3 (please, refer to the Negative Charge Transfer regime in Figure 3.5), which justify the use of the DFT approach with the GGA approximation study this material. Other important ingredient might be the interaction among the different Ru(Ir)O_6-YO_6 octahedra, which indicates that the electronic structure of SYRO should still be investigated with the Double Cluster model, taking into account many-body effects beyond the DFT+GGA method and also treating explicitly the Ru(Ir)O_6 - YO_6 interaction.

5.2.3 O 1*s* X-ray absorption spectra

The top panel of Figure 5.9 shows the O 1*s* X-ray absorption spectra of Sr_2YRuO_6 and $Sr_2YRu_{0.75}Ir_{0.25}O_6$. The spectra are related to transitions from O 1*s* to empty O 2*p* states, which reflects the different metal bands, via hybridization. The structures at 529 eV, 531 eV and 532 eV arise from O 2*p* states mixed with Ru 4*d* and/or Ir 5*d* states. In octahedral symmetry, the five Ru 4*d* (Ir 5*d*) orbitals are split into the t_{2g} and e_g bands, as indicated in Fig. 5.9. From 533 eV to 540 eV, the O 2*p* states hybridize with Y 4*d* and Sr 4*d* states, and, at higher energies, the spectra are associated to an O 2*p* - Ru 5*sp* combination. The main difference in the spectrum of each compound is the decrease in intensity of the first e_g peak, at 531 eV, relative to the second e_g peak, at 532 eV.

The bottom panel of Figure 5.9 presents the calculated DOS projected on the unoccupied O 2*p* orbitals of $Sr_2YRu_{1-x}Ir_xO_6$. For $x = 0$, the partial DOS consists of O 2*p* orbitals mixed with Ru 4*d* t_{2g}, at about 528.7 eV, and Ru 4*d* e_g, from around 530.7 eV to 532.4 eV. At higher energies, O 2*p* orbitals appear hybridized with Y 4*d* (533 eV), Sr 4*d* (535 eV), Y 4*d* (538 eV) and Ru 5*sp* (542 eV), as labeled in Fig. 5.9. For the x = 0.25 compound, the higher energy region, above 533 eV, remains practically unchanged, whereas the lower energy region has a new contribution from Ir 5*d* states. The Ir t_{2g} states

show up as a new peak in the DOS, at 528.2 eV, while the Ir e_g DOS contribute to the same region as the Ru e_g states.

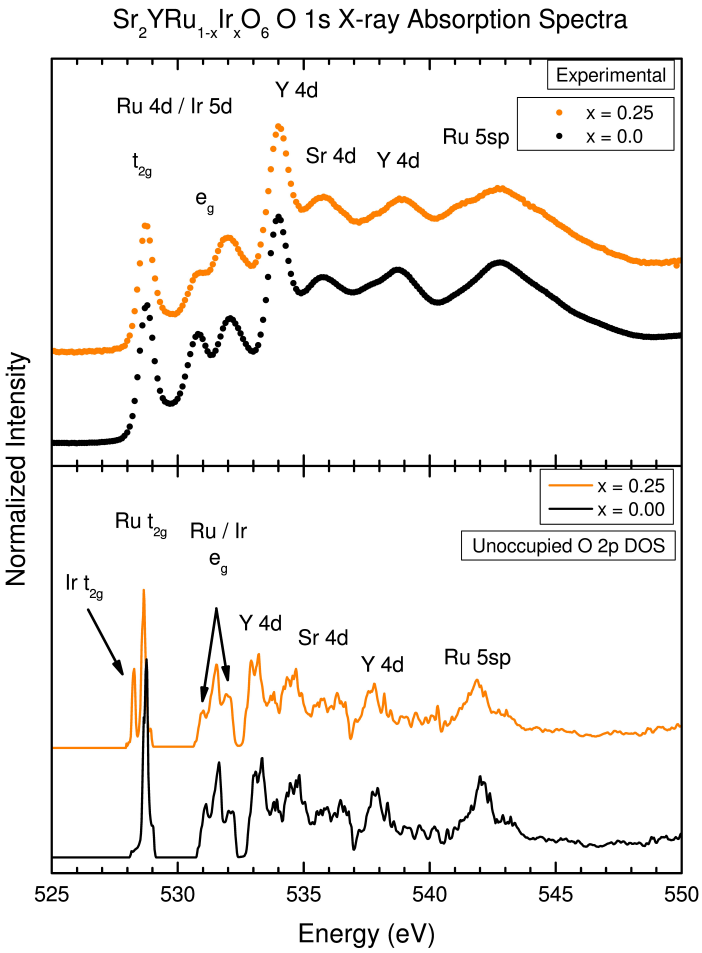

Figure 5.9 O 1s X-ray absorption spectra of Sr_2YRuO_6 and $Sr_2YRu_{0.75}Ir_{0.25}O_6$. This technique is related to the O $2p$ unoccupied states, which are covalently mixed with different metal bands. The experimental spectra are compared to the calculated DOS projected into the unoccupied O $2p$ orbitals.

The structures in the O $2p$ DOS are in good agreement with the O $1s$ XAS spectra, although the position of the higher energy structures are slightly underestimated. The decrease in the relative intensity of the first e_g peak seen in the experimental data is reproduced by the DOS presented here. On the other hand, the two t_{2g} structures in the $x = 0.25$ DOS could not be resolved by the experiment. One hypothesis is that the peak could not be resolved due to the experimental energy resolution, which is of around 0.4 eV. However, since a broadening of the t_{2g} structure is not observed, which would be expected in case a Ir state appeared close to the Ru state, it is also possible that both unoccupied Ru $4d$ and Ir $5d$ states fall superimposed on the same energy.

5.2.4 Ground state properties and density of states

The good agreement between the experimental and theoretical data shows that the calculation provides a satisfactory description of the electronic structure of SYR(I)O. Now, we proceed to the analysis of the ground state properties and the total DOS. The ferromagnetic (FM) solution resulted in a total energy approximately 40 meV and 80 meV lower than the paramagnetic (P) solution for $x = 0$ and $x = 0.25$, respectively. In turn, the antiferromagnetic (AFM) solution yielded a total energy around 12 meV lower than the FM solution in the $x = 0$ compound, and about 20 meV lower for the $x = 0.25$ system.

The AFM solution for $x = 0$ resulted in magnetic moments of 1.66 μ_B/Ru ion and 0.10 μ_B/O ion. These results are in agreement with the calculation presented in Ref. [42], as well as with data from neutron diffraction (NPD) experiments, as shown in Table 5.2. On the other hand, the AFM solution for $x = 0.25$ actually resulted in a semiconducting and ferrimagnetic (FiM) state, with total magnetic moment of 1.99 μ_B/cell. For the RuO_6 octahedra, the calculated magnetic moments resulted in 1.65 μ_B/Ru, 0.10 μ_B/O_{Ru}, while for the IrO_6 octahedra the magnetic moments found are -0.45 μ_B/Ir and -0.04 μ_B/O_{Ir}. It is worth noting that the resulting non-vanishing total magnetic moment, which leads to the FiM state, regards only the calculated unit cell, and it does not mean that the macroscopic behavior of the sample will be FiM.

Table 5.2: Calculated and measured magnetic moments, in units of μ_B, for the Sr_2YRuO_6 compound.

	Calculated		NPD	
	This work	Ref. [42]	Ref. [117]	Ref. [39]
μ_{Tot}	0.00	–	–	–
μ_{Ru}	1.66	1.70	1.96	1.85
$\mu_{O_{Ru}}$	0.10	0.10	0.06	–

Figure 5.10 presents the calculated the AFM densities of states of Sr_2YRuO_6 and $Sr_2YRu_{0.75}Ir_{0.25}O_6$, for both up and down magnetic sublattices. The majority and minority spin contributions to the DOS are displayed in the positive and negative y-axis, respectively. The total DOS is projected into the Sr $4d$, Y $4d$, Ru $4d$, Ir $5d$ and O $2p$ orbitals, as indicated in the legend. In the top panel, the $x = 0$ DOS can be divided into four main regions. In the occupied states, the O $2p$ band extends from -6.2 eV to -1.2 eV, clearly presenting distinct bonding and non-bonding character. The anti-bonding Ru t_{2g} states appear from -1 eV to the Fermi energy largely mixed with O $2p$ states. On the

positive energy region, the empty part of the Ru $4d$ t_{2g} states extends to 1 eV. A crystal field splitting of roughly 10 $Dq \sim 4.0$ eV centers the Ru e_g states at around 3.5 eV, which are in turn split by $J \sim 1$ eV due to the intra-atomic exchange. The Y $4d$ and Sr $4d$ orbitals begin to contribute at around 5 eV.

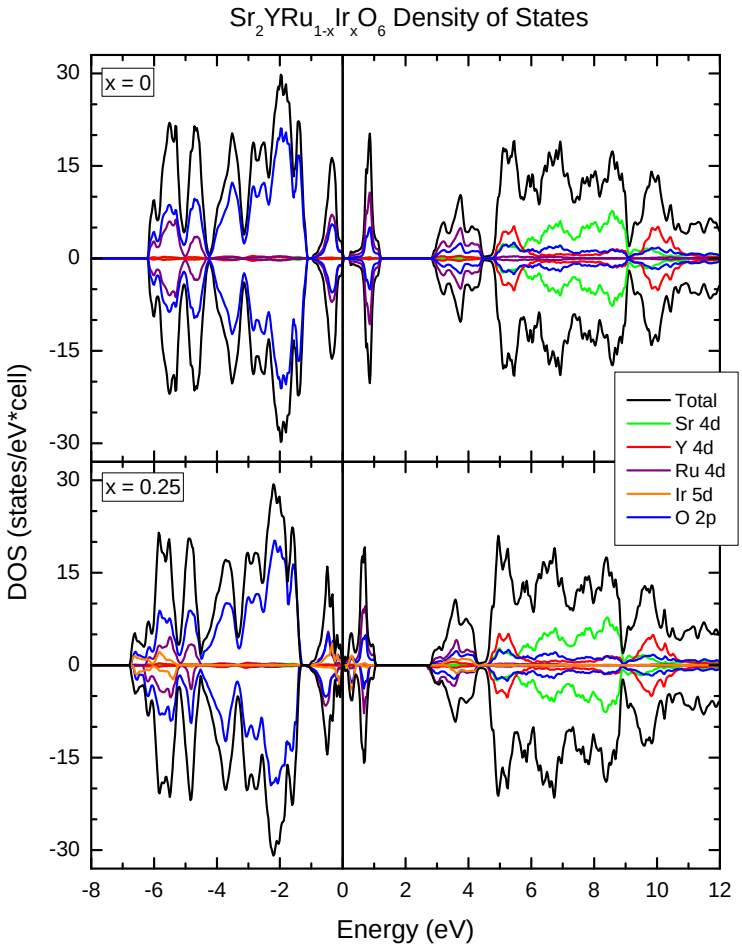

Figure 5.10 Calculated densities of states (DOS) of Sr_2YRuO_6 and $Sr_2YRu_{0.75}Ir_{0.25}O_6$. The total DOS is projected into the Sr $4d$, Y $4d$, Ru $4d$, Ir $5d$ and O $2p$ orbitals, as well as in the majority and minority spin contributions.

The substitution of Ru by Ir causes changes in the DOS, as shown in the bottom panel of Figure 5.10. At the bottom of the VB, the O $2p$ – Ir $5d$ bonding states appear between -6.7 eV and -5.2 eV, increasing the bandwidth of the O $2p$ band by approximately 0.4 eV. The occupied Ir $5d$ states with t_{2g} symmetry appear around the Fermi level, mixed with Ru $4d$ t_{2g} and O $2p$ states. The empty Ir $5d$ t_{2g} states are located just above the Fermi level, followed by the Ru $4d$ t_{2g} states from 0.1 to 1.1 eV. The unoccupied Ru $4d$ e_g band appears from 2.8 eV to 4.3 eV, mixed with Ir $5d$ e_g states from 3.3 eV to 4.3 eV. Further, Y $4d$ and Sr $4d$ states remain practically unchanged at higher energies. Finally,

the calculated band gaps are around 0.24 eV and 0.10 eV for the pure and substituted compounds, respectively. The calculated gap for the x = 0 compound agrees with the measured value of around 0.1 eV [40].

5.2.5 Spin-orbit interaction

The growing interest in materials containing Ir lies in the new physics generated by the importance of spin-orbit (SO) coupling. The magnitude of the SO interaction ξ increases from 0.01 eV in $3d$ TM's, to 0.1 eV in $4d$ TM's, and 0.5 eV in $5d$ TM's. Thus, this effect is negligible in $3d$ compounds, but it needs to be considered explicitly in $4d$ and $5d$ systems because it is of the same order as other interactions such as Coulomb and non-cubic (O_h symmetry) crystal fields [124; 127; 128].

The calculations shown here were performed for a collinear spin arrangement, with the magnetization axis **M** (defined by the angle α) parallel to the b axis of the monoclinic structure, as suggested by neutron diffraction results [117]. In fact, these calculations indicate a total energy decrease of about 100 meV compared to calculations where **M** points along the pseudocubic b' axis. Unfortunately, the energy difference among calculations with distinct values of α of was of the same order of the convergence parameter, and a reliable value for this angle could not be found.

Figure 5.11 compares the calculated DOS for $Sr_2YRu_{0.75}Ir_{0.25}O_6$ with and without the inclusion of spin-orbit coupling in the Ir $5d$ and Ru $4d$ valence orbitals. Each coupling was included separately, which is not shown here, but the real effect to the DOS comes only from the Ir $5d$ SO. As expected, the main change occurs from -1 eV to 1 eV region, which is dominated by Ru $4d$ and Ir $5d$ t_{2g} states. In the top panel of Figure 5.11, the minority Ir $5d$ t_{2g} peak crosses the Fermi level, rendering this calculation a metallic ground state. The inclusion of the SO interaction, shown in the lower panel, is responsible for splitting this peak, suppressing the DOS at the Fermi energy, which signals a tendency towards the true semiconducting behavior. The two structures closer to the Fermi level are then assigned as the occupied and unoccupied parts of the so-called $j_{eff} = \frac{1}{2}$ state, as described in details in Ref. [127]. Under octahedral crystal field, the d orbitals split into t_{2g} and e_g symmetries. Usually, $4d$ and $5d$ orbital present a crystal field splitting large enough to yield a low-spin configuration with filled t_{2g} and empty e_g orbitals if there are less than 6 electrons to populate these orbitals), which is the case of the Ir^{4+} ions. On the other hand, without the presence of a crystal field, the spin-orbit interaction would split the d orbitals in two subsets, with with total angular momenta $J = \frac{3}{2}$ and $J = \frac{5}{2}$. The combination of both ingredients leads to the splitting of the t_{2g} band into an effective

total angular momentum $J_{eff} = \frac{3}{2}$ quartet and $J_{eff} = \frac{1}{2}$ doublet bands. Since the Ir^{4+} ion presents 5 valence d electrons, the $J_{eff} = \frac{3}{2}$ quartet is completely filled, while the remaining electron occupy the $J_{eff} = \frac{1}{2}$ doublet, which becomes semi-filled.

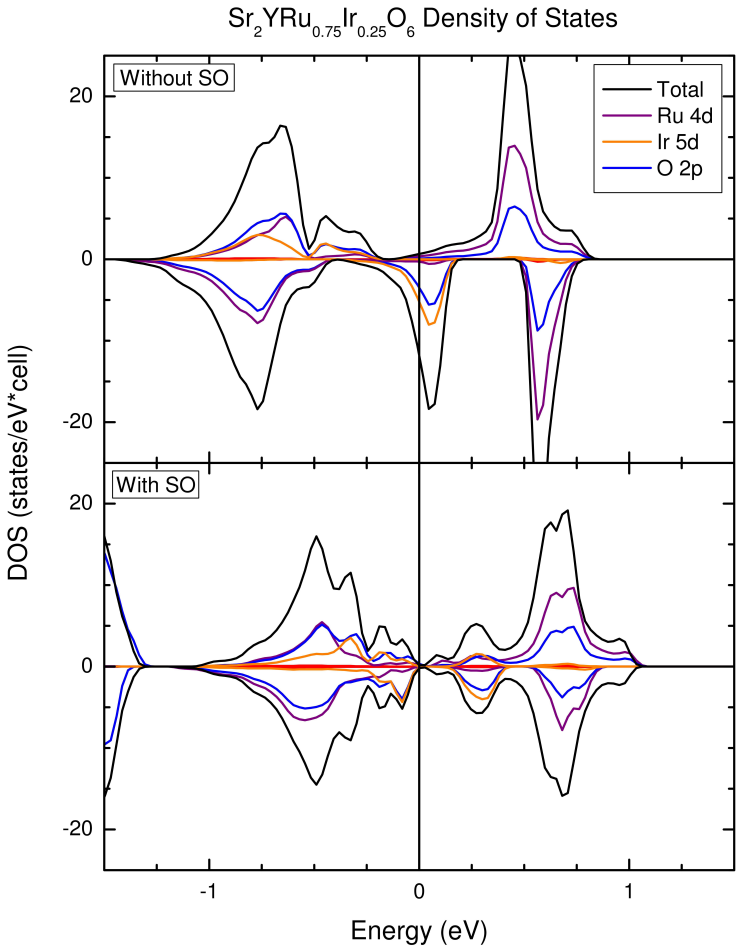

Figure 5.11 Calculated densities of states for $Sr_2YRu_{0.75}Ir_{0.25}O_6$ with and without Ir $5d$ and Ru $4d$ spin-orbit coupling. The main effect appears in the Ir $5d$ states at E_F.

Another effect of the inclusion of the SO interaction is the reduction of the magnetic moments within the IrO_6 octahedron, from $0.98\mu_B$ to $0.45\mu_B$ in Ir ions, and nearly suppressing all contribution of O ions. On the other hand, the effect on the magnetic moment within the RuO_6 octahedron is negligible, as shown in Table 5.3. The importance of SO coupling in this material is also observed in inelastic neutron scattering measurements [129]. Again, the calculated total magnetic moment regards the calculated unit cell, and it does not mean that, the samples present a macroscopic non-vanishing total magnetic moment.

The electron-doping caused by the partial substitution of Ru $4d^3$ by Ir $5d^4$ raises the question of whether this extra electron delocalizes to other sites or, if it introduces

Table 5.3: Calculated magnetic moments, in units of μ_B, of $Sr_2YRu_{0.75}Ir_{0.25}O_6$ and the effect of spin-orbit coupling.

	x = 0.25 (no SO)	x = 0.25 (SO)
μ_{Tot}	0.82	1.95
μ_{Ru}	1.63	1.65
$\mu_{O_{Ru}}$	0.10	0.10
μ_{Ir}	-0.98	-0.45
$\mu_{O_{Ir}}$	-0.10	-0.04

any orbital anisotropy. This issue can be addressed by analyzing the orbital occupancy of the Ru $4d_{xy,xz,yz}$ and Ir $5d_{xy,xz,yz}$ orbitals, which are displayed in Table 5.4. Neglecting the small deviation from the cubic perovskite structure, only these orbitals contribute to the T_{2g} molecular orbital. From the calculated data, it can be inferred that the extra electron introduced by Ir substitution is somewhat delocalized, given a smaller value than the expected nominal occupancy of $5d^4$. Further, there is no evident sign of important orbital ordering, which indicates the system is quite isotropic. It is important to note that the occupation mentioned in Ref. [42] is related to the entire Ru $4d$ band, not only the t_{2g} symmetry as it was done here. Our analysis of the entire Ru $4d$ band (not shown) yielded similar results as in Ref [42].

Table 5.4: Calculated orbital occupancies of Sr_2YRuO_6 and $Sr_2YRu_{0.75}Ir_{0.25}O_6$, and the effect of spin-orbit coupling.

	x = 0	x = 0.25 (no SO)	x = 0.25 (SO)
Ru $4d$ t_{2g}	2.90	2.98	2.94
xy_{Ru}	0.97	1.01	0.97
xz_{Ru}	0.97	0.98	1.00
yz_{Ru}	0.96	0.99	0.97
Ir $5d$ t_{2g}	–	3.64	3.41
xy_{Ir}	–	1.25	1.17
xz_{Ir}	–	1.17	1.12
yz_{Ir}	–	1.22	1.12

5.2.6 Discussion

It is known that in fcc magnetic lattices, such as the one formed by Ru^{5+} ions in Sr_2YRuO_6, next-nearest-neighbor (NNN) coupling and/or magnetic anisotropy can stabilize the magnetic order [41; 111; 112] although the latter should be much smaller than the former. The existence of ferromagnetic interactions in SYRO was inferred from band structure calculations [42] and proposed by several authors, albeit the microscopic origin of this interaction is still unclear. One hypothesis is that, either single-ion magnetic anisotropy, or anti-symmetric exchange would cant spins and induce a small FM component [40; 115; 116]. On the other hand, the recently proposed picture of a partial long-range order, where alternate AFM layers are coupled, is an indicative of sizeable FM NNN interactions [117].

The discussion of magnetic interactions is not straightforward within the DFT framework, specially in insulating systems, because it does not explicitly include the exchange interaction between localized ions. However, this method provides information on electron density and orbital occupancies, which can then be used to give insights on the magnetism of the system. The first-principles calculations reported here indicate a tilting of atomic spins away from the pseudocubic b′ axis, and towards the monoclinic b axis, consistent with neutron powder diffraction measurements. However, this deviation induces no appreciable difference among the occupancies of Ru $4d$ t_{2g}, indicating a fairly isotropic character of the molecular bonds.

Also, according to the calculations, the magnetic moment of the Ir^{5+} ion is nearly 75% smaller than in Ru^{5+}. This fact is reflected in the induced magnetization of the oxygen ions at the IrO_6 octahedron, which are 60% smaller than the ones at the RuO_6 octahedron. Hence, the reduction of T_{N1} in the Ir substituted sample can be understood in terms of the weakening of the NNN interaction due to the decrease of the magnetic moment of Ir ion at 25% of the Ru sites. Further, the suppression of T_{N2} in the same compound can be understood in terms of the weakening of the Ru–O–O–Ru interaction due to the reduction of the spin polarization in oxygen sites, which reflects the characteristic strong Ru $4d$–O $2p$ covalency in these compounds. Since no orbital ordering is found, and the SO interaction has an effect over the magnitude and orientation of the magnetic moments, the results indicate the spin-orbit interaction **could play an important role in the stabilization of the magnetic ordering in the Sr_2YRuO_6 system.**

5.3 Summary and conclusions

This part of the work reported on physical properties, spectroscopy and electronic structure of Sr_2YRuO_6 and $Sr_2YRu_{0.75}Ir_{0.25}O_6$ polycrystals. The spectroscopic methods used here were the X-ray (resonant) photoemission spectroscopy and X-ray absorption spectroscopy. The experimental results were interpreted via first-principle calculations, with and without the inclusion of spin-orbit interaction.

In the valence band region, the X-ray photoemission spectra showed the O $2p$- and Ru $4d$-derived bands, which are clearly identified by the calculated density of states (DOS). The changes in the spectra caused by Ir substitution were also captured by the calculation, as evidenced by the increase in the DOS close to E_F and at the bottom of the O $2p$ band. Furthermore, the contributions from Ru $4d$ orbitals to the valence spectra were identified with the Ru L_3 resonant photoemission technique. The difference between the on- and off-resonance spectra agreed well with the calculated Ru $4d$ DOS. The results showed that the Ru $4d$ (Ir $5d$) character appears close to the Fermi energy and is highly hybridized with O $2p$ states. Comparison of these results with previously reported RPES spectra for $SrRuO_3$ indicate that U_{Ru}^{5+} should be smaller than U_{Ru}^{4+}, which also justifies the use of the DFT approach with the GGA approximation to study this material. Finally, the unoccupied part of the O $2p$ orbitals hybridized with different metal bands were mapped with the O $1s$ XAS, and presented good agreement with the calculated O $2p$ DOS.

The analysis of the calculated ground state properties indicates that the spin-orbit interaction does not affect the Ru^{5+} ions significantly, while causing a reduction of magnetic moments of the Ir^{5+} ions. Also, this interaction does not induce orbital ordering, but it is responsible for suppressing the density of states ate the Fermi level of $Sr_2YRu_{0.75}Ir_{0.25}O_6$. Further, the reduction of T_{N1} with Ir substitution can be explained by the dilution of the magnetic moment in the $Sr_2YRu_{0.75}Ir_{0.25}O_6$ unit cell, specifically at the IrO_6 octahedra. The results indicate that the spin-orbit interaction could play an important role in this system.

6 Conclusions

This thesis presented electronic structure studies of $SrTi_{1-x}Ru_xO_3$ (x = 0, 0.1, 0.2, 0.35, 0.40, 0.50, 0.60, 0.80, 1) and $Sr_2YRu_{0.75}Ir_{0.25}O_6$ (x = 0, 0.25) by means of x-ray (resonant) photoemission and absorption spectroscopies and theoretical methods. This combined experimental + theoretical approach allowed for a thorough interpretation of the electronic structure, which can ultimately be correlated to the physical properties of the materials. The (Double) cluster model was chosen to interpret the spectra of the $SrTi_{1-x}Ru_xO_3$ series based on my previous work on $SrRuO_3$, which used the Cluster Model to study correlation and covalence effects in this material. In this case, the interest lies in identifying possible changes in the electronic structure of $SrTi_{0.5}Ru_{0.5}O_3$ arising from the interaction between the TiO_6 and RuO_6 octahedra. On the other hand, the method chosen to study the $Sr_2YRu_{1-x}Ir_xO_6$ series was the DFT for mainly two reasons: (i) the primary interest lies in ground state properties such as the magnetic moments of Ru and Ir atoms, which are correctly calculated by the DFT; (ii) the Ru^{5+} ion assumes a $4d^3$ electronic configuration in this material, which leads to less electronic correlation and enables a better comparison of XPS data with the calculated DOS.

The $SrTi_{1-x}Ru_xO_3$ series (Section 4) particularly known for its intriguing electrical properties, whose behavior range from insulating in $SrTiO_3$ to a correlated metal in $SrRuO_3$, with a insulator-to-metal transition for x $\approx$ 0.7 which is still elusive. After characterization of the ES of the $SrTi_{1-x}Ru_xO_3$ with experimental methods, the spectra of $SrTiO_3$, $SrTi_{0.5}Ru_{0.5}O_3$ and $SrRuO_3$ were interpreted with cluster models. In particular, the spectra of $SrTi_{0.5}Ru_{0.5}O_3$ were simulated with a double cluster (DC) and by properly weighing the $SrTiO_3$ and $SrRuO_3$ single cluster calculations (SC).

Although SC and DC approaches resulted in a good agreement with experiment, the analysis of the compositions of the peaks in the core level and valence band spectra with the DC and SC approaches yielded different results. The most noticeable differences are manifested in (i) the reduction of ligand screening in the DC results, which was explained in terms of the position of Ti^{4+} and Ru^{4+} ions in the ZSA diagram; and (ii) the differences in the screening mechanisms between these spectra, which indicate that, in the core level, the creation of a hole by the photoemission process decouples the Ti $3d$ and Ru $4d$ states, while the valence band hole is responsible for enhancing the mixing of the system.

One of the other materials studied (Section 5), the double perovskite Sr_2YRuO_6, can be understood as if every other Ru ion had been replaced by Y in $SrRuO_3$. This material crystallizes in a structure in which the RuO_6 and YO_6 octahedra form a three-dimensional checkerboard-like arrangement. Although magnetic interactions are thought to arise only from Ru^{5+} ions, because Y^{3+} ions present an empty $3d$ band, Sr_2YRuO_6 presents two phase transitions and other anomalous magnetic properties, are believed to stem from the face-centered-cubic (fcc) network formed by the Ru^{5+} ions. This arrangement is the simplest 3D structure leading to geometric frustrated magnetism. One possible approach to study the magnetic interactions in SYRO is to replace the Ru ion for Ir, a less magnetic atom with one extra electron in the valence band, originating the other compound studied in Section 5, $Sr_2YRu_{0.75}Ir_{0.25}O_6$. This part of the thesis focused on the interpretation of the core level and valence band XPS and O $1s$ XAS measurements of Sr_2YRuO_6 and $Sr_2YRu_{0.75}Ir_{0.25}O_6$ polycrystals using the DFT method with the a GGA exchange-correlation potential, with and without the inclusion of the spin-orbit interaction in the Ru $4d$ and Ir $5d$ orbitals.

The electronic structure of Sr_2YRuO_6 and $Sr_2YRu_{0.75}Ir_{0.25}O_6$ polycrystals were measured and characterized with X-ray Photoemission, X-ray Resonant Photoemission and X-ray Absorption spectroscopies. The calculated DOS satisfactorily reproduced the (resonant) valence band photoemission and O $1s$ x-ray absorption spectra, including the changes in the spectra caused by Ir substitution. Furthermore, comparison of the RPES measurements with previously reported RPES spectra of $SrRuO_3$ indicate that the electron correlation U_{Ru}^{3+} should be smaller than U_Ru^{4+}, which also justifies the use of the DFT approach with the GGA approximation to study this material. Analysis of the calculated ground state properties indicated that the spin-orbit interaction in Ir^{5+} ions causes a reduction of magnetic moments. This interaction is also responsible for suppressing the density of states at the Fermi level of $Sr_2YRu_{0.75}Ir_{0.25}O_6$, rendering the correct semiconducting behavior. even though it does not induce any significant orbital ordering. Further, the presented reduction of T_{N1} with Ir substitution can be explained by the dilution of the magnetic moment in the $Sr_2YRu_{0.75}Ir_{0.25}O_6$ unit cell, specifically at the IrO_6 octahedra. The results show that the canting of Ru^{5+} magnetic moments could actually play an important role in the stabilization of the magnetic ordering in the Sr_2YRuO_6 system.

The presented results highlight the relevance of a combined experimental and theoretical approach in the study of the electronic structure of transition metal compounds, which enables to not only map, but to thoroughly interpret the occupied and unoccupied states. For this purpose, synchrotron sources play a major role in the experimental front, because they are projected to generate x-rays in such a way that many (and sometimes complementary) x-ray techniques can be successfully performed. On the theoretical

front, several methods exist, in particular *ab-initio* methods, such as the DFT, and semi-empirical methods, such as the Cluster model, each of which with its limitations and advantages. Although all of them can be used to some extent, the convenient choice of the method is crucial for the interpretation of the electronic structure of any material. This choice is based not only on the materials studied, but on the X-ray spectrum to be interpreted and wheter the quantities of interest are ground state or excited state properties.

Bibliography

[1] P. Drude, Annalen der Physik **306**, 566 (1900).

[2] P. Drude, Annalen der Physik **308**, 369 (1900).

[3] A. Sommerfeld, Zeitschrift für Physik **47**, 1 (1928).

[4] F. Bloch, Zeitschrift für Physik **52**, 555 (1929).

[5] A. Sommerfeld and H. Bethe, Aufbau Der Zusammenhängenden Materie , 333 (1933).

[6] A. H. Wilson, Proceedings of the Royal Society of London A: Mathematical, Physical and Engineering Sciences **133**, 458 (1931).

[7] A. H. Wilson, Proceedings of the Royal Society of London A: Mathematical, Physical and Engineering Sciences **134**, 277 (1931).

[8] V. Fock, Zeitschrift für Physik **61**, 126 (1930).

[9] J. C. Slater, Phys. Rev. **35**, 210 (1930).

[10] Brillouin, L., J. Phys. Radium **5**, 413 (1934).

[11] D. R. Hartree and W. Hartree, Proceedings of the Royal Society of London A: Mathematical, Physical and Engineering Sciences **164**, 167 (1938).

[12] J. C. Slater, Phys. Rev. **81**, 385 (1951).

[13] P. Hohenberg and W. Kohn, Phys. Rev. **136**, B864 (1964).

[14] W. Kohn and L. J. Sham, Phys. Rev. **140**, A1133 (1965).

[15] J. H. de Boer and E. J. W. Verwey, Proceedings of the Physical Society **49**, 59 (1937).

[16] N. F. Mott and R. Peierls, Proceedings of the Physical Society **49**, 72 (1937).

[17] N. F. Mott, Proceedings of the Physical Society. Section A **62**, 416 (1949).

[18] N. F. Mott, Canadian journal of physics **34**, 1356 (1956).

[19] N. F. Mott, Philosophical Magazine **6**, 287 (1961).

[20] F. M. F. de Groot and A. Kotani, *Core Level Spectroscopy of Solids*, Advances in Condensed Matter Science (CRC Press, 2008).

[21] A. C. Thompson and D. Vaughan, *X-ray Data Booklet* (Lawrence Berkeley Laboratory, 2001).

[22] R. Eisberg and R. Resnick, *Quantum Physics of Atoms, Molecules, Solids, Nuclei, and Particles* (J. Wiley & sons, 2002).

[23] K.-I. Kobayashi, T. Kimura, H. Sawada, K. Terakura, and Y. Tokura, Nature **395**, 677 (1998).

[24] A. Callaghan, C. W. Moeller, and R. Ward, Inorganic Chemistry **5**, 1572 (1966).

[25] J. G. Bednorz and K. A. Müller, Zeitschrift für Physik B Condensed Matter **64**, 189 (1986).

[26] S. Jin, M. McCormack, T. H. Tiefel, and R. Ramesh, Journal of Applied Physics **76**, 6929 (1994).

[27] F. J. Morin, Phys. Rev. Lett. **3**, 34 (1959).

[28] H. F. Pen, M. Abbate, A. Fuijmori, Y. Tokura, H. Eisaki, S. Uchida, and G. A. Sawatzky, Phys. Rev. B **59**, 7422 (1999).

[29] D. B. McWhan, A. Menth, J. P. Remeika, W. F. Brinkman, and T. M. Rice, Phys. Rev. B **7**, 1920 (1973).

[30] S. Royer, D. Duprez, F. Can, X. Courtois, C. Batiot-Dupeyrat, S. Laassiri, and H. Alamdari, .

[31] S. Tao and J. T. S. Irvine, Nat Mater **2**, 320 (2003).

[32] M. A. Green, A. Ho-Baillie, and H. J. Snaith, Nat Photon **8**, 506 (2014).

[33] K. Momma and F. Izumi, Journal of Applied Crystallography **44**, 1272 (2011).

[34] R. J. O. Mossanek, M. Abbate, T. Yoshida, A. Fujimori, Y. Yoshida, N. Shirakawa, H. Eisaki, S. Kohno, P. T. Fonseca, and F. C. Vicentin, Phys. Rev. B **79**, 033104 (2009).

[35] E. B. Guedes, M. Abbate, K. Ishigami, A. Fujimori, K. Yoshimatsu, H. Kumigashira, M. Oshima, F. C. Vicentin, P. T. Fonseca, and R. J. O. Mossanek, Phys. Rev. B **86**, 235127 (2012).

[36] K. W. Kim, J. S. Lee, T. W. Noh, S. R. Lee, and K. Char, Phys. Rev. B **71**, 125104 (2005).

[37] K. Nogami, K. Yoshimatsu, H. Mashiko, E.Sakai, H. Kumigashira, O. Sakata, T. Oshima, and A. Ohtomo, Applied Physics Express **6**, 105502 (2013).

[38] R. Greatrex, N. N. Greenwood, M. Lal, and I. Fernandez, J. Solid State Chem. **30**, 137 (1979).

[39] P. D. Battle and W. J. Macklin, J. Solid State Chem. **145**, 138 (1984).

[40] G. Cao, Y. Xin, C. S. Alexander, and J. E. Crow, Phys. Rev. B **63**, 184432 (2001).

[41] Y.-Y. Li, Phys. Rev. **84**, 721 (1951).

[42] I. I. Mazin and D. J. Singh, Phys. Rev. B **56**, 803 (1997).

[43] J. A. van Bokhoven and C. Lamberti, *X-Ray Absorption and X-Ray Emission Spectroscopy: Theory and Applications*, v. 1 (Wiley, 2016).

[44] SXS Beamline website: `http://lnls.cnpem.br/linhas-de-luz/sxs/overview/` [accessed Jan, 2017].

[45] A. Einstein, Annalen der Physik **322**, 132 (1905).

[46] R. Schlafs, "Calibration of photoemission spectra and work function determination," `http://rsl.eng.usf.edu/Pages/Tutorials.htm` [accessed Jan, 2017].

[47] S. Hüfner, *Photoelectron Spectroscopy: Principles and Applications*, Advanced Texts in Physics (Springer, 2003).

[48] C. S. Fadley, Chemical Physics Letters **25**, 225 (1974).

[49] R. Manne and T. Aberg, Chemical Physics Letters **7**, 282 (1970).

[50] J. J. Yeh and I. Lindau, Atomic Data and Nuclear Data Tables **32**, 1 (1985).

[51] M. P. Seah and W. A. Dench, Surface and Interface Analysis **1**, 2 (1979).

[52] M. Abbate, J. B. Goedkoop, F. M. F. de Groot, M. Grioni, J. C. Fuggle, S. Hofmann, H. Petersen, and M. Sacchi, Surface and Interface Analysis **18**, 65 (1992).

[53] M. Abbate, F. C. Vicentin, V. Compagnon-Cailhol, M. C. Rocha, and H. Tolentino, Journal of Synchrotron Radiation **6**, 964 (1999).

[54] S. Tanuma, C. J. Powell, and D. R. Penn, Surface and Interface Analysis **43**, 689 (2011).

[55] PGM Beamline website: `http://lnls.cnpem.br/linhas-de-luz/pgm/overview/` [accessed Jan, 2017].

[56] J. van Elp, J. Wieland, H. Eskes, P. Kuiper, G. Sawatzky, F. de Groot, and T. Turner, Phys. Rev. B **44**, 6090 (1991).

[57] M. Imada, A. Fujimori, and Y. Tokura, Reviews of Modern Physics **70**, 1039 (1998).

[58] J. C. Slater and G. F. Koster, Phys. Rev. **94**, 1498 (1954).

[59] G. van der Laan, C. Westra, C. Haas, and G. A. Sawatzky, Phys. Rev. B **23**, 4369 (1981).

[60] A. Fujimori and F. Minami, Phys. Rev. B **30**, 957 (1984).

[61] J. Zaanen, G. A. Sawatzky, and J. W. Allen, Phys. Rev. Lett. **55**, 418 (1985).

[62] T. Mizokawa, H. Namatame, A. Fujimori, K. Akeyama, H. Kondoh, H. Kuroda, and N. Kosugi, Phys. Rev. Lett. **67**, 1638 (1991).

[63] H. Eskes, L. H. Tjeng, and G. A. Sawatzky, Phys. Rev. B **41**, 288 (1990).

[64] Z.-X. Shen, J. W. Allen, P. A. P. Lindberg, D. S. Dessau, B. O. Wells, A. Borg, W. Ellis, J. S. Kang, S.-J. Oh, I. Lindau, and W. E. Spicer, Phys. Rev. B **42**, 1817 (1990).

[65] J. Ghijsen, L. H. Tjeng, J. van Elp, H. Eskes, J. Westerink, G. A. Sawatzky, and M. T. Czyzyk, Phys. Rev. B **38**, 11322 (1988).

[66] A. E. Bocquet, T. Mizokawa, T. Saitoh, H. Namatame, and A. Fujimori, Phys. Rev. B **46**, 3771 (1992).

[67] M. Taguchi, A. Chainani, N. Kamakura, K. Horiba, Y. Takata, M. Yabashi, K. Tamasaku, Y. Nishino, D. Miwa, T. Ishikawa, S. Shin, E. Ikenaga, T. Yokoya, K. Kobayashi, T. Mochiku, K. Hirata, and K. Motoya, Phys. Rev. B **71**, 155102 (2005).

[68] R. Mossanek and M. Abbate, Phys. Rev. B **74**, 125112 (2006).

[69] A. E. Bocquet, T. Mizokawa, K. Morikawa, A. Fujimori, S. R. Barman, K. Maiti, D. D. Sarma, Y. Tokura, and M. Onoda, Phys. Rev. B **53**, 1161 (1996).

[70] R. J. O. Mossanek, I. Preda, M. Abbate, J. Rubio-Zuazo, G. R. Castro, A. Vollmer, A. Gutiérrez, and L. Soriano, Chem. Phys. Lett. **501**, 437 (2011).

[71] R. M. Martin, *Electronic Structure: Basic Theory and Practical Methods* (Cambridge University Press, 2004).

[72] F. Tran and P. Blaha, Phys. Rev. Lett. **102**, 226401 (2009).

[73] V. I. Anisimov, I. V. Solovyev, M. A. Korotin, M. T. Czyżyk, and G. A. Sawatzky, Phys. Rev. B **48**, 16929 (1993).

[74] A. I. Liechtenstein, V. I. Anisimov, and J. Zaanen, Phys. Rev. B **52**, R5467 (1995).

[75] P. Blaha, K. Schwarz, G. Madsen, D. Kvasnicka, and J. Luitz, *WIEN2K: An Augmented Plane Wave + Local Orbitals Program for Calculating Crystal Properties* (2014) pp. 1–223.

[76] G. K. H. Madsen, P. Blaha, K. Schwarz, E. Sjöstedt, and L. Nordström, Phys. Rev. B **64**, 195134 (2001).

[77] J. C. Slater, Phys. Rev. **51**, 846 (1937).

[78] D. Singh, *Planewaves, Pseudopotentials and the LAPW Method* (Springer US, 2013).

[79] F. W. Lytle, Journal of Applied Physics **35**, 2212 (1964).

[80] K. van Benthem, C. ElsÄsser, and R. H. French, Journal of Applied Physics **90**, 6156 (2001).

[81] P. B. Allen, H. Berger, O. Chauvet, L. Forro, T. Jarlborg, A. Junod, B. Revaz, and G. Santi, Phys. Rev. B **53**, 4393 (1996).

[82] A. P. Mackenzie, J. W. Reiner, A. W. Tyler, L. M. Galvin, S. R. Julian, M. R. Beasley, T. H. Geballe, and A. Kapitulnik, Phys. Rev. B **58**, R13318 (1998).

[83] P. Kostic, Y. Okada, N. C. Collins, Z. Schlesinger, J. W. Reiner, L. Klein, A. Kapitulnik, T. H. Geballe, and M. R. Beasley, Phys. Rev. Lett. **81**, 2498 (1998).

[84] L. Klein, J. S. Dodge, C. H. Ahn, G. J. Snyder, T. H. Geballe, M. R. Beasley, and A. Kapitulnik, Phys. Rev. Lett. **77**, 2774 (1996).

[85] S. A. Chambers, T. Droubay, T. C. Kaspar, M. Gutowski, and M. van Schilfgaarde, Surface Science **554**, 81 (2004).

[86] L. Soriano, M. Abbate, A. Fernández, A. R. González-Elipe, and J. M. Sanz, Surface and Interface Analysis **25**, 804 (1997).

[87] J. Okamoto, T. Mizokawa, A. Fujimori, I. Hase, M. Nohara, H. Takagi, Y. Takeda, and M. Takano, Phys. Rev. B **60**, 2281 (1999).

[88] J. Kim, J. Chung, and S.-J. Oh, Phys. Rev. B **71**, 121406 (2005).

[89] M. Takizawa, D. Toyota, H. Wadati, A. Chikamatsu, H. Kumigashira, A. Fujimori, M. Oshima, Z. Fang, M. Lippmaa, M. Kawasaki, and H. Koinuma, Phys. Rev. B **72**, 060404 (2005).

[90] K. Fujioka, J. Okamoto, T. Mizokawa, A. Fujimori, I. Hase, M. Abbate, H. J. Lin, C. T. Chen, Y. Takeda, and M. Takano, Phys. Rev. B **56**, 6380 (1997).

[91] J. Park, S.-J. Oh, J.-H. Park, D. M. Kim, and C.-B. Eom, Phys. Rev. B **69**, 085108 (2004).

[92] K. Maiti, Phys. Rev. B **73**, 235110 (2006).

[93] J. M. Rondinelli, N. M. Caffrey, S. Sanvito, and N. A. Spaldin, Phys. Rev. B **78**, 155107 (2008).

[94] H.-T. Jeng, S.-H. Lin, and C.-S. Hsue, Phys. Rev. Lett. **97**, 067002 (2006).

[95] H. Hadipour and M. Akhavan, Journal of Solid State Chemistry **183**, 1678 (2010).

[96] H.-D. Kim, H.-J. Noh, K. H. Kim, and S.-J. Oh, Phys. Rev. Lett. **93**, 126404 (2004).

[97] E. Jakobi, S. Kanungo, S. Sarkar, S. Schmitt, and T. Saha-Dasgupta, Phys. Rev. B **83**, 041103 (2011).

[98] M. Abbate, J. A. Guevara, S. L. Cuffini, Y. P. Mascarenhas, and E. Morikawa, Eur. Phys. J. B **25**, 203 (2002).

[99] J. Kim, J.-Y. Kim, B.-G. Park, and S.-J. Oh, Phys. Rev. B **73**, 235109 (2006).

[100] K. Maiti, Phys. Rev. B **77**, 212407 (2008).

[101] P.-A. Lin, H.-T. Jeng, and C.-S. Hsue, Phys. Rev. B **77**, 085118 (2008).

[102] B. H. Toby, Journal of Applied Crystallography **34**, 210 (2001).

[103] A. C. Larson and R. B. von Dreele, General Structure Analysis System (GSAS), Los Alamos, NM: Los Alamos National Laboratory; 2004. Report No. LAUR 86-748 .

[104] L. Soriano, M. Sánchez-Agudo, R. J. O. Mossanek, M. Abbate, G. G. Fuentes, P. R. Bressler, L. Alvarez, J. Méndez, A. Gutiérrez, and J. M. Sanz, Surface Science **605**, 539 (2011).

[105] C. Guillot, Y. Ballu, J. Paigné, J. Lecante, K. P. Jain, P. Thiry, R. Pinchaux, Y. Pétroff, and L. M. Falicov, Phys. Rev. Lett. **39**, 1632 (1977).

[106] R. Mossanek, M. Abbate, T. Yoshida, A. Fujimori, Y. Yoshida, N. Shirakawa, H. Eisaki, S. Kohno, and F. Vicentin, Phys. Rev. B **78**, 075103 (2008).

[107] R. Eguchi, M. Taguchi, M. Matsunami, K. Horiba, K. Yamamoto, Y. Ishida, A. Chainani, Y. Takata, M. Yabashi, D. Miwa, Y. Nishino, K. Tamasaku, T. Ishikawa, Y. Senba, H. Ohashi, Y. Muraoka, Z. Hiroi, and S. Shin, Phys. Rev. B **78**, 075115 (2008).

[108] R. J. O. Mossanek and M. Abbate, Journal of Physics: Condensed Matter **22**, 375602 (2010).

[109] E. B. Guedes, M. Abbate, F. Abud, R. F. Jardim, F. C. Vicentin, and R. J. O. Mossanek, Phys. Rev. B **94**, 045109 (2016).

[110] P. C. Donohue and E. L. McCann, Mater. Res. Bull. **12**, 519 (1977).

[111] E. V. Kuzmin, S. G. Ovchinnikov, and D. J. Singh, Phys. Rev. B **68**, 024409 (2003).

[112] E. V. Kuzmin, S. G. Ovchinnikov, and D. J. Singh, JETP **96**, 1124 (2003).

[113] I. Dzyaloshinsky, Journal of Physics and Chemistry of Solids **4**, 241 (1958).

[114] T. Moriya, Phys. Rev. **120**, 91 (1960).

[115] R. P. Singh and C. V. Tomy, Phys. Rev. B **78**, 024432 (2008).

[116] P. L. Bernardo, L. Ghivelder, G. G. Eslava, H. S. Amorim, E. H. C. Sinnecker, I. Felner, J. J. Neumeier, and S. García, J. Phys. Condens. Matter **24**, 486001 (2012).

[117] E. Granado, J. W. Lynn, R. F. Jardim, and M. S. Torikachvili, Phys. Rev. Lett. **110**, 017202 (2013).

[118] A. F. García-Flores, H. Terashita, E. M. Bittar, R. F. Jardim, and E. Granado, Journal of Raman Spectroscopy **45**, 193 (2014).

[119] H. A. Blackstead, J. D. Dow, D. R. Harshman, W. B. Yelon, M. X. Chen, M. K. Wu, D. Y. Chen, F. Z. Chien, and D. B. Pulling, Phys. Rev. B **63**, 214412 (2001).

[120] S. Rao, J. Srivastava, M. Wu, B. Mok, C. Chen, M. Ling, H.-L. Liu, Y. Chen, and J. Ho, J. Supercond. Nov. Magn. **24**, 1249 (2011).

[121] R. D. Shannon, Acta Crystallographica Section A **32**, 751 (1976).

[122] M. H. Aguirre, D. Logvinovich, L. Bocher, R. Robert, S. G. Ebbinghaus, and A. Weidenkaff, Acta Materialia **57**, 108 (2009).

[123] M. Wakeshima, D. Harada, and Y. Hinatsu, Journal of Alloys and Compounds **287**, 130 (1999).

[124] G. Cao, T. F. Qi, L. Li, J. Terzic, S. J. Yuan, L. E. DeLong, G. Murthy, and R. K. Kaul, Phys. Rev. Lett. **112**, 056402 (2014).

[125] M. T. Anderson, K. B. Greenwood, G. A. Taylor, and K. R. Poeppelmeier, Progress in Solid State Chemistry **22**, 197 (1993).

[126] J. P. Perdew, A. Ruzsinszky, G. I. Csonka, O. A. Vydrov, G. E. Scuseria, L. A. Constantin, X. Zhou, and K. Burke, Phys. Rev. Lett. **100**, 136406 (2008).

[127] B. J. Kim, H. Jin, S. J. Moon, J.-Y. Kim, B.-G. Park, C. S. Leem, J. Yu, T. W. Noh, C. Kim, S.-J. Oh, J.-H. Park, V. Durairaj, G. Cao, and E. Rotenberg, Phys. Rev. Lett. **101**, 076402 (2008).

[128] S. Y. Jang, H. Kim, S. J. Moon, W. S. Choi, B. C. Jeon, J. Yu, and T. W. Noh, J. Phys. Condens. Matter **22**, 485602 (2010).

[129] S. M. Disseler, J. W. Lynn, R. F. Jardim, M. S. Torikachvili, and E. Granado, Phys. Rev. B **93**, 140407 (2016).

[130] Y. T. Satoru Sugano and H. K. (Eds.), *Multiplets of Transition-Metal Ions in Crystals*, 0th ed., Pure and Applied Physics 33 (Academic Press Inc, 1970).

[131] G. Arfken and H. Weber, *Mathematical Methods for Physicists* (Elsevier Science).

[132] H. Bruus and K. Flensberg, *Many-Body Quantum Theory in Condensed Matter Physics: An Introduction*, Oxford Graduate Texts (OUP Oxford, 2004).

Appendices

A The Crystal Field Splitting

The crystal Field Theory [130] describes the splitting of otherwise degenerate electronic orbitals under the influence of a surrounding static point charge distribution provided by the anion neighbors, with a defined symmetry. For this purpose, we are interested in finding the eigenvalues of Schrödinger's equation to the following Hamiltonian:

$$\hat{H} = \hat{H}_0 + \hat{H}_{CF}, \tag{A.1}$$

where the term $\hat{H}_0$ includes the kinetic energy of the electrons and their interaction with the nuclei is constant and can be omitted. The term $\hat{H}_{CF}$ describes the interaction among the electrons and the crystal field due to the anion neighbors. The spin-orbit interaction in 3,4d orbitals is of the order of 0.01 eV, and can be disregarded in face of typical crystal fields of a few eV for these orbitals.

Let us consider a crystal with perovskite-like structure, such as in Fig. 1.4, where a transition metal with a single valence electron is surrounded by a regular octahedron of oxygen anions (O_h symmetry). This is true In most cases, except where effects such as the Jahn-Teller distortion are severe. The regular octahedron considered is depicted in Fig. A.1; the transition metal is at the origin, and the oxygen ions with charges Q are located at ($\pm a$, 0, 0), (0, $\pm a$, 0) e (0, 0, $\pm a$), where a defines the dimensions of the octahedron.

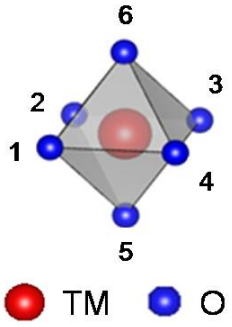

Figure A.1 Transition metal ion arranged in the center of a octahedra of point charges (oxygen anions), in O_h symmetry.

Hence, $\hat{H}_{CF}$ can be written as:

$$\hat{H}_{CF}(\vec{r}) = \sum_{i=1}^{6} \frac{Qe}{|\vec{R}_i - \vec{r}|} \tag{A.2}$$

where $\vec{r}$ and $\vec{R}_i$ are the electron and point charges positions, respectively. $\hat{H}_{CF}$ can be further expanded in terms of Legendre Polynomials:

$$\hat{H}_{CF}(\vec{r}) = Qe\sum_{i=1}^{6}\sum_{k=0}^{\infty}\frac{r_<^k}{r_>^{k+1}}P_k(cos\gamma_i) \tag{A.3}$$

where $r_<$ and $r_>$ are the largest and smallest values between a and r, and γ is the angle between $\vec{R}_i$ and $\vec{r}$. Due to he strong spacial localization of the d orbitals, we may assume $r_< = r$ e $r_> = a$. Hence,

$$\hat{H}_{CF}(\vec{r}) = Qe\sum_{i=1}^{6}\sum_{k=0}^{\infty}\frac{r^k}{a^{k+1}}P_k(cos\gamma_i). \tag{A.4}$$

The Spherical Harmonic Addition theorem states that, for two unit vectors $\hat{\boldsymbol{r}}$ and $\hat{\boldsymbol{R}}_i$ with coordinates (θ, ϕ) and (θ_i', ϕ_i'), respectively, the following holds:

$$P_l(\hat{r}\cdot\hat{R}_i = cos\gamma_i) = \frac{4\pi}{2l+1}\sum_{m=-l}^{l}Y_{lm}^*(\theta_i', \phi_i')Y_{lm}(\theta, \phi) \tag{A.5}$$

Substituting equation A.5 in A.4,

$$H_{CF}(\vec{r}) = \sum_{l=0}^{\infty}\sum_{m=-l}^{l}r^k q_{l,m}C_m^{(l)}(\theta, \phi) \tag{A.6}$$

where

$$q_{lm} = \left(\frac{4\pi}{2l+1}\right)^{1/2}\frac{Qe}{a^{l+1}}\sum_{i=1}^{6}Y_{lm}^*(\theta_i', \phi_i') \tag{A.7}$$

and

$$C_m^{(l)} = \left(\frac{4\pi}{2l+1}\right)^{1/2}Y_{lm}(\theta, \phi), \tag{A.8}$$

where the pairs of angles $(\theta_i, \phi_i)\, i = 1, 2, ..., 6$, to be used in equation A.7 are:

$$(\frac{\pi}{2}, 0), (\frac{\pi}{2}, \frac{\pi}{2}), (\frac{\pi}{2}, \pi), (\frac{\pi}{2}, \frac{3\pi}{2}), (\pi, 0), (0, 0) \tag{A.9}$$

The $C_0^{(0)}$ term can be ignored for being constant (because $Y_{00}(\theta, \phi)$ is constant). The explicit forms of $Y_{4m}(\theta, \phi)\ -4 \leq m \leq 4$ can be easily found on textbooks such as [131], which combined with A.9 into A.7 causes all terms containing $m = odd$ and the terms with $m = 2$ vanish. Also, in the case of $4d$-electrons $\ell = 2$, and all terms with $k > 4$ can be ignored here, because the Clebsch-Gordan coefficients which will appear later vanish if $k > \ell_1 + \ell_2 = 4$. Then, $\hat{H}_{CF}$ can be written as:

$$\hat{H}_{CF} = \frac{7}{2}\frac{Qe}{a^5}r^4\left[C_0^{(4)} + \sqrt{\frac{5}{14}}(C_{-4}^{(4)} + C_4^{(4)})\right], \tag{A.10}$$

also known as a *cubic crystal field*.

The Crystal Field theory also assumes hydrogen-like wave functions to the atomic orbitals, which can then be written as a product of a radial $R_{nl}(r)$ and an angular $Y_{lm}(\theta,\phi)$ part,

$$\Psi_{nlm} = R_{nl}(r)Y_{lm}(\theta,\phi) \tag{A.11}$$

where $n = 0, 1, ...,\ l = 0, 1, ..., n-1$ and $m = -l, ..., l$. For the case of $4d$ electrons, for instance, $l_1 = l_2 = 2$ and $-l \leq m \leq l$. Now the matrix elements of $\hat{H}_{CC}$ can be found:

$$\langle \Psi_1 | \hat{H}_{CF} | \Psi_2 \rangle = \int \Psi^*_{n_1 l_1 m_1 s}\, \hat{H}_{CF}\, \Psi_{n_2 l_2 m_2 s}\, d^3r. \tag{A.12}$$

Substituting A.11 and A.6 into A.12 yields:

$$\begin{aligned}\langle \Psi_{n_1 l_1 m_1} | \hat{H}_{CF} | \Psi_{n_2 l_2 m_2} \rangle = \frac{7}{2}\frac{Qe}{a^5} \int_0^{2\pi} d\phi \int_0^{\pi} sin\theta d\theta \int_0^{\infty} R_{n1}(r) R_{n2}(r)\, r^6\, dr \times \\ \times Y^*_{l_1 m_1}(\theta,\phi) \left\{ C_0^{(4)} + \sqrt{\frac{5}{14}} \left(C_{-4}^{(4)} + C_4^{(4)} \right) \right\} Y_{l_2 m_2}(\theta,\phi).\end{aligned} \tag{A.13}$$

The radial part of the integral can be regarded as $\langle r^4 \rangle_{4d}$ for the present discussion. Recalling that the $\mathrm{C}_m^{(l)}$ coefficients are written in terms of $\mathrm{Y}_{lm}(\theta,\phi)$, the angular integrals of three spherical harmonics are dealt with using the following relation:

$$\int_0^{2\pi} d\phi \int_0^{\pi} sin\theta d\theta\, Y^*_{l_1 m_1}(\theta,\phi)\, Y_{lm}(\theta,\phi)\, Y_{l_2 m_2}(\theta,\phi) = \sqrt{\frac{(2l_1+1)(2l_2+1)}{4\pi(2l+1)}} C^{l0}_{l_1 0 l_2 0}\, C^{l_1 m_1}_{l_2 m_2 l m} \tag{A.14}$$

where $C^{l_1 m_1}_{l_2 m_2 l m}$ are the Clebsch-Jordan (CB) coefficients:

$$C^{l_1 m_1}_{l_2 m_2 l m} = \langle l_1 m_1 l_2 m_2 | l m \rangle, \tag{A.15}$$

with $l_1 = l_2 = 2$ and $-2 \leq m_1,\ m_2 \leq 2$.

And the expression for the matrix elements reduces to:

$$\langle \Psi_{42m_1} | \hat{H}_{CF} | \Psi_{42m_2} \rangle = C^{20}_{4020} \left[C^{2m_1}_{402m_2} + \sqrt{\frac{5}{14}} \left(C^{2m_1}_{4-42m_2} + C^{2m_1}_{442m_2} \right) \right] \tag{A.16}$$

The constant term $\mathrm{C}^{20}_{2020} = \sqrt{2/7}$, and the CB coefficients are nonvanishing for m_1 and m_2 satisfying $m_1 = 4 + m_2$, $m_1 = -4 + m_2$ and $m_1 = m_2$. The resulting matrices elements are, therefore:

$$\begin{aligned}\langle \Psi_{320} | \hat{H}'_{CC} | \Psi_{320} \rangle &= +6Dq \\ \langle \Psi_{32\pm1} | \hat{H}'_{CC} | \Psi_{32\pm1} \rangle &= -4Dq \\ \langle \Psi_{32\pm2} | \hat{H}'_{CC} | \Psi_{32\pm2} \rangle &= +Dq \\ \langle \Psi_{32\pm2} | \hat{H}'_{CC} | \Psi_{32\mp2} \rangle &= +5Dq,\end{aligned} \tag{A.17}$$

where

$$D = \frac{35}{4}\frac{Qe}{a^5} \tag{A.18}$$

$$q = \frac{2}{105}\langle r^4 \rangle_{4d}. \tag{A.19}$$

Note that D depends only on the ligand ions, whereas q depends only on properties of the transition metal ion. The splitting of the d levels of the transition metal ion under an octahedral crystal field can be obtained diagonalizing the following matrix:

$$\hat{H}'_{CF} \doteq \begin{pmatrix} Dq & 0 & 0 & 0 & 5Dq \\ 0 & -4Dq & 0 & 0 & 0 \\ 0 & 0 & 6Dq & 0 & 0 \\ 0 & 0 & 0 & -4Dq & 0 \\ 5Dq & 0 & 0 & 0 & Dq \end{pmatrix}. \tag{A.20}$$

This process results in two degenerate eigenvectors with energy $+6Dq$:

$$\begin{aligned} |\Psi_{420}\rangle &= |4d_{z^2}\rangle \\ \frac{1}{\sqrt{2}}(|\Psi_{422}\rangle + |\Psi_{42-2}\rangle) &= |4d_{x^2-y^2}\rangle, \end{aligned} \tag{A.21}$$

and in other three degenerate eigenvectors with energy $-4Dq$:

$$\begin{aligned} \frac{i}{\sqrt{2}}(|\Psi_{422}\rangle - |\Psi_{42-2}\rangle) &= |4d_{xy}\rangle \\ \frac{1}{\sqrt{2}}(|\Psi_{421}\rangle - |\Psi_{42-1}\rangle) &= |4d_{xz}\rangle \\ \frac{i}{\sqrt{2}}(|\Psi_{421}\rangle + |\Psi_{42-1}\rangle) &= |4d_{yz}\rangle. \end{aligned} \tag{A.22}$$

Such eigenvectors give rise to the so-called doubly degenerate e_g and triply degenerate t_{2g} orbitals, which are energetically split by 10 Dq, as can be seen in Figure 3.2.

B Second Quantization

B.1 Brief Review

Quantum many-body problems, such as the VES in Section 2.2 can be conveniently formulated in the Second Quantization formalism [132]. In this scheme, it is firstly necessary to choose an ordered (orthonormal) single-particle basis set in a Hilbert space ε_1, *e.g.* the energy eigenstates $|n\rangle$ of the one-dimensional quantum harmonic oscillator, which will be denoted by $|\nu_i\rangle$. N-particle states in Second Quantization are obtained by listing the the number of particles occupying each of the single-particle $|\nu_i\rangle$ states (in the case of fermions, either 0 or 1), which justifies the expression Occupation Number representation also used to denote this formalism. N-particle states are written as

$$|n_{\nu_1}, n_{\nu_2}, ..., n_{\nu_{dim\varepsilon_1}}\rangle\,, \quad \sum_i n_{\nu_i} = N, \tag{B.1}$$

and reside in a *Fock space*, which is composed of the direct sum of a set of single-particle Hilbert spaces representing zero particle states, one particle states, two particle states, and so on. It is therefore natural to define the action of operators that create ($\hat{d}^\dagger_\nu$), annihilate ($\hat{d}_\nu$) and count the number of particles ($\hat{n}_\nu$) occupying each $|\nu_i\rangle$ single-particle state $|\nu_i\rangle$:

$$\begin{array}{ccc} \hat{d}^\dagger_\nu\,|0\rangle = |\nu\rangle & \hat{d}_\nu\,|0\rangle = 0 & \hat{n}_\nu\,|0\rangle = 0 \\ \hat{d}^\dagger_\nu\,|\nu\rangle = 0 & \hat{d}_\nu\,|\nu\rangle = |0\rangle & \hat{n}_\nu\,|\nu\rangle = 1\,|\nu\rangle \end{array} \tag{B.2}$$

where $\hat{n}_\nu = \hat{d}^\dagger_\nu \hat{d}_\nu$. The fermionic creation and annihilation operator obey the following anti-commutation relations:

$$\left\{\hat{d}^\dagger_\nu, \hat{d}_{\nu'}\right\} = \delta_{\nu,\nu'} \tag{B.3}$$

$$\left\{\hat{d}_\nu, \hat{d}_{\nu'}\right\} = \left\{\hat{d}^\dagger_\nu, \hat{d}^\dagger_{\nu'}\right\} = 0, \tag{B.4}$$

$$\tag{B.5}$$

and the following commutation relations:

$$\left[\hat{d}_\nu, \hat{n}_{\nu'}\right] = \hat{d}^\dagger_\nu \delta_{\nu,\nu'} \tag{B.6}$$

$$\left[\hat{d}^\dagger_\nu, \hat{n}_{\nu'}\right] = -\hat{d}_\nu \delta_{\nu,\nu'} \tag{B.7}$$

$$[\hat{n}_\nu, \hat{n}_{\nu'}] = 0. \tag{B.8}$$

$$\tag{B.9}$$

These relations, with the addition of the requirement that the N-particle state be constructed in the same order as the single-particle basis is given, *i.e.*,

$$|1_{nu_1}, 1_{\nu_2}, ..., 1_{\nu_4}\rangle = \hat{d}^\dagger_{\nu_1}\hat{d}^\dagger_{\nu_2}\hat{d}^\dagger_{\nu_4}|0\rangle\,, \tag{B.10}$$

where $|0\rangle$ is the vacuum level, grants the condition of antisymmetrization required by the wave function of fermions.

In Second Quantization, one- and two-body operators are be expressed in terms of the creation and annihilation operators as shown in equations B.11 and B.13, respectively. For the one-body operator, the First Quantization version (on the left-hand side) acts on all i particles, while in Second Quantization (right-hand side), the sums are over an orthonormal basis of ε_1:

$$\sum_i^N \mathcal{O}_i = \sum_\nu^{dim\varepsilon_1}\sum_{\nu'}^{dim\varepsilon_1} \langle\nu|\,\mathcal{O}\,|\nu'\rangle\,\hat{d}^\dagger_\nu\hat{d}_{\nu'}. \tag{B.11}$$

The term $\langle\nu|\,\mathcal{O}\,|\nu'\rangle$ is a single-particle matrix element of operator $\mathcal{O}$,

$$\langle\nu|\,\mathcal{O}\,|\nu'\rangle = \int_V d\boldsymbol{r}\;\phi^*_\nu(\boldsymbol{r})\,\mathcal{O}\,\phi_{\nu'}(\boldsymbol{r}) \tag{B.12}$$

which can be, for instance, the kinetic energy operator. Interactions between particles are represented by two-body operators, written as:

$$\frac{1}{2}\sum_i^N\sum_{j\neq i}^N \mathcal{O}_{i,j} = \frac{1}{2}\sum_{\nu,\nu',\mu,\mu'}^{dim\varepsilon_1} \langle\nu\nu'|\,\mathcal{O}_{1,2}\,|\mu\mu'\rangle\,\hat{d}^\dagger_\nu\hat{d}^\dagger_{\nu'}\hat{d}_{\mu'}\hat{d}_\mu, \tag{B.13}$$

where $\langle\nu\nu'|\,\mathcal{O}_{1,2}\,|\mu\mu'\rangle$ are two-body matrix elements which, in the case of the Coulomb repulsion, are given by:

$$\langle\nu\nu'|\,\mathcal{O}_{1,2}\,|\mu\mu'\rangle = \int_V d\boldsymbol{r_1}\int_V d\boldsymbol{r_2}\;\frac{\phi^*_\nu(\boldsymbol{r_1})\phi^*_{\nu'}(\boldsymbol{r_2})\phi_\mu(\boldsymbol{r_1})\phi_{\mu'}(\boldsymbol{r_2})}{|\boldsymbol{r_1}-\boldsymbol{r_2}|} \tag{B.14}$$

in which the single-particle wave functions $\phi_\nu(\boldsymbol{r})$, related to the single-particle states $|\nu\rangle$ are defined in the volume V. Operators in Second Quantization are thus composed of linear combinations of products of creation and annihilation operators weighted by the appropriate matrix elements of the operator calculated in First Quantization. Note the order of the indices, which is extremely important in the case of two-particle fermion operators. The initial state is annihilated by first annihilating state μ and then state $\mu\prime$, while the final state is created by first creating state ν' and then state ν. Non-interacting systems are ruled by Hamiltonians that can be reduced to one-body operators. For interacting systems, however, two-body terms are present in $\hat{H}$, which makes impossible to, in general,analytically find its eigenstates and energies without approximations.

B.2 The Spectral Function $A(\omega)$

The Green's function formalism can be extended to the treat many-body problems in Second Quantization. In this framework, the one-particle Green's functions for a possibly interacting Hamiltonian, in contact with reservoir at temperature T and chemical potential $\bar{\mu}$, denoted by $G^R_{\mu\nu}(t-t'), G^A_{\mu\nu}(t-t'), G^>_{\mu\nu}(t-t'), G^<_{\mu\nu}(t-t')$, can be defined. For the present case only the *retarded* and *minor* Green's functions $G^R_{\mu\nu}(t-t')$ and $G^<_{\mu\nu}(t-t')$, respectively, are necessary:

$$G^R_{\mu\nu}(t-t') \equiv -\frac{i}{\hbar}\Theta(t-t')\left\langle\left\{\hat{d}^\dagger_\nu(t'), \hat{d}_\mu(t)\right\}\right\rangle \tag{B.15}$$

$$G^<_{\mu\nu}(t-t') \equiv \frac{i}{\hbar}\left\langle\hat{d}^\dagger_\nu(t')\hat{d}_\mu(t)\right\rangle. \tag{B.16}$$

In which

$$\hat{\mathcal{O}}(t) = e^{i\hat{H}t/\hbar}\hat{\mathcal{O}}e^{-i\hat{H}t/\hbar}, \tag{B.17}$$

is the Interaction Picture representation of the operator $\hat{\mathcal{O}}$, and

$$\langle\hat{\mathcal{O}}\rangle = Tr\left\{\frac{e^{-\beta(\hat{H}-\bar{\mu}\hat{N})}}{\mathcal{Z}}\hat{\mathcal{O}}\right\} \tag{B.18}$$

is the thermodynamic average on grand-canonical ensemble: $\mathcal{Z}$ is the grand-canonical partition function, with $\beta = 1/k_BT$ and k_B is the Boltzmann constant. The trace operation is performed between eigenstates of $\hat{H}$ with one particle, two particles, and so on, spanning the entire Fock space.

The function $G^<_{\mu\nu}(t-t')$ may be interpreted as the probability amplitude of a hole created in state μ at time t being observed in state ν at time t', while $G^R_{\mu\nu}(t-t')$ involves the creation and propagation of electrons and holes.

Now let us calculate equation B.15 (with t' set to 0) in the many-particle basis set of eigenstates of $\hat{H}$, denoted by $\{|n\rangle\}$. Using the definition B.17 and inserting a complete set of $|n\rangle$ between the operators,

$$G^R_{\mu\nu}(t) = -\frac{i}{\hbar}\Theta(t)\sum_n B_n \langle n|\, \hat{d}_\nu(t)\hat{d}^\dagger_\nu + \hat{d}^\dagger_\nu\hat{d}_\mu(t)\,|n\rangle \tag{B.19}$$

Substituting the operators defined in B.17 and inserting a complete set of eigenstates of $\hat{H}$,

$$\begin{aligned} G^R_{\mu\nu}(t) = -\frac{i}{\hbar}\Theta(t)\sum_{nn'} B_n\{&\langle n|\, \hat{d}_\nu\,|n'\rangle\,\langle n'|\,\hat{d}^\dagger_\nu\,|n\rangle\, e^{i(E_n-E_{n'})t/\hbar} + \\ &+ \langle n|\,\hat{d}^\dagger_\nu\,|n'\rangle\,\langle n'|\,\hat{d}_\mu\,|n\rangle\, e^{-i(E_n-E_{n'})t/\hbar}\} \end{aligned} \tag{B.20}$$

The dummy indexes can be exchanged in the second term, $n \leftrightarrow n'$, and the frequencies $\omega_n \equiv E_n/\hbar$ are used, resulting in:

$$G^R_{\mu\nu}(t) = -\frac{i}{\hbar}\Theta(t)\sum_{nn'}(B_n + B_{n'})\left\{\langle n|\,\hat{d}_\nu\,|n'\rangle\,\langle n'|\,\hat{d}^\dagger_\nu\,|n\rangle\,e^{-i(\omega_n-\omega_{n'})t}\right\}. \tag{B.21}$$

Applying the Fourier transform[1] to the above expression and using the left-hand-side equality of the following identity:

$$\int_0^\infty e^{i\omega t}dt = \lim_{\delta\to 0}\frac{i}{\omega + i\delta} = \pi\delta(\omega) + iP\left(\frac{1}{\omega}\right), \tag{B.22}$$

where P is the Principal Cauchy value, we arrive at the Lehmann representation of $G^R_{\mu\nu}(\omega)$:

$$G^R_{\mu\nu}(\omega) = \sum_{n,n'}(B_\nu + B_{\nu'})\frac{\langle n|\,\hat{d}_\mu\,|n'\rangle\,\langle n'|\,\hat{d}^\dagger_\nu\,|n\rangle}{\hbar(\omega + \omega_n - \omega_{n'}) + i\delta} \tag{B.23}$$

where δ is assumed to be close to zero. Similarly for $G^<_{\mu\nu}(\omega)$, but using the following identity instead:

$$\int_{-\infty}^\infty e^{i\omega t}dt = 2\pi\delta(\omega), \tag{B.24}$$

we can write a similar expression for $G^<_{\mu\nu}(\omega)$:

$$G^<_{\mu\nu}(\omega) = 2\pi i\sum_{n,n'}B_{\nu'}\,\langle n|\,\hat{d}_\mu\,|n'\rangle\,\langle n'|\,\hat{d}^\dagger_\nu\,|n\rangle\,\delta(\hbar\omega + \hbar\omega_n - \hbar\omega_{n'}). \tag{B.25}$$

This approach can be used to calculate the $G^A_{\mu\nu}(t-t')$ and $G^>_{\mu\nu}(t-t')$ Green's functions as well, whose diagonal parts ($\mu = \nu = \alpha$) are all intimately related and can be obtained from a single object, the so-called *Spectral Function* $A_\alpha(\omega)$, defined as:

$$A_\alpha(\omega) \equiv -2\Im m\left\{G^R_{\alpha\alpha}(\omega)\right\} \tag{B.26}$$

$A_\alpha(\omega)$ is a positive definite function, with dimension of inverse energy, normalized to $2\pi/\hbar$ and that behaves as a distribution function. Using the right-hand side of equation B.22 to rewrite $G^R_{\mu\nu}(\omega)$ as

$$\begin{aligned} G^R_{\alpha\alpha}(\omega) = &\sum_{n,n'}(B_\nu + B_{\nu'})\,\langle n|\,\hat{d}_\alpha\,|n'\rangle\,\langle n'|\,\hat{d}^\dagger_\alpha\,|n\rangle\,\times \\ &\times\left\{P\left[\frac{1}{\hbar\,(\omega + \omega_n - \omega_{n'})}\right] - i\pi\delta(\hbar\omega + \hbar\omega_n - \hbar\omega_{n'})\right\}, \end{aligned} \tag{B.27}$$

$A_\alpha(\omega)$ can be read out as:

$$A_\alpha(\omega) = 2\pi\sum_{n,n'}(B_n + B_{n'})\,|\,\langle n|\,\hat{d}_\alpha\,|n'\rangle\,|^2\delta(\hbar\omega + \hbar\omega_n - \hbar\omega_{n'}). \tag{B.28}$$

[1]The Fourier transform of a function f(t) is defined as: $\mathcal{F}\{f(t)\} = \int_{-\infty}^{\infty} f(t)e^{i\omega t}dt$

Since the Green's functions are connected, is it possible to show that $G^{<}_{\mu\nu}(\omega)$ also relates to the spectral function through:

$$-iG^{<}_{\alpha\alpha}(\omega) = A_\alpha(\omega)n_F(\omega), \tag{B.29}$$

where $n_F(\omega) = \frac{1}{e^{\beta(\hbar\omega-\bar{\mu})}+1}$ is the Fermi distribution.

Now, let us recall the expression for the photoemission intensity $I(E_B)$, derived in Section 2.2:

$$I_\alpha\left(E_B\right) \propto \sum_k \left|\langle d^{n-1}_{0k}|\, \hat{d}_\alpha\, |d^n_0\rangle\right|^2 \delta\left(E_{n-1} - E_n - E_B\right), \tag{B.30}$$

The derivation in Section 2.2 assumed $T = 0$, an assumption that leads the initial state $|n\rangle$ to the ground state configuration $|d^n_0\rangle$ with a probability $B_n = 1$, and the final states $|n'\rangle$ can be identified as $|d^{n-1}_0 k\rangle$, and the equation for the Photoemission intensity assumes the form:

$$I_\alpha\left(E_B\right) \propto \sum_k \langle d^{n-1}_{0k}|\, \hat{d}_\alpha\, |d^n_0\rangle \langle d^n_0|\, \hat{d}^\dagger_\alpha\, |d^{n-1}_{0k}\rangle \delta\left(E_{n-1} - E_n - E_B\right). \tag{B.31}$$

Comparing this equation with equation B.25 and using equation B.29, equation $I\left(E_B\right)$ can be written as:

$$I_\alpha(E_B) \propto A_\alpha(E_B)n_F(E_B)\delta\left(E_{n-1} - E_n - E_B\right). \tag{B.32}$$

In other words, **the photoemission spectroscopy measures the occupied portion** (because of the factor $n_F(E_B)$) **of the spectral function $\boldsymbol{A(E_B)}$**.

In a system without interactions, where $\hat{H}_0 = \sum_{\nu\nu'}^{dim\varepsilon_1} \langle\nu|\, h\, |\nu'\rangle\, \hat{d}^\dagger_\nu \hat{d}_{\nu'}$, the retarded Green's function $G^R_{\alpha\beta}(t)$ is given by:

$$G^R_{\alpha\beta}(t) = -\frac{i}{\hbar}\Theta(t)\langle\{\hat{d}_\alpha(t), \hat{d}^\dagger_\beta\}\rangle = -\frac{i}{\hbar}\Theta(t)e^{-i\epsilon_\alpha t/\hbar}\delta_{\alpha\beta} \tag{B.33}$$

where the identities $e^{i\hat{\mathcal{H}}}\, \hat{d}^\dagger_\alpha e^{-i\hat{\mathcal{H}}} = \hat{d}^\dagger_\alpha e^{i\epsilon_\alpha}$ and $e^{i\hat{\mathcal{H}}}\, \hat{d}_\alpha e^{-i\hat{\mathcal{H}}} = \hat{d}^\dagger_\alpha e^{-i\epsilon_\alpha}$ were used. Taking the Fourier transform again and using B.22 yields:

$$G^R_{\alpha\beta}(t) = \frac{1}{\hbar}\frac{\delta_{\alpha\beta}}{(\omega - \omega_\alpha + i\delta)} \tag{B.34}$$

And using equation B.26:

$$A_\alpha(\omega) = -2\Im m\left\{\frac{1}{\hbar}\frac{\delta_{\alpha\beta}}{(\omega - \omega_\alpha + i\delta)}\right\} \tag{B.35}$$

$$A_\alpha(\omega) = 2\pi\delta(\hbar\omega - \hbar\omega_\alpha). \tag{B.36}$$

which is clearly positive definite and normalized to $2\pi/\hbar$. This is actually the density of states of multiplied by 2π, and presents a single peak at $\omega = \omega_\alpha$.

In the interacting case, where $\hat{H} = \hat{H}_0 + \hat{V}$, where $\hat{V}$ has the same form of equation B.13, the frequency ω_α may acquire a shift in its real part and be broadened, which is manifested in an imaginary part such as $\omega_\alpha \to \omega_\alpha^R - i\omega_\alpha^I$, and instead of a Dirac's delta function, $A(\omega)$ assumes the form of a Lorentzian distribution of width $\hbar\omega_\alpha^I$:

$$A_\alpha(\omega) = -2\Im m \left\{ \frac{1}{\hbar} \frac{\delta_{\alpha\beta}}{(\omega - \omega_\alpha^R + i\omega_\alpha^I)} \right\} \tag{B.37}$$

$$A_\alpha(\omega) = \frac{2\omega_\alpha^I}{\hbar[(\omega - \omega_\alpha^R)^2 + (\omega_\alpha^I)^2]}. \tag{B.38}$$

Ultimately, the spectral function can be thought of as an indication of how well the excitation (in the XPS case, the creation of a hole) can be described by a free non-interacting particle.

C Curricular Information

C.1 Conferences

1. **São Paulo School of Advanced Sciences on Recent Developments on Synchrotron Radiation** Campinas, SP - BR (2015).
2. **XXXVIII Encontro Nacional de Física da Matéria Condensada** Foz do Iguaçu, PR - BR (2015).
3. **24^a Reunião Anual de Usuários do LNLS** Campinas, SP - BR (2014).
4. **23^a Reunião Anual de Usuários do LNLS** Campinas, SP - BR (2013).
5. **2nd School on Advanced X-ray Spectroscopic Methods** Campinas, SP - BR (2013).
6. **I Encontro de Físicos do Sul** Curitiba - PR, BR (2013).
7. **XXXVI Encontro Nacional de Física da Matéria Condensada** Águas de Lindóia, SP - BR (2013).
8. **XIII Escola Brasileira de Estrutura Eletrônica** Cuiabá, MT - BR (2012).
9. **XXXV Encontro Nacional de Física da Matéria Condensada** Águas de Lindóia, SP - BR (2012).
10. **16th International Conference on Recent Progress in Many-Body Theories** San Carlos Bariloche - AR (2011).
11. **ANDES/ALPS School on Numerical Methods for Many-Body Theories** San Carlos Bariloche - AR (2011).
12. **São Paulo Advanced School on Anisotropic Conductors and Superconductors** Lorena, SP - BR (2011).

C.2 Publications

1. **Guedes, E. B.**; Abbate, M. ; Abud, F. ; Jardim, R. F. ; Vicentin, F. C. ; Mossanek, R. J. O., Spectroscopy and electronic structure of Sr_2YRuO_6 and $Sr_2YRu_{0.75}Ir_{0.25}O_6$. Physical Review B **94**, p. 045109, 2016.

2. Alves, L. M. S. ; Benaion, S. S. ; Romanelli, C. M. ; dos Santos, C. A. M. ; da Luz, M. S. ; de Lima, B. S. ; Oliveira, F. S. ; Machado, A. J. S. ; **Guedes, E. B.** ; Abbate, M. ; Mossanek, R. J. O., Electrical Resistivity in Non-stoichiometric MoO_2. Brazilian Journal of Physics **45**, p. 234-237, 2015.

3. **Guedes, E. B.**; Abbate, M. ; Ishigami, K. ; Fujimori, A. ; Yoshimatsu, K. ; Kumigashira, H. ; Oshima, M. ; Vicentin, F. ; Fonseca, P. ; Mossanek, R. J. O., Core level and valence band spectroscopy of $SrRuO_3$: Electron correlation and covalence effects. Physical Review. B **86**, p. 235127, 2012.